Passive Coherent Location Radar using Software-Defined Radio techniques.

Francois Sebastiaan Heunis

A dissertation submitted to the Department of Electrical Engineering,
University of Cape Town, in fulfilment of the requirements
for the degree of Master of Science in Engineering.

Durban, May 2010

Declaration

I know the meaning of plagiarism and declare that all the work in this dissertation, save for that which is properly acknowledged, is my own. It is being submitted for the degree of Master of Science in Engineering in the University of Cape Town. It has not been submitted before for any degree or examination in any other university.

Signature of Author .....

Francois Sebastiaan Heunis

Durban

30 May 2010

Abstract

Passive Coherent Location radar is a technology that allows fully functional radar systems to be constructed without the need for a dedicated transmitter. These radar systems operate by utilising existing transmitters already present within the environment. This significantly reduces system costs, as well as complexity. This also means that PCL radar sites are passive and immune to jamming. Furthermore, PCL radar systems are able to operate within portions of the radiofrequency and microwave spectra that have previously been unavailable to radar. The amount of different transmitters and waveforms that are present in the environment is increasing all the time. This, along with the availability of low-cost, high-dynamic range analogue-to-digital converters, as well as desktop computers with powerful processing capabilities, has led to a large amount of published work appearing in the open literature during the last decade.

This dissertation details the design and implementation of a PCL radar system that utilises FM radio transmitters. For this purpose, the Universal Software Radio Peripheral and the opensource GNURadio Software-defined Radio Toolkit is used. It is shown that the PCL radar system has the ability to detect commercial passenger aircraft.

Acknowledgements

I would like to thank the following people, who have all contributed towards this disseration

My supervisor, Prof M.R. Inggs, for providing me with the necessary guidance and supervision.
Dr. Yoann Paichard, for the vast amount of technical advice, knowledge and suggestions that he provided me with.
The members of the GNURadio community, in particular Brian Padalino, for helping me with all my FPGA and HDL related queries.
Dr. Paul Howland and Darek Maksimiuk of the NATO C3 Agency, for answering a lot of my questions regarding PCL radar.
The members of RRSG, in particular Regine Lord, for administrative support, and Marc Brooker, Benson Chan, Gunther Lange, Stephan Sandenbergh, Craig Tong, Jonathan Ward and Lance Williams for assisting me with various things.

The South African National Defence Force, for providing the funding that made this dissertation possible.

Finally, I would like to thank my family and friends for their undying support.

Contents

List of Figures

List of Tables

Nomenclature

A/D	Analogue-to-Digital
AOA	Angle-Of-Arrival
ARD	Amplitude-Range-Doppler
CFAR	Constant False Alarm Rate
CIC	Cascaded Integrator-Comb
CORDIC	COordinate Rotation DIgital Computer
CPU	Central Processing Unit
D/A	Digital-to-Analogue
DAB	Digital Audio Broadcast
DDC	Digital Down-Converter
DFT	Discrete Fourier Transform
DPI	Direct Path Interference
DVB-T	Terrestrial Digital Video Broadcast
ECA	Extensive Cancellation Algorithm
ERP	Effective Radiated Power
ESR	Equivalent Series Resistance
FERS	Flexible, Extensible Radar and Sonar Simulator
FFT	Fast Fourier Transform
FIFO	First In, First Out
FIR	Finite Impulse Response
FPGA	Field-Programmable Gate Array
GMSK	Gaussian Minimum Shift Keying
GPS	Global Positioning System
GSM	Global System for Mobile Communications
HDL	Hardware Description Language
IF	Intermediate Frequency
IIR	Infinite Impulse Response
IP_3	Third-Order Intercept Point
LE	Logic Element
LMS	Least-Mean Square

MSPS Mega-Samples Per Second
NLMS Normalised Least-Mean Square
PC Personal Computer
PCL Passive Coherent Location
PFB Polyphase Filterbank
PFFT Polyphase FFT
RAM Random Access Memory
RCS Radar Cross-Section
RF Radiofrequency
RLS Recursive Least-Squares
SDR Software-Defined Radio
SFDR Spur-Free Dynamic Range
SFN Single Frequency Network
SIR Signal-to-Interference Ratio
SNR Signal-to-Noise Ratio
TDOA Time Difference Of Arrival
TVRX Television Receiver
UCT University of Cape Town
UHF Ultra High Frequency
USB Universal Serial Bus
USRP Universal Software Radio Peripheral
VHF Very High Frequency
WLAN Wireless Local Area Network

Chapter 1

Introduction

The ever-increasing congestion of the radiofrequency (RF) and microwave spectra has led to the development of radar systems that can operate without transmitting any waveforms of their own. These radar systems operate by utilising existing *illuminators of opportunity* to detect reflections from moving airborne or ground-based targets. This technique is know as *passive coherent location* (PCL) radar or *hitchhiking* [3]. An illuminator of opportunity can be any existing transmitter with properties that are favourable for PCL radar. In practice, broadcast transmitters are mostly used due to their high radiated powers and very wide coverage [11]. PCL radar is also a subset of bistatic radar, where the transmitting and receiving antennas are not located at the same site.

This dissertation details the design of such a PCL radar system using the GNURadio[1] software-defined radio (SDR) development toolkit and the Universal Software Radio Peripheral[2] (USRP).

1.1 Passive Coherent Location

The concept of PCL radar is not new. According to Willis [12], most of the ideas concerning bistatic radar are rather old and simply periodically re-invented. In February 1935, Sir Robert Watson-Watt and Arnold Wilkins used a BBC Empire broadcast to detect a Heyford bomber at a range of eigth miles in what became known as the Daventry experiment. Thus, the first British radar experiment was also the first PCL radar experiment [13]. It was, however, soon realised that the detection range was severely limited due to the strong power of the direct signal from the transmitter. It also seemed

[1] Accessed 24 September 2009, <http://gnuradio.org/trac>.
[2] Accessed 24 September 2009, <http://gnuradio.org/trac/wiki/USRP>.

impossible to extract any ranging information and therefore aircraft could only be detected and not located. Apart from some amateur radio interest in the 1960s, PCL radar was mostly forgotten.

In the 1980s, IBM[3] developed a prototype system that could track aircraft in non-realtime by analysing the echoes of the vision carrier of an analogue television signal [13]. Lockheed Martin[4] later acquired this division of IBM and developed a commercial PCL radar system known as Silent Sentry [14]. In 1986, Griffiths and Long [15] published the first open literature work on the utilisation of analogue television signals for radar purposes but, like their predecessors, found that the poor ambiguity function and dynamic range problems prevented them from demonstrating any target detections.

PCL radar received renewed interest in the mid 1990s with the arrival of aircraft with stealth capabilities [16]. This renewed interest was probably due to the potential counterstealth abilities that PCL radar offered because of its bistatic, low-frequency operation. It was, however, not until the 21st century that PCL radar started receiving the attention it deserved. This can be attributed to two major developments. Firstly, analogue-to-digital (A/D) converter technology has evolved to the stage where it is possible to buy an A/D converter capable of digitising the whole FM band, while providing dynamic range sufficient for PCL radar at a reasonable cost. Secondly, as a consequence of Moore's law, the central processing unit (CPU) of a modern personal computer (PC) is able to perform all the processing required by a complete PCL radar system at speeds approaching realtime operation [13]. These advances are enabling university research groups to develop PCL radar prototypes without the need for a large budget. As a result, a lot of published work on PCL radar has appeared in the open literature during recent years.

1.2 Software-defined Radio, GNURadio and the USRP

An SDR is a radio where functions traditionally implemented in hardware are instead implemented in software running on a PC or other embedded computing device. These functions include, among others, mixing, filtering and demodulation. An ideal SDR receiver would have its A/D converter as close to the antenna as possible [17]. In practice, a frontend is used to filter and mix a portion of the RF spectrum down to an intermediate frequency (IF), where it is digitised.

[3]Accessed 24 September 2009, <http://www.ibm.com>.
[4]Accessed 24 September 2009, <http://www.lockheedmartin.com>.

GNURadio is an opensource development toolkit that is widely used to implement SDR systems. It is available as a set of Python[5] packages that can be imported in order to develop an SDR application. A user describes the connections between different signal processing blocks in terms of data rates and types in what is known as a *flowgraph*. A typical flowgraph consists of a signal source, several signal processing blocks and a signal sink. When a flowgraph is started, data flows from the source, gets processed by the signal processing blocks and is delivered to the sink. Users are also able to write their own blocks. For a detailed list of available signal processing blocks and their functions, the reader is referred to Abbas [18].

The USRP hardware, manufactured by Ettus Research LLC[6], is used in conjunction with GNURadio to receive and transmit signals. The USRP consists of an Altera[7] Cyclone field-programmable gate array (FPGA), two Analog Devices[8] AD9862 Mixed-Signal Front-End processors, four slots to connect various USRP daughterboards to and a Cypress[9] FX2 universal serial bus (USB) microcontroller. Each Mixed-Signal Front-End processor contains two 12-bit, 64 Mega-Samples Per Second (MSPS) A/D converters and two 14-bit, 128 MSPS digital-to-analogue (D/A) converters. The FPGA contains logic to mix a signal down from an IF to baseband, lowpass-filter the signal and downsample it to a lower sampling frequency when used as a receiver. When used as a transmitter, the signal is upsampled, lowpass-filtered and mixed up from baseband to an IF. The USB microcontroller handles communication with the host PC over a USB 2 interface. For a more detailed overview of the USRP and the different daughterboards, refer to Abbas [19].

1.3 Research Motivation

PCL radar is still in its infancy and offers a lot of scope for future research. Potential new applications include, but are not limited to, the monitoring of people in buildings, the monitoring of vehicles on roads and the deployment of low-cost air traffic management systems in countries where none currently exist. The ability to develop a cost-effective PCL radar system would enable small research groups and amateur radio enthusiasts to contribute to this topic. The number of different transmitters and waveforms that could be utilised are also increasing. A PCL radar system should therefore be flexible to enable it to simultaneously utilise a multitude of different waveforms

[5]Accessed 24 September 2009, <http://www.python.org>.
[6]Accessed 24 September 2009, <http://www.ettus.com>.
[7]Accessed 24 September 2009, <http://www.altera.com>.
[8]Accessed 24 September 2009, <http://www.analog.com>.
[9]Accessed 24 September 2009, <http://www.cypress.com>.

for target detection. The USRP, along with the GNURadio SDR toolkit, offers this flexibility and affordability and therefore shows the potential to be an ideal platform for an experimental PCL radar system.

1.4 Objectives

The objectives of this dissertation are as follows.

- Perform basic experiments with the USRP television receiver (TVRX) daughterboard to characterise its performance when used as a receiver for a PCL radar system that utilises FM radio transmissions.
- Analyse the signal processing blocks used in the digital down-converter (DDC) of the FPGA. Modify the filtering stages to transfer as much signal bandwidth over the USB connection as possible, while providing the necessary suppression of unwanted out-of-band signals.
- Perform a study on the signal processing required to detect targets in a PCL radar system. Implement the signal processing in software. Use the Flexible, Extensible Radar and Sonar Simulator (FERS) [20] to simulate a PCL radar system and test the signal processing software.
- Perform a study on target location in a PCL radar system using time difference of arrival (TDOA) measurements and multilateration. Simulate a multistatic PCL radar system and show that the coordinates of a target can be calculated when TDOA measurements from multiple transmitters are available.
- Perform a study on channelisation, with the aim of channelising a portion of the FM band into separate channels. Determine whether a channeliser can be implemented on the FPGA, and if possible, implement one.
- Integrate all the above tasks into a complete PCL radar system. Demonstrate that targets can be detected with the system.
- Comment on the performance of the PCL radar system. Identify problems and make suggestions regarding future improvements.

1.5 Dissertation Outline

Chapter 1 introduces the concept of PCL radar and SDR. A brief overview of the GNU-Radio SDR toolkit and the USRP is given. The motivation and research objectives of this dissertation are stated.

Chapter 2 expands on the topic of PCL radar and provides a comprehensive literature review. The important properties of PCL radar are discussed. The anatomy of a PCL radar system is presented. The advantages and disadvantages of PCL radar are discussed. Different illuminators of opportunity are analysed, along with the properties of their waveforms and the tradeoffs that need to be considered with each of them.

Chapter 3 presents a brief performance analysis of the TVRX daughterboard. Measurements are made to determine the 1-dB compression point of the receiver for different amplifier gain settings. The third-order intercept point (IP_3) of the receiver is determined from measurements. The total response of the filters in the receiver is measured to determine the receiver bandwidth and the attenuation of out-of-band signals. A bandpass filter is designed and constructed to suppress a strong FM radio station transmitted from the University of Cape Town (UCT) campus, and to provide additional attenuation of out-of-band signals prior to the receiver.

Chapter 4 looks at the signal processing stages on the FPGA. The oscillator and mixer are evaluated to determine the dynamic range and the frequency accuracy with which a signal can be mixed down from an IF to baseband. The different filtering and decimation stages are looked at. Each stage is evaluated in terms of its out-of-band attenuation and passband response. Improvements are made where necessary to utilise the logic resources of the FPGA as efficiently as possible.

Chapter 5 presents a study on the signal processing stages required to detect targets in a PCL radar system. The matched filter processing is implemented and tested through simulations. A possible method to accelerate the matched filter processing is identified, implemented and tested. Suitable direct path interference (DPI) and clutter suppression algorithms are identified and implemented. The performance of the suppression algorithms are evaluated. A suitable DPI suppression algorithm to be used in the experimental PCL radar system is chosen.

Chapter 6 investigates the channelisation of a portion of the FM band using a polyphase filterbank (PFB). The filterbank is analysed and implemented in Matlab to gain a better understanding of how it functions. A PFB is implemented using GNURadio signal processing blocks. The Matlab and GNURadio PFBs are used to channelise a portion

of the FM band into separate channels. The method of locating a target in a multistatic PCL radar system using TDOA measurements and multilateration is studied. Software is written to calculate the coordinates of a target when TDOA measurements from more than one transmitter are used. A multistatic PCL radar system with a single target is simulated. The software is used to calculate the coordinates of the simulated target.

Chapter 7 describes the experiments that were performed using the experimental PCL radar system. The results obtained after each processing stage are presented and discussed.

Chapter 8 draws all the completed work together. The results of the various experiments are discussed and conclusions are made. The problems that were encountered are presented, as well as proposed solutions. Recommendations regarding future work are made.

Chapter 2

Passive Coherent Location Radar

Bistatic radar systems have been around since the earliest days of radar. The advent of the duplexer, which made it possible to transmit and receive through the same antenna, meant that monostatic systems have since dominated radar design [3]. Bistatic radar systems do however have a number of advantages, and now practical and cost-effective systems are beginning to emerge. The receiver site of a bistatic radar system is passive and hence, undetectable. Receiver sites are also potentially simple and cheap. Bistatic radar systems also have counter-stealth capabilities since target shaping to reduce the monostatic radar cross-section (RCS) will in general not reduce the bistatic RCS. A further advantage is that multiple receivers can be deployed, each forming a bistatic radar with a single transmitter. This would allow better coverage and more accurate target location [21].

PCL radar systems operate by utilising transmitters that are already present in the environment. As a consequence, the location and power of the transmitter and the nature of the transmitted waveform are not under the control of the radar designer. A big part of the challenge in designing a PCL radar system lies in utilising a waveform for a purpose other than what it was originally designed for. A typical PCL radar system is shown in Figure 2.1.

An illuminator of opportunity can be any existing transmitter with properties that are favourable for PCL radar. Systems that utilise FM radio [11], analogue TV broadcasts [22], Global System for Mobile communications (GSM) signals [23], terrestrial digital video broadcasts (DVB-T) and digital audio broadcasts (DAB) [24] have been demonstrated. Other proposed methods include Global Positioning System (GPS) signals from satellites [25] and wireless local area network (WLAN) signals [26].

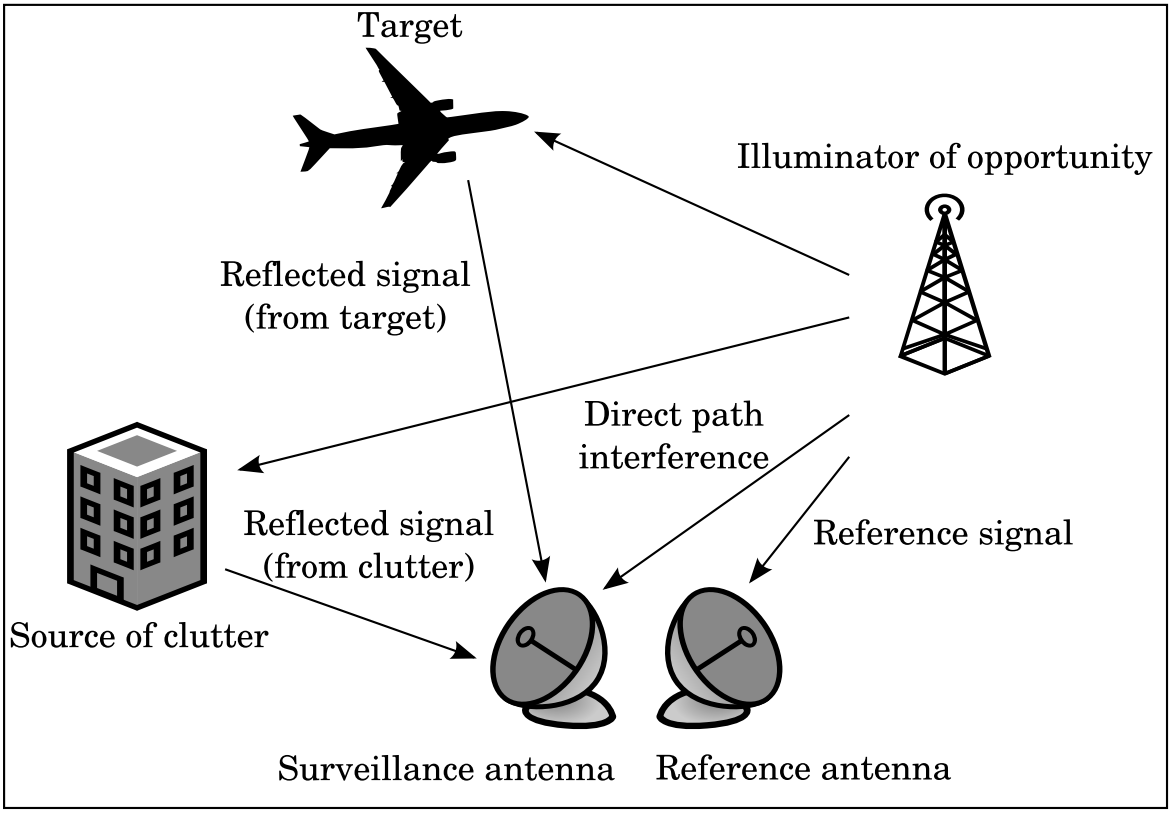

Figure 2.1: The geometry of a typical PCL radar system.

A basic PCL radar system requires two antennas. The first antenna, often called the *reference* antenna, is used to capture a direct version of the signal being utilised and should point in the direction of the transmitter. This captured direct signal serves two purposes. Firstly, it provides a reference signal against which the signal from the *surveillance* channel is correlated in the matched filter processing stage. Secondly, a direct version of the signal is required in the DPI suppression stage to cancel adaptively the direct signal component in the surveillance channel. The second antenna, usually called the surveillance antenna, is used to capture signals containing time-delayed and Doppler-shifted versions (i.e. reflections from moving targets) of the signal being utilised. In practice, the surveillance antenna also receives a strong direct signal component from the transmitter, as well as strong returns from stationary clutter. Including a second surveillance antenna in a PCL radar system enables the angle-of-arrival (AOA) of target reflections to be measured using phase interferometry [11]. The AOA, Φ, can be calculated as follows

$$\Phi = \frac{2\pi d}{\lambda} \sin\theta \tag{2.1}$$

where d is the distance between the two antennas, λ is the wavelength and θ is the phase difference between the signal reflections received at the two antennas. To min-

imise angular ambiguities, the two surveillance antennas should be mounted half a wavelength apart.

2.1 Anatomy of a PCL Radar System

2.1.1 Data Collection

The first section of a PCL radar system contains all the analogue components required to filter, amplify and downconvert the signals received by the reference and surveillance antennas. As shown in Figure 2.2, this is also the stage where the analogue signals are digitised for processing. The main requirements are high dynamic range and highly linear receiving equipment with a low noise figure [1]. One of the factors severely influencing the performance of a PCL radar system is the DPI component received by the surveillance antenna. This DPI correlates perfectly with the reference signal and produces range and Doppler sidelobes that are several orders of magnitude larger than the reflected signals from targets [11]. A number of different techniques can be employed to reduce the DPI component received by the surveillance antenna. Terrain shielding is a technique whereby the surveillance antenna is shielded from the transmitter by placing it behind a building or other physical structure. The Manastash Ridge radar is a good example, where the surveillance antenna is shielded from the transmitter by a mountain range [27]. Spatial suppression may also be achieved by steering the surveillance antenna so that the transmitter falls inside a null or a low sidelobe. Another approach is to use an analogue canceller before digitisation of the surveillance signal. An example of this is the Howells-Applebaum analogue cancellation loop [28]. In practice, a combination of different techniques should be used to relax the dynamic range requirements on the A/D converters.

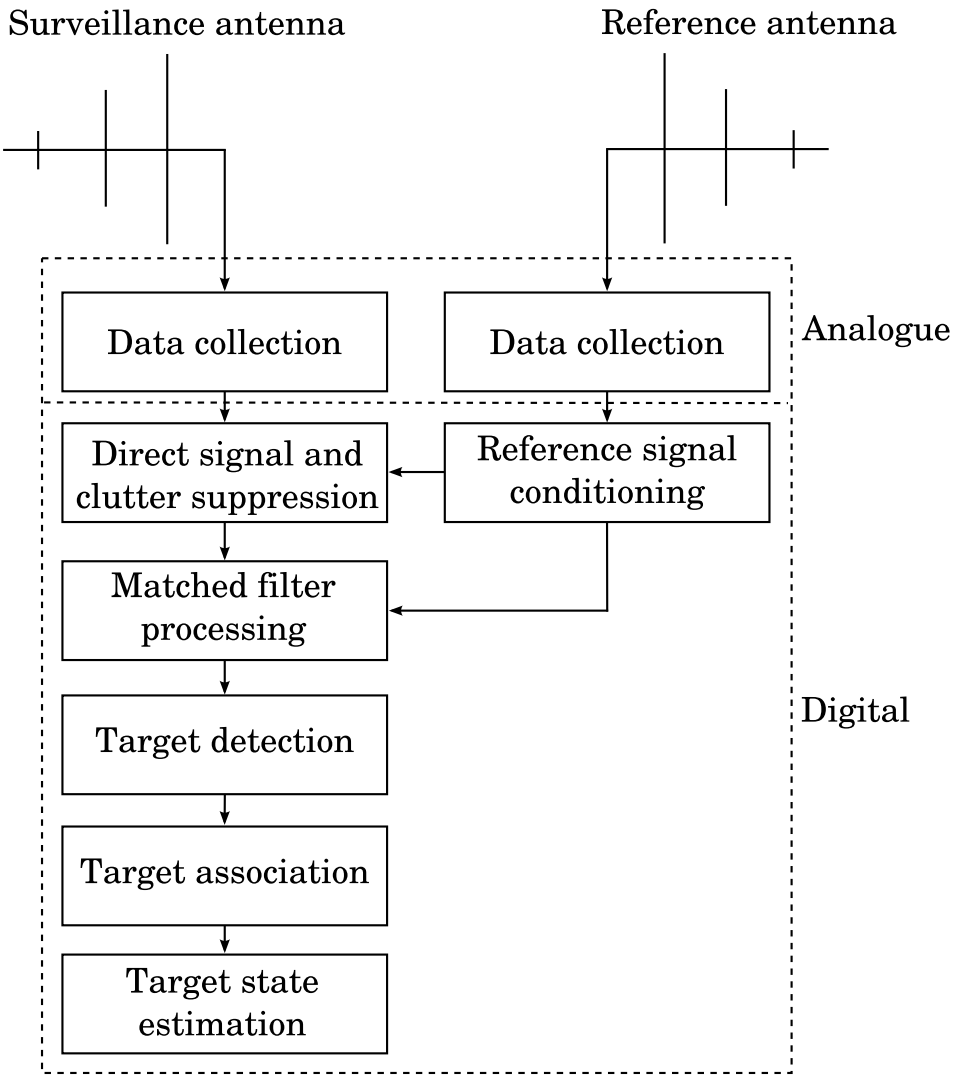

Figure 2.2: The anatomy of a PCL radar system [1].

2.1.2 Reference Signal Conditioning

When utilising certain transmissions in a PCL radar system, the reference signal first needs to be preprocessed in order to improve its quality. For systems utilising FM radio transmissions, this stage is not necessary. An example occurs when utilising DAB signals in a single frequency network (SFN). In this case, the raw reference signal would consist of several identical, time-shifted copies of the reference signal from each transmitter within line-of-sight of the receiver. If the matched filter processing is performed on the surveillance signal and the raw reference signal, a single target would show up as multiple time-shifted targets on the amplitude-range-Doppler (ARD) surface. To avoid this, the multipath-resistant features of the DAB waveform need to be utilised in order to construct a pure reference signal [1].

2.1.3 Direct Signal and Clutter Suppression

As mentioned earlier, the surveillance channel of a PCL radar system contains a strong DPI component, as well as time-delayed reflections from clutter sources. These unwanted signals correlate highly with the reference signal, causing the weak reflections from moving targets to be masked by the resulting sidelobes.

In addition to analogue, physical and spatial techniques, an adaptive filtering algorithm should also be used for DPI suppression. This involves using a noise canceller structure to estimate the direct signal and clutter components in the surveillance channel. This estimate is then subtracted from the surveillance signal. Ideally, the surveillance signal should now contain only target reflections. In practice, the amount of suppression that can be achieved is limited due to estimation errors in the noise canceller. Howland [11] details the development of an adaptive M-stage lattice predictor, followed by an adaptive tapped delay line. This approach ensures rapid convergence of the suppression algorithm.

2.1.4 Matched Filter Processing

At the core of a PCL radar system lies the matched filter processing stage. After suppression of the DPI and clutter components in the surveillance channel, it is necessary to search for time-delayed and Doppler-shifted versions of the reference signal. This is achieved by correlating the surveillance signal with Doppler-shifted versions of the reference signal to form a bank of filters matched to every possible Doppler frequency of interest. This is equivalent to calculating the ambiguity function and can be written as follows

$$\left|\Psi(R_R, f_d)^2\right| = \left|\int_{-\infty}^{\infty} s(t)d^*(t + R_R)\text{exp}(j2\pi f_d t)dt\right|^2 \tag{2.2}$$

where $|\Psi(R_R, f_d)^2|$ denotes the ARD surface being calculated, $s(t)$ represents the surveillance signal, $d(t)$ represents the reference signal, R_R represents the range of interest and f_d represents the Doppler shift of interest [11].

2.1.5 Target Detection

Having calculated an ARD surface, the next step involves identifying the range and Doppler cells that exceed a detection threshold. To maintain a constant probability of false alarm, the detection threshold is constantly changed according to an estimate of

the noise variance. A conventional constant false alarm rate (CFAR) algorithm can be used for this task [29].

2.1.6 Target Association

The output of the CFAR algorithm produces all the cells on the ARD surface that contain target detections. It is now necessary to associate this range and Doppler data with individual targets. A standard Kalman filter, provided with measurements of range, Doppler and AOA, and estimates of range, Doppler, Doppler rate, bearing and bearing rate can be used to effectively track targets in the range-Doppler space [1].

2.1.7 Target State Estimation

The final stage of a PCL system aims at estimating each target's track parameters, such as location, heading and speed, from the measurements of range, Doppler and AOA. An extended Kalman filter can be used for this purpose. Track initialisation in wideband PCL systems is a simple process as opposed to narrowband systems where range measurement data is not available. Elaborate initialisation schemes are required in the latter case [22].

2.2 Properties of PCL Radar Systems

2.2.1 The Geometry of a PCL Radar System

The geometry of a PCL radar system is identical to that of a bistatic radar system. Jackson [2] analysed the geometry of bistatic radar systems and his notation and North-referenced coordinate system has been widely adopted. The North-referenced system and its parameters are shown in Figure 2.3.

The coordinate sets (x_T, y_T, z_T), (x_R, y_R, z_R) and (x, y, z) represent the coordinates of the transmitter, receiver and target respectively, while V represents the velocity of the target. The triangle formed by the transmitter, receiver and target is known as the *bistatic triangle*. The transmitter and receiver are connected by the bistatic baseline with length L. The transmitter and receiver look angles are given by θ_T and θ_R respectively and are measured clockwise from the north of the coordinate system. The bistatic angle, β, is given by $\beta = \theta_T - \theta_R$. The bistatic bisector bisects the bistatic angle. δ is the target angle relative to the bistatic bisector. R_T represents the range from the transmitter to the target and R_R the range from the target to the receiver.

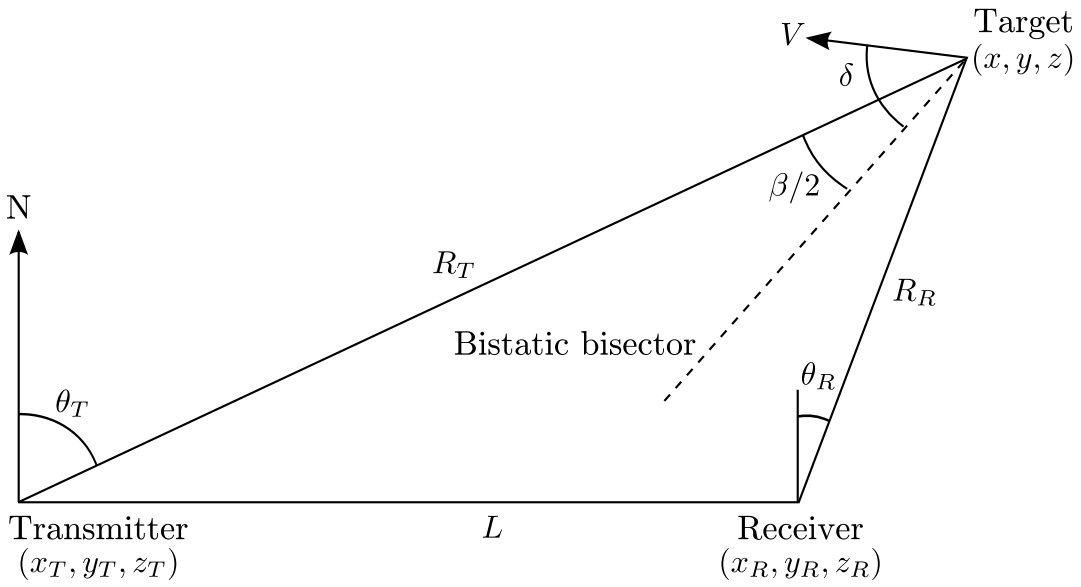

Figure 2.3: The North-referenced coordinate system [2].

2.2.2 The Bistatic Radar Equation

With reference to Figure 2.3, the bistatic radar equation for a PCL radar system is given by

$$\frac{P_r}{P_n} = \frac{P_t G_t G_r \lambda^2 \sigma_b L}{(4\pi)^3 R_T^2 R_R^2 k T_0 B F} \tag{2.3}$$

where

P_r	is the received signal power
P_n	is the receiver noise power
P_t	is the transmit power
G_t	is the transmit antenna gain
G_r	is the receive antenna gain
λ	is the wavelength
σ_b	is the target bistatic RCS
$L\ (\leq 1)$	are system losses
k	is Boltzmann's constant
T_o	is the noise reference temperature (290 K)
B	is the receiver bandwidth
F	is the receiver noise figure

2.2.3 Bistatic Range

The bistatic range of a target is given by the equation of an ellipsoid with the transmitter and receiver as the two foci [21]. With reference to Figure 2.3, the equation of such an ellipsoid is

$$\sqrt{(x_R - x)^2 + (y_R - y)^2 + (z_R - z)^2} + \sqrt{(x_T - x)^2 + (y_T - y)^2 + (z_T - z)^2} = \ldots \\ \ldots R_T + R_R \tag{2.4}$$

By projecting the ellipsoid onto the $z = 0$ plane, an ellipse is found, also known as a *contour of constant bistatic range*. An example of such a contour is shown in Figure 2.4. In this case the receiver is located at UCT and the transmitter at Constantiaberg.

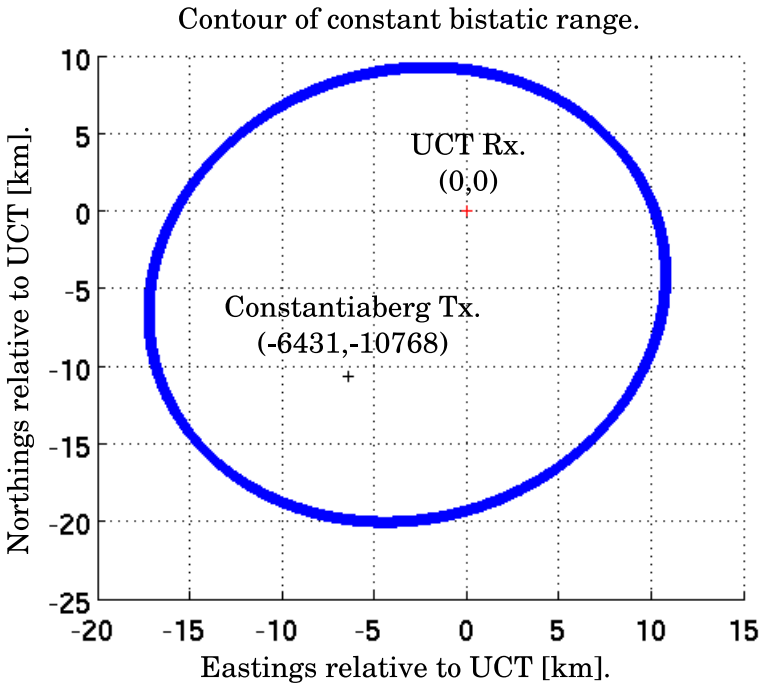

Figure 2.4: Contour of constant bistatic range for a target with a bistatic range of 30 km.

2.2.4 Bistatic Doppler

The Doppler shift of a target in a PCL radar system is a function of the velocities of the target, transmitter and receiver and their positions relative to each other [3]. With reference to Figure 2.3, and assuming that the transmitter and receiver are both

stationary, the Doppler shift of a reflected target signal is given by

$$f_D = (\frac{2V}{\lambda}) \cos\delta \cos(\beta/2) \tag{2.5}$$

2.2.5 Bistatic Radar Cross-Section

In PCL radar systems, target detection and location are a function of the spatially dependent bistatic RCS, target dynamics and radar design parameters. Rather little work has appeared in the open literature regarding the bistatic RCS of targets [21]. Kell [30] found that the bistatic RCS is comparable to the monostatic RCS measured at the bisector of the bistatic angle at a frequency lower than the true frequency by a factor of $\cos(\beta/2)$. This approximation only holds for small bistatic angles.

As the bistatic angle approaches 180° (i.e. the target lies on the bistatic baseline), the forward scatter zone is encountered. Targets located in the forward scatter zone have a substantially increased RCS. This is explained by Babinet's principle, which states that the forward scatter from a perfectly-absorbing target is equivalent to that of a target-shaped aperture in a perfectly-conducting sheet, apart from a 180° phase shift [21]. A target of physical area, A, will have an RCS of

$$\sigma_b = \frac{4\pi A^2}{\lambda^2} \tag{2.6}$$

while the angular width of the scattered signal is given by

$$\theta_b = \frac{\lambda}{d} \tag{2.7}$$

where d is the target linear dimension. Figure 2.5 shows how θ_b and σ_b vary with frequency for a target with $A = 10$ m^2 and $d = 20$ m.

It can be seen that θ_b increases as the frequency decreases, making the target detectable over a wider angular range. The ability of a PCL radar system to operate in the very high frequency (VHF) and ultra high frequency (UHF) bands makes it an ideal candidate for a forward scatter radar. The tradeoff with a forward scatter radar system is that the target's bistatic range cannot be measured. Target tracking can however still be performed using Doppler and AOA measurements [22].

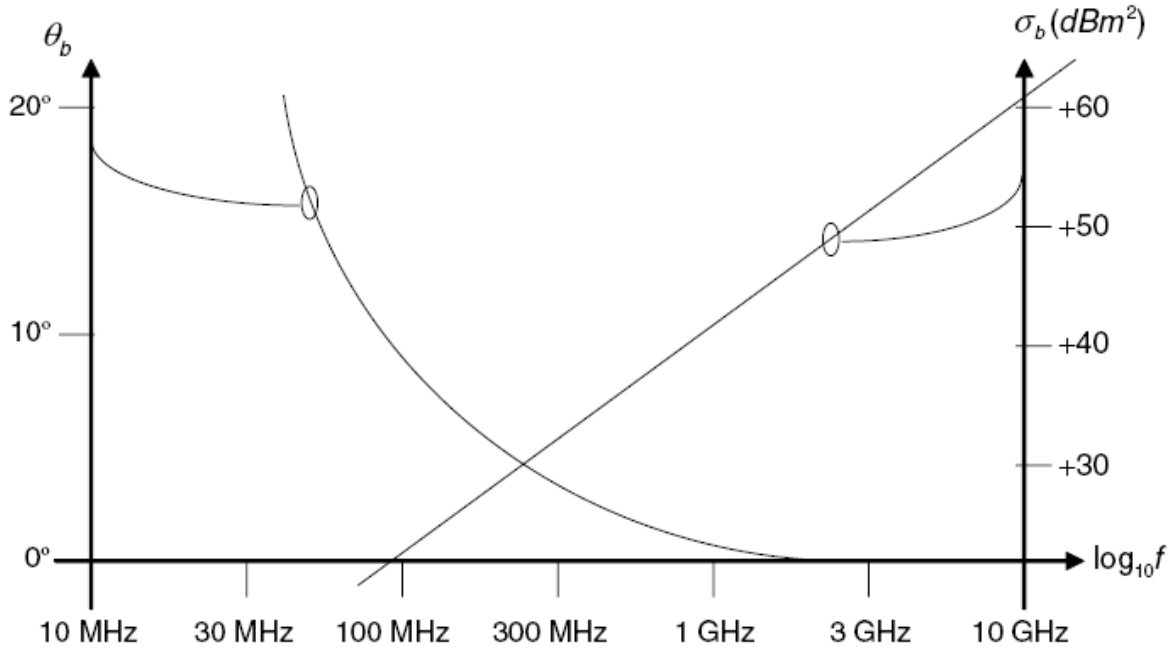

Figure 2.5: Variation of θ_b and σ_b with frequency [3].

2.2.6 The Self-Ambiguity Function

The ambiguity function was defined in Equation 2.2. When a signal is matched-filtered with itself, it is equivalent to calculating the self-ambiguity function of the signal [5]. The self-ambiguity function provides a useful visual tool to determine the range and Doppler resolutions of a waveform, as well as locate any ambiguities in range and Doppler. Examples of the self-ambiguity function will be presented later in this chapter, when the suitability of different transmitters of opportunity for PCL radar are evaluated.

2.2.7 The Bistatic Ambiguity Function

The self-ambiguity function does not take the relative positions of the receiver, transmitter and target into account and therefore mimics a monostatic geometry. The self-ambiguity function provides an indication of the best achievable range and Doppler resolutions [5]. Tsao [4] analysed the ambiguity function for bistatic radar and found that in practice, the range and Doppler resolutions in a bistatic radar are highly dependent on the relative positions of the receiver, transmitter and target. This is also true for a PCL radar system. A more appropriate formulation of the ambiguity function for bistatic radar is given by

$$|\psi(R_{RH}, R_{Ra}, V_H, V_a, \theta_R, L)| = \ldots$$
$$\ldots \left| \begin{array}{c} \int_{-\infty}^{\infty} s_t(t - \tau_a(R_{Ra}, \theta_R, L)) s_t^*(t - \tau_H(R_{RH}, \theta_R, L)) \times \ldots \\ \ldots \exp\left[j(2\pi f_{DH}(R_{RH}, V_H, \theta_R, L) - 2\pi f_{Da}(R_{Ra}, V_a, \theta_R, L))t\right] dt \end{array} \right|^2 \tag{2.8}$$

where R_{RH} and R_{Ra} are the hypotesised and actual ranges from the target to the receiver, V_H and V_a are the hypothesised and actual radial velocities of the target relative to the receiver, θ_R is the angle of the target relative to the receiver in the North-referenced coordinate system and L is the length of the bistatic baseline [5]. The above formula assumes that the receiver is the reference point in the bistatic radar system. Figures 2.6 and 2.7 illustrate the influence of the bistatic geometry on the achievable range and Doppler resolutions.

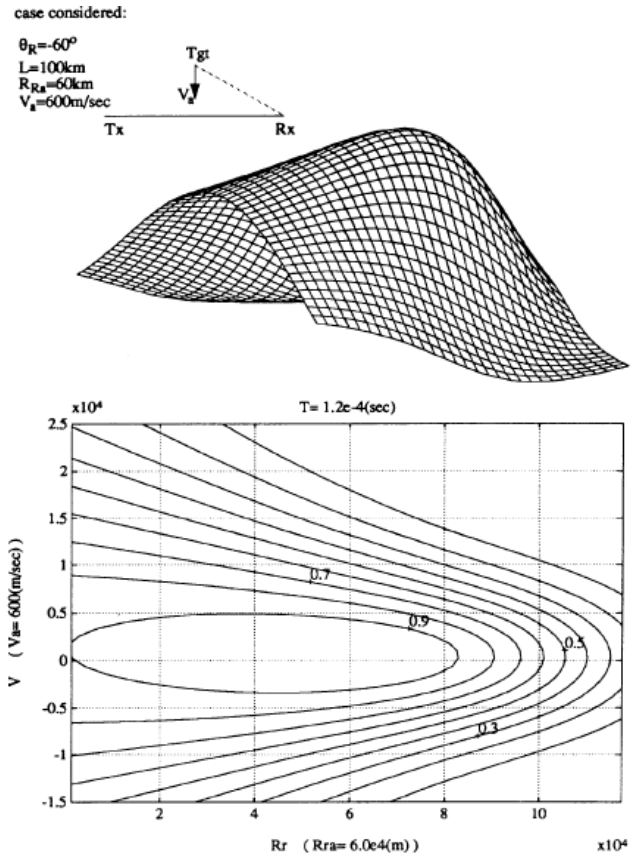

Figure 2.6: Matched filter output for a target approaching the bistatic baseline [4].

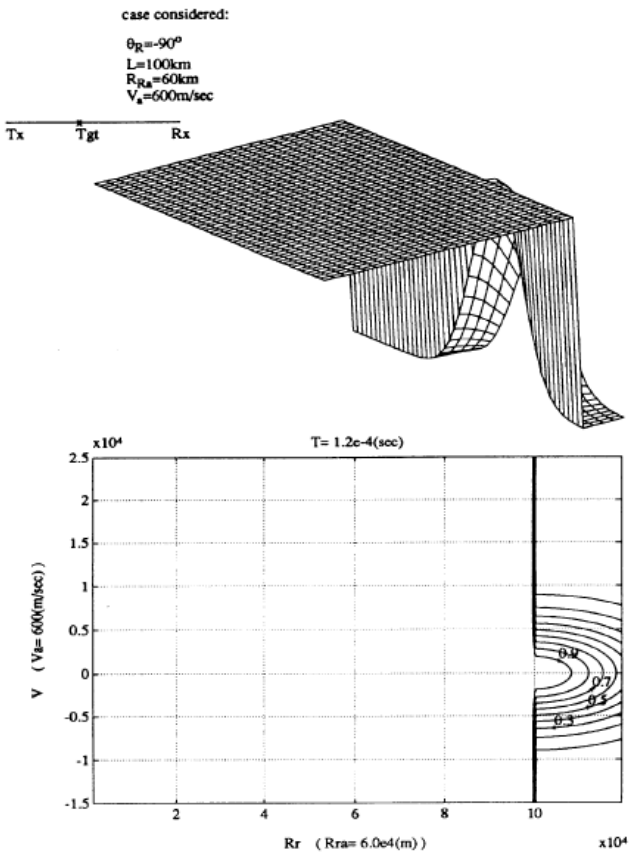

Figure 2.7: Matched filter output for a target on the bistatic baseline [4].

Figure 2.6 shows that as the target approaches the bistatic baseline, the range resolution starts to deteriorate. From Figure 2.7 it can be seen that the range of a target that is on the bistatic baseline cannot be determined.

2.2.8 Range and Doppler Resolution

In any radar system, range resolution determines the minimum range between targets for correct target separation [23]. The range resolution of a PCL radar system, ΔR, is given by

$$\Delta R = \frac{c}{2B\cos(\beta/2)} \tag{2.9}$$

where c is the speed of light and B is the signal bandwidth.

The Doppler resolution of a PCL radar system, Δf_d, is determined by the total coherent integration time and can be calculated using

$$\Delta f_d = \frac{1}{T} \tag{2.10}$$

where T is the coherent integration time [23].

2.3 Illuminators of Opportunity

Utilising existing transmitters to provide a waveform for target detection is what distinguishes a PCL radar system from a conventional radar system. Unfortunately, this means that a radar designer has no control over the form, nature and origin of the transmitted waveform [5]. Lately, however, there has been a dramatic increase in the number and variety of transmitters that could be utilised in a PCL radar system. Spectral congestion is usually a problem for radar designers, but for PCL radar it presents a significant advantage [3]. Radar designers are now able to select the most appropriate transmitters for a given application when designing a PCL radar system. The most important properties of an illuminator of opportunity are (i) power density at the target, (ii) spatial and temporal coverage, and (iii) waveform properties [3]. The power density at the target, Φ, is given by

$$\Phi = \frac{P_t G_t}{4\pi R_T^2} \tag{2.11}$$

and is measured in W/m^2.

2.3.1 FM Radio

In most parts of the world, the FM radio band ranges from 87.5 MHz to 108 MHz and forms part of the larger VHF band. FM radio transmissions have the desirable properties of very broad coverage and high transmitted powers [21]. This is because FM radio transmitters have to cope with non line-of-sight propagation and innefficient antenna and receiver systems at the user end [3]. These properties make FM radio an ideal candidate for a PCL radar system. Figures 2.8 and 2.9 compare the range and Doppler resolutions of two captured FM radio signals, modulated by speech and music respectively.

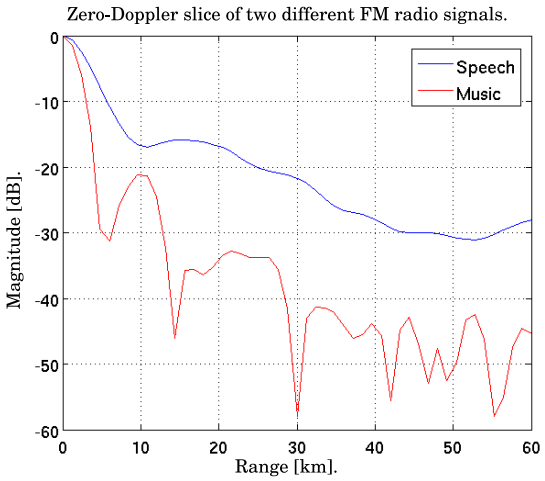

Figure 2.8: Zero-Doppler slice of two FM radio transmissions, modulated by speech and music respectively.

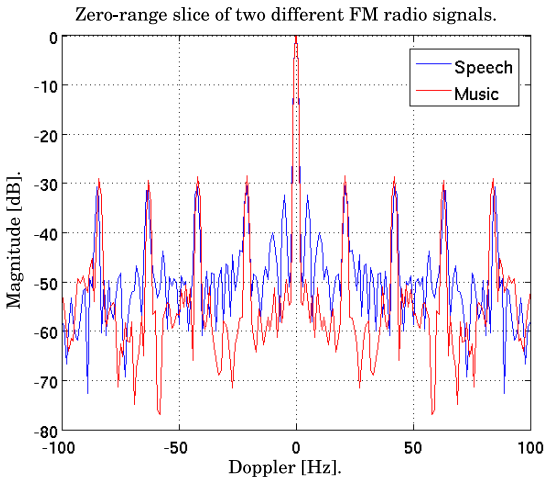

Figure 2.9: Zero-range slice of two FM radio transmissions, modulated by speech and music respectively.

The superior range resolution and lower range sidelobes of the signal modulated by music can clearly be seen. Music has more spectral content than speech, resulting in a modulated signal with a higher bandwidth. By referring to Equation 2.9, it can be concluded that a higher bandwidth results in better range resolution. Baker [5] found that the range resolution of FM radio varies between 19 km (for speech) and 6 km (for fast tempo jazz). The Doppler sidelobes of the two FM signals show similar structure, with a slight improvement for the signal modulated by music.

2.3.2 Analogue TV

Analogue TV broadcasts are usually located in the UHF band. As with FM radio, analogue TV broadcasts have broad coverage and high transmitted powers. Analogue TV broadcasts also have a high bandwidth, making them a potential candidate for a

PCL radar system. Figures 2.10 and 2.11 show the zero-Doppler and zero-range slices of the self-ambiguity function of an analogue TV transmission.

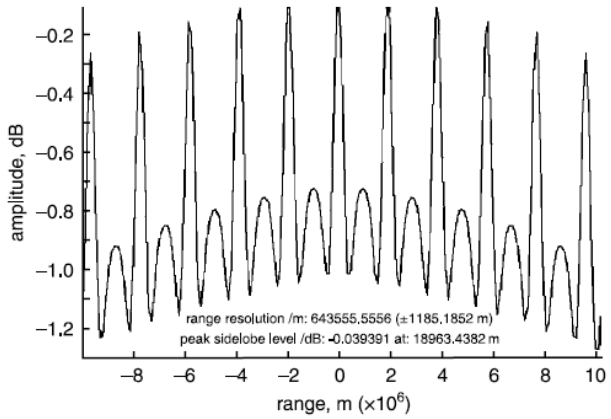

Figure 2.10: Zero-Doppler slice for an analogue TV transmission [5].

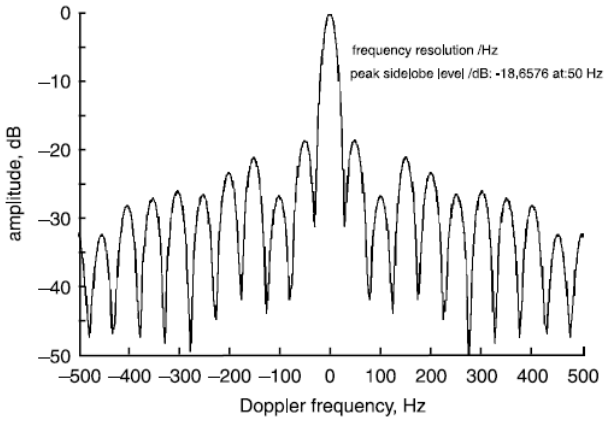

Figure 2.11: Zero-range slice for an analogue TV transmission [5].

The zero-Doppler slice reveals range ambiguities every 19.2 km. These ambiguities are a result of the 64 μs line fly back time of the vision carrier of the analogue TV signal. Because of these range ambiguities, the utilisation of analogue TV signals for PCL radar is quite complicated and its application is likely to be limited [5]. Howland [22] detected and tracked aircraft by monitoring the Doppler history of analogue TV broadcasts.

2.3.3 GSM

Another potential family of illuminators of opportunity that can be utilised in a PCL radar system are GSM transmitters used for digital cellular communication. GSM uses Gaussian minimum shift keying (GMSK) and occupies the 900 MHz and 1800 MHz bands in most countries. Two 25 MHz-wide bands have been allocated around each of the GSM bands, one for the uplink and one for the downlink. Each of the 25 MHz bands are divided into 124 carriers, each spaced 200 kHz apart. The radiated power of GSM basestations is usually very low, with a single basestation covering a radius of approximately 2 km [23]. One advantage of GSM signals is that the bandwidth is relatively constant over time, resulting in little variation of the achievable range resolution. Figures 2.12 and 2.13 show the zero-Doppler and zero-range slices of the self-ambiguity function of a GSM 1800 signal.

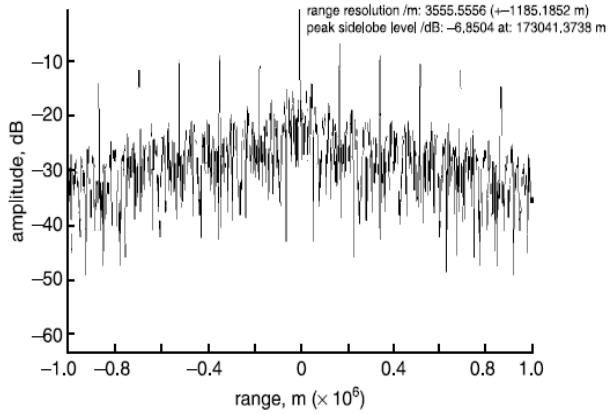

Figure 2.12: Zero-Doppler slice for a GSM 1800 signal [5].

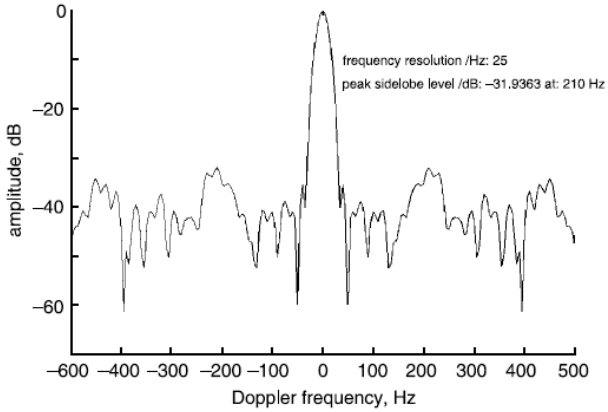

Figure 2.13: Zero-range slice for a GSM 1800 signal [5].

The zero-Doppler slice reveals the presence of equally-spaced range ambiguities. These ambiguities are a result of the bitrate modulation used by GSM [5]. The ambiguities are not a major concern, since the coverage of a single GSM basestation is relatively small. A potential PCL radar application would be to track targets moving through a whole network of GSM basestations.

2.4 Advantages and Disadvantages of PCL Radar

PCL radar has a number of advantages when compared to conventional radar. This, along with the advancements in A/D converter and processor technology, are the primary reasons for the recent upsurge in PCL radar research. Some of the advantages of PCL radar are

- The receiver is entirely passive and hence, undetectable by surveillance receivers.
- PCL radar requires no spectrum allocation and has a minimal impact on the environment [31].
- Stealth technology is less effective against PCL radar. Stealth aircraft are designed with a very low monostatic RCS. Because PCL radar is bistatic in nature, stealth aircraft will still reflect electromagnetic energy towards the receiver. Multiple receivers can also be deployed, forming a multistatic radar system, to further enhance the detection of stealth aircraft [21]. PCL radar systems have the further advantage of being able to operate in the VHF and UHF bands. The absorbing layers on stealth aircraft are not designed for these low frequencies, making them less effective against a PCL radar system [24].

- PCL radar systems do not require dedicated transmitters, reducing system costs.
- A wide variety of both terrestrial and space-based broadcasts exist, providing frequency and spatial diversity. Different transmitters and various different waveforms can be simultaneously utilised to improve detection performance [21].

PCL radar unfortunately has disadvantages, the most important ones being

- The geometry and associated signal processing is more complicated than that of a monostatic system [3].
- Using adaptive antennas for DPI suppression reduces the cost-effectiveness and simplicity of a PCL receiver [28].
- Not all waveforms are suitable for PCL radar purposes. Some, such as DVB-T signals, need appropriate reference signal conditioning before being suitable for PCL radar [32].

2.5 Chapter Summary

This chapter presented an overview of PCL radar, including the most important properties. It was found that the geometry and many other characteristics of a PCL radar system are identical to that of a bistatic radar system. The presence of various different transmitters and waveforms in the environment presents unique challenges and opportunities to the designer of a PCL radar system. Of all the potential transmitters, FM radio transmitters have the most attractive properties for a PCL radar system. The high radiated powers, very broad coverage and the absence of range and Doppler ambiguities in the transmitted waveform are ideal. The downside to utilising FM radio transmitters is the relatively low range resolution of the transmitted waveforms. Chapter 6 will investigate more accurate target location by utilising transmissions from multiple FM radio transmitters.

Chapter 3

The PCL Radar Receiver

In a PCL radar system, the task of the reference and surveillance channel receivers are to amplify, filter and mix a portion of the RF or microwave spectrum down to an IF before digitisation. As mentioned in Chapter 2, the main requirements of a PCL receiver are 1) high dynamic range; 2) high linearity; 3) low noise.

For the experimental PCL radar system, the TVRX daughterboard was considered. The daughterboard is based on the Microtune[1] 4937 DI5 3X7901 tuner module. This chapter presents an analysis of the TVRX daughterboard and discusses basic experiments that were performed to characterise the performance of this module. For a more complete performance characterisation, the reader is referred to Volkwin [33]. This chapter also presents the design, construction and performance evaluation of a bandpass filter to provide additional attenuation before the receiver and to attenuate a strong FM radio station transmitted from the UCT campus. This chapter concludes with a discussion of the results.

3.1 The TVRX Daughterboard

The TVRX daughterboard is a complete receiver, covering the frequency range between 50 and 860 MHz. The daughterboard therefore covers the VHF low, VHF high and UHF bands of the electromagnetic spectrum. The daughterboard allows the user to select a frequency of interest, which is then bandpass-filtered and mixed down to an IF of 44 MHz, before being digitised by an A/D converter on the AD9862 Mixed-Signal Front-End processor. The daughterboard also contains an RF and an IF amplifier. The RF amplifier has a gain range of 0 to 60 dB, while the IF amplifier has a gain range of 0 to 35 dB. Figure 3.1 shows a picture of the daughterboard.

[1] Accessed 20 February 2010, <http://www.microtune.com>.

Figure 3.1: The TVRX daughterboard.

3.1.1 Performance Characterisation

The purpose of the measurements that were performed to characterise the performance of the receiver were as follows: 1) to determine how the gains of the RF and IF amplifiers should be set to utilise the dynamic range of the receiver as efficiently as possible, while avoiding saturation; 2) to determine how well the receiver is able to suppress third-order distortion products; 3) to determine the bandwidth of the receiver and how well out-of-band frequencies are attenuated.

1-dB Compression Point

The 1-dB compression point is a measure of the input signal level at which the receiver begins to deviate from a linear amplitude response. For a linear receiver, each 1 dB increase in input signal power should result in a 1 dB increase in output signal power [6]. Figure 3.2 shows an illustration of the 1-dB compression point.

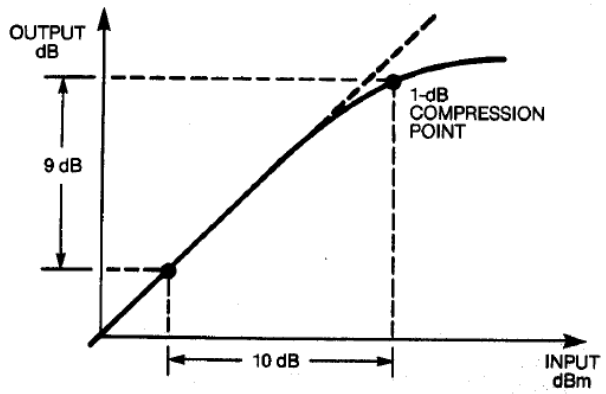

Figure 3.2: An illustration of the 1-dB compression point [6].

Knowing the 1-dB compression point of the receiver allows the gains of the RF and IF amplifiers to be correctly set for a particular input signal power. The AD9862 datasheet

states a maximum analogue input voltage range of 2 $V_{p\text{-}p}$ for an input impedance of 200 Ω. This is equivalent to an input signal power level of 7 dBm. Each 6 dB decrease in input signal power level will result in a 6 dB loss of A/D converter dynamic range. To determine the 1-dB compression point of the receiver, the setup shown in Figure 3.3 was used.

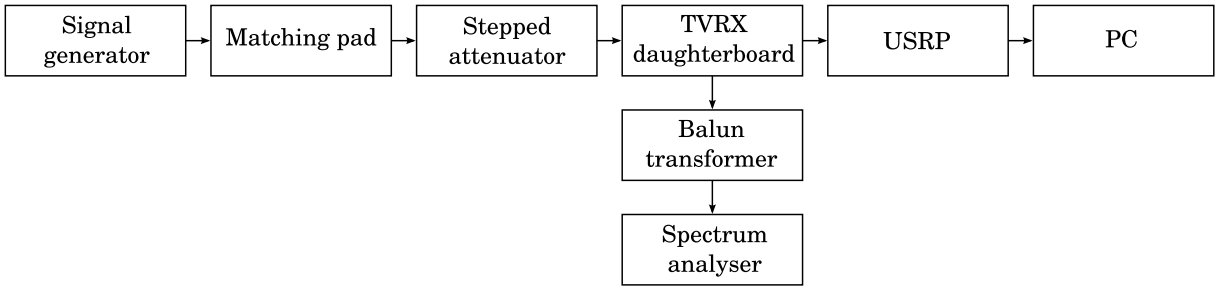

Figure 3.3: A block diagram of the experimental setup that was used to determine the 1-dB compression point of the receiver.

A Hewlett-Packard[2] HP 8656B signal generator was used to generate a 95.3 MHz, 5.8 dBm tone. A Mini-Circuits[3] BMP-5075R+ matching pad was used to match the 50 Ω output of the signal generator to the 75 Ω input of the stepped attenuator. The matching pad and stepped attenuator resulted in a power loss of 5.8 dBm. The signal power at the input of the the TVRX daughterboard was therefore equal to 0 dBm. A Mini-Circuits T4-1-X65 balun transformer was used to transform the 200 Ω balanced output of the daughterboard to a 50 Ω unbalanced output. An Agilent[4] E4407B spectrum analyser was used to measure the signal power at the 50 Ω output. Figure 3.4 shows a picture of the test equipment that was used.

For the experiment, a GNURadio application was written to set the gains of the RF and IF amplifiers independently. To determine the maximum RF and IF amplifier gain settings, the datasheet of the module was consulted. Figure 3.5 shows the gain curves of the RF amplifier, while Figure 3.6 shows the gain curve of the IF amplifier.

Based on Figures 3.5 and 3.6, it was decided to limit the maximum RF and IF amplifier gain settings to 40 dB and 30 dB respectively. The stepped attenuator was now used to decrease the power of the signal delivered to the TVRX daughterboard in 5 dB-steps, while measuring the output power of the signal with the spectrum analyser. This was repeated for a number of different gain settings. Figure 3.7 shows the plots of the data that was obtained.

[2]Accessed 20 February 2010, <http://www.hp.com>.
[3]Accessed 20 February 2010, <http://www.minicircuits.com>.
[4]Accessed 20 February 2010, <http://www.agilent.com>.

Figure 3.4: A picture of the experimental setup that was used to determine the 1-dB compression point of the receiver.

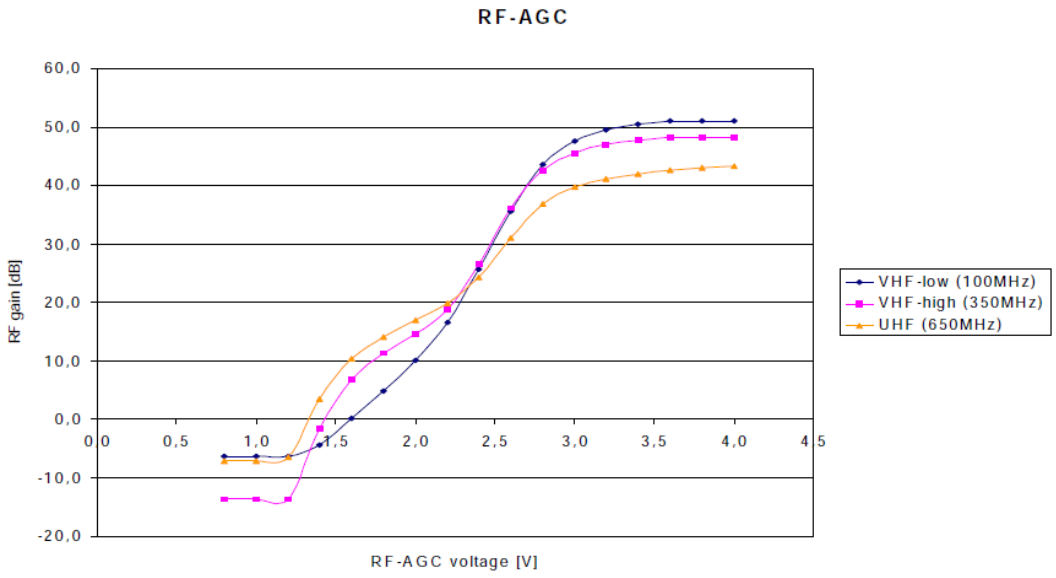

Figure 3.5: The gain curves of the RF amplifier, as provided in the datasheet.

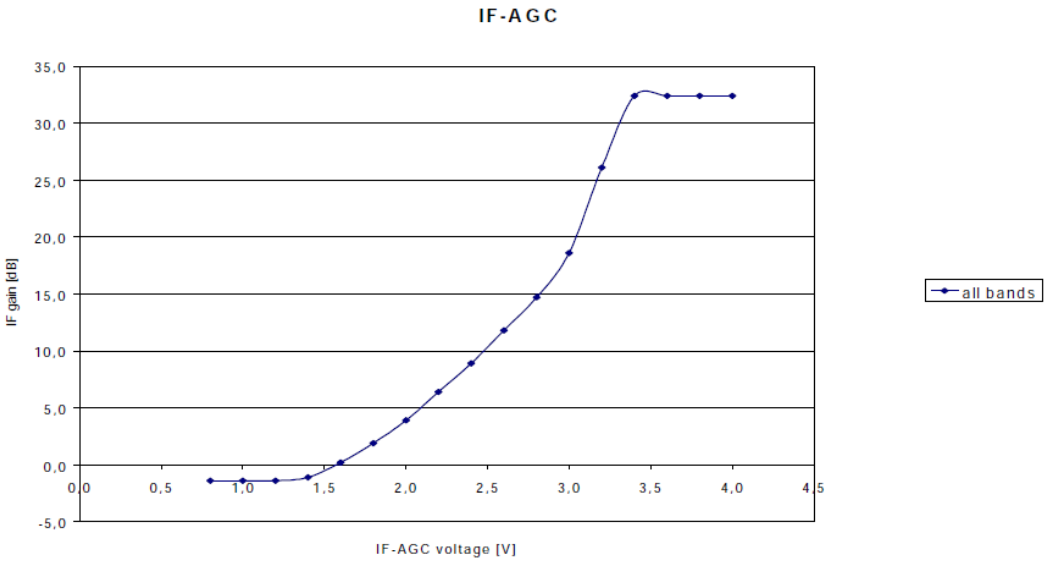

Figure 3.6: The gain curve of the IF amplifier, as provided in the datasheet.

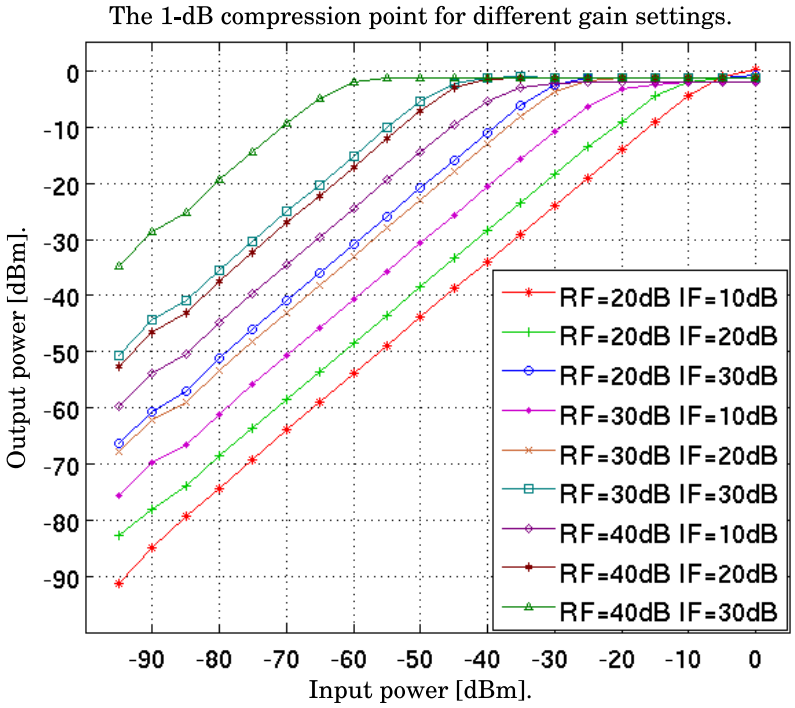

Figure 3.7: Plots of the receiver output power against input power for different gain settings.

For all the gain settings, the receiver has a 1-dB compression point of approximately -5 dBm. For an RF amplifier gain setting of 20 dB and an IF amplifier gain setting of 10 dB, the receiver has a linear response for an output signal power range of -80 to -5 dBm. The receiver therefore has a maximum linear dynamic range of approximately 75 dBm.

Third-Order Intercept Point

The IP_3 of a receiver is the theoretical point at which the curves of the linear output and the third-order distortion products intersect [6]. Third-order distortion products are produced due to the interaction of two signals in the receiver. Given two input signals with frequencies f_1 and f_2, a receiver will produce third-order distortion products at frequencies $2f_1 - f_2$ and $2f_2 - f_1$. These unwanted components fall within the passband of the receiver. Each 1 dB increase in input signal power results in a third-order distortion product power increase of 3 dB [34]. Figure 3.8 shows an illustration of the IP_3, while Figure 3.9 shows the setup that was used to determine the IP_3 of the receiver.

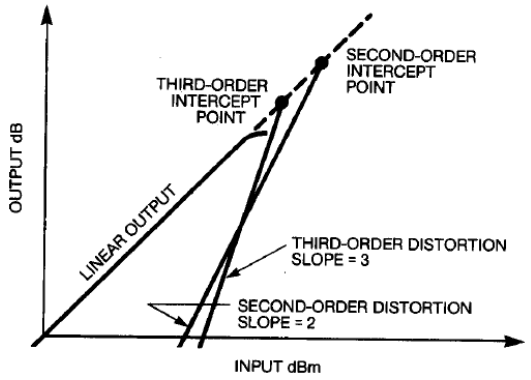

Figure 3.8: An illustration of the IP_3 [6].

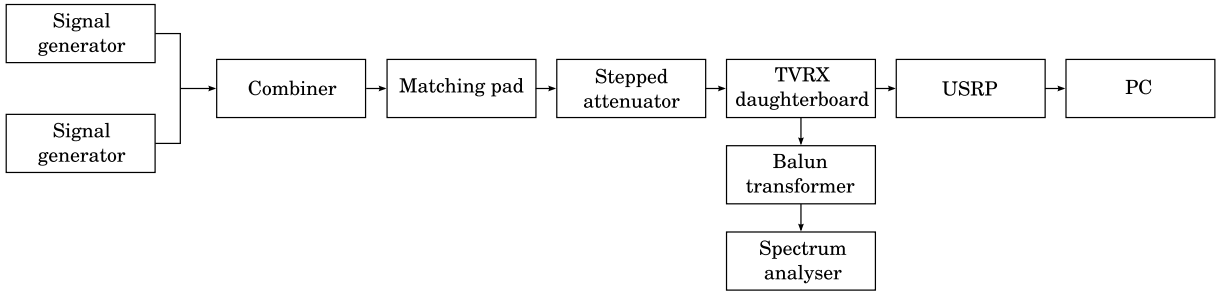

Figure 3.9: A block diagram of the experimental setup that was used to determine the IP_3 of the receiver.

The setup is similar to the setup used to determine the 1-dB compression point of the receiver, with the addition of an Agilent E4400B signal generator and a combiner. Figure 3.10 shows a picture of the test equipment that was used for this experiment.

Figure 3.10: A picture of the experimental setup that was used to determine the IP_3 of the receiver.

For the experiment, the HP 8656B signal generator was used to generate a 100 MHz, 14.7 dBm tone, while the E4400B signal generator was used to generate a 100.02 MHz, 14.6 dBm tone. At these power levels, it was found that both signal generators delivered signals with a power of level 5 dBm to the input of the TVRX daughterboard. The TVRX daughterboard was tuned to a frequency of 100 MHz. This resulted in the desired signals appearing at output frequencies of 43.98 MHz and 44 MHz, while their third-order distortion products appeared at frequencies of 43.96 MHz and 44.02 MHz. The stepped attenuator was used to decrease the input signal power in 5 dB-steps, while the power of the desired and third-order distortion products were measured with the spectrum analyser. Figure 3.11 shows a plot of the data that was obtained.

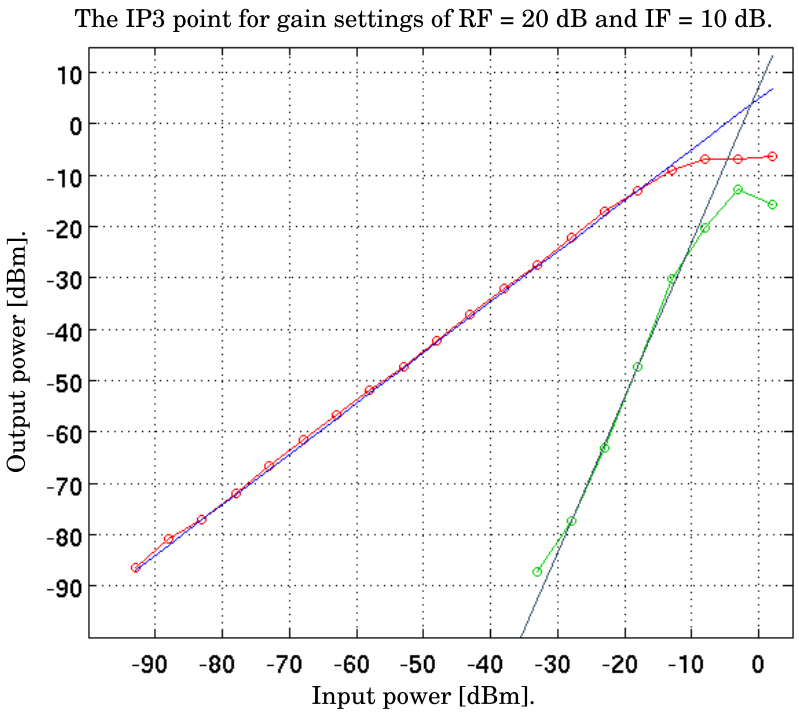

Figure 3.11: Plot of the receiver output power and third-order distortion product power against input power for gain settings of RF = 20 dB and IF = 10 dB.

The receiver has an IP_3 of approximately 4 dBm. The spur-free dynamic range (SFDR) of a receiver is the difference between the desired signal output power and the power of the third-order distortion products, at the input signal power where the third-order distortion products are first visible above the noise [35]. Figure 3.11 shows that the receiver has an SFDR of approximately 60 dB.

Receiver Bandwidth

The datasheet of the module specifies a receiver bandwidth of 6 MHz. To verify this, a test setup identical to the setup that was used to determine the 1-dB compression point of the receiver was used. The HP 8656B function generator was used to generate a 94 MHz, -20 dBm tone, while the RF and IF amplifiers were set to gains of 20 dB and 10 dB respectively. The TVRX daughterboard was tuned in 200 kHz-steps, starting at 89 MHz and ending at 99 MHz, while the resulting output power at the corresponding IF was measured with the spectrum analyser. Figure 3.12 shows a plot of the data that was obtained.

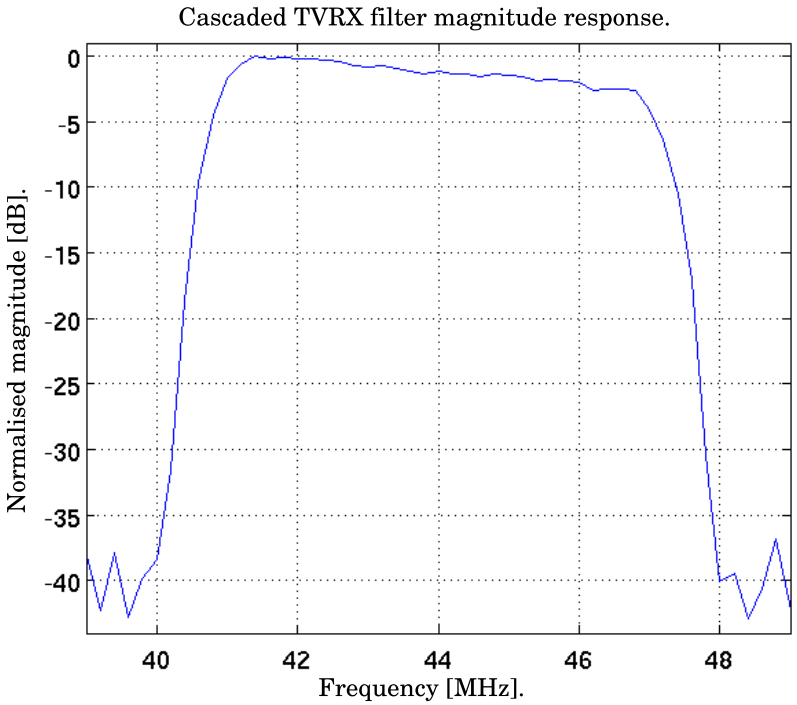

Figure 3.12: The cascaded magnitude response of the TVRX daughterboard filters.

It can be seen that the receiver has a bandwidth of 6 MHz, with an out-of-band attenuation of 40 dB. The magnitude response shows a variation of approximately 2 dB across the passband of the receiver.

3.2 Bandpass Filter Design

Figure 3.13 shows the FM band, as measured at UCT. A folded dipole antenna, along with the E4407B spectrum analyser, was used to capture the data.

For the experimental PCL radar system, two potential transmitters were identified, namely the Constantiaberg and Tygerberg transmitters. As shown in Chapter 2, FM signals modulated by music are more suitable for PCL radar than FM signals modulated by speech, due to the superior range resolution. Two radio stations that broadcast a lot of musical content and are transmitted by both the Constantiaberg and Tygerberg transmitters, are 5FM and Radio Good Hope. The Tygerberg transmitter transmits 5FM at 88.2 MHz and Radio Good Hope at 96.2 MHz, while the Constantiaberg transmitter transmits 5FM at 89 MHz and Radio Good Hope at 95.3 MHz. These radio stations are visible on Figure 3.13. A very strong radio station is also visible at 104.5 MHz. This radio station is known as UCT FM and is transmitted from the UCT campus.

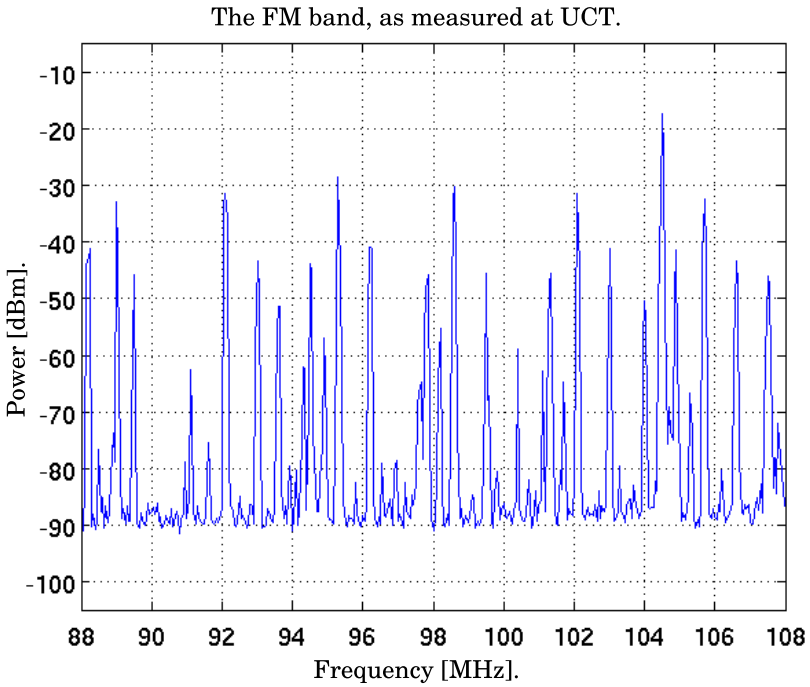

Figure 3.13: The FM band, as measured at UCT.

For the experimental PCL radar system, it was decided to utilise the 5FM radio station. This station is located at the lower end of the FM band. It would therefore be easier to design a bandpass filter based on shunt-mounted resonators to attenuate signals at higher frequencies in the FM band. The RF filter design procedure detailed in Devlin [36] was used to design the bandpass filter, while the Genesys software from Agilent was used to simulate its performance. Figure 3.14 shows the schematic of the filter that was designed and simulated.

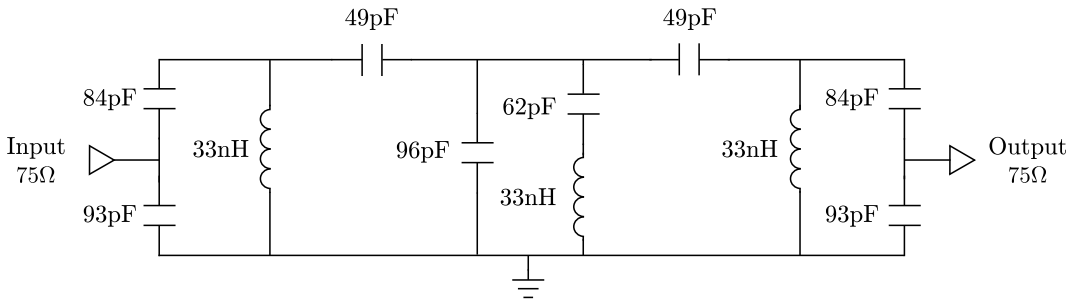

Figure 3.14: A schematic of the bandpass filter that was designed and simulated. Note the capacitor in series with the centre inductor.

A capacitor was included in series with the inductor of the centre resonator. This introduces a rejection notch at 104.5 MHz and should help to significantly attenuate the UCT FM radio station.

To simulate the filter, each capacitor was modelled as having an equivalent series resistance (ESR) of 0.05 Ω. The datasheet of the Johanson Technology[5] R14-range of capacitors that were used in the filter states that all the capacitors have an ESR that is close to this value. The Q-factor of the inductors was also limited to 100. The datasheet of the Coilcraft[6] 1812-range of inductors states that the 33 nH inductors have a Q-factor of approximately 100 at 100 MHz. Furthermore, the effect of the PCB tracks and the FR-4 substrate that was used to construct the filter was also accounted for in the simulation. These extra measures ensured a more accurate simulation of the final filter. Figure 3.15 shows the simulated scattering parameters of the filter.

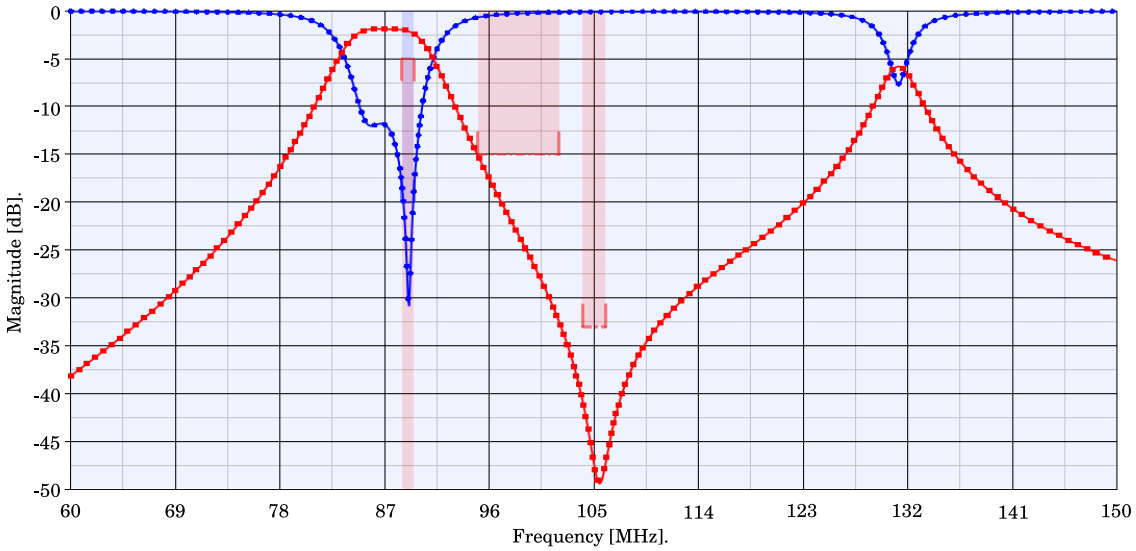

Figure 3.15: The simulated scattering parameters of the bandpass filter.

It can be seen that the simulated filter has an insertion loss of approximately 2 dB at the frequencies of interest, while the return loss is in the order of 20 dB. The simulated filter also has an attenuation of approximately 40 dB at 104.5 MHz.

The layout of the filter included wider footprints for each capacitor. The reason for this was twofold. Firstly, all the required capacitor values were not available from the manufacturer. A wider footprint meant that two capacitors could be used in parallel to obtain a value that is closer to the required value. Secondly, component tolerances caused the rejection notch to not exactly be at 104.5 MHz. By varying the value of a capacitor in parallel with the series capacitor, the position of the rejection notch could be placed at 104.5 MHz. Figure 3.16 shows the schematic of the final filter that was constructed.

[5]Accessed 20 February 2010, <http://www.johansontechnology.com>.
[6]Accessed 20 February 2010, <http://www.coilcraft.com>.

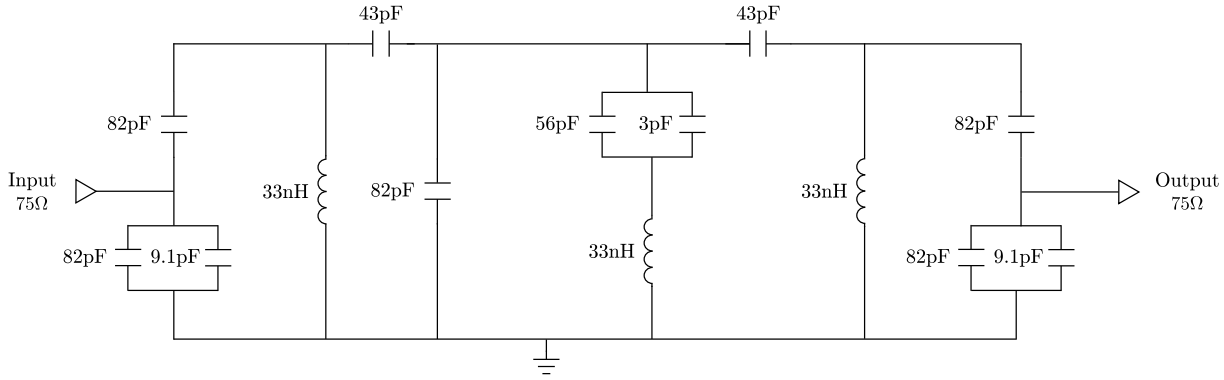

Figure 3.16: A schematic of the constructed bandpass filter. Capacitors were used in parallel to obtain values that are close to the desired values.

By comparing Figure 3.16 to Figure 3.14, it can be seen that the actual component values that were used to construct the filter are close to the values that were used to simulate the filter. Figure 3.17 shows a picture of the constructed filter.

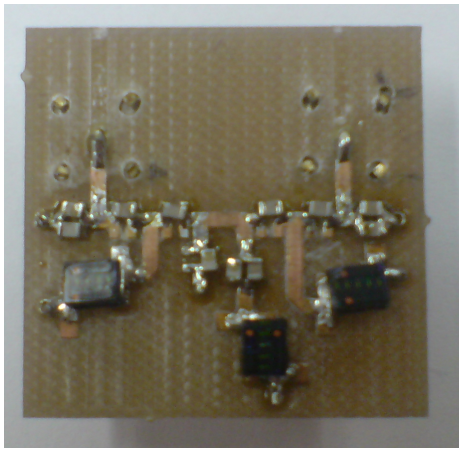

Figure 3.17: A picture of the constructed bandpass filter.

The filter has two 75 Ω BNC female connectors that are used to connect it to the receiving antenna and the TVRX daughterboard. The inductors were also placed at 90° angles to each other to minimise coupling. To measure the scattering parameters of the constructed filter, an Agilent E5071B network analyser was used. Two matching pads were used, one to match the 50 Ω impedance of the first port of the network analyser to the input of the filter and the other to match the output of the filter to the second port of the network analyser. The two matching pads and connectors that were used to connect the filter to the network analyser resulted in a loss of 11.6 dB. Figure 3.18 shows the measured insertion loss of the filter.

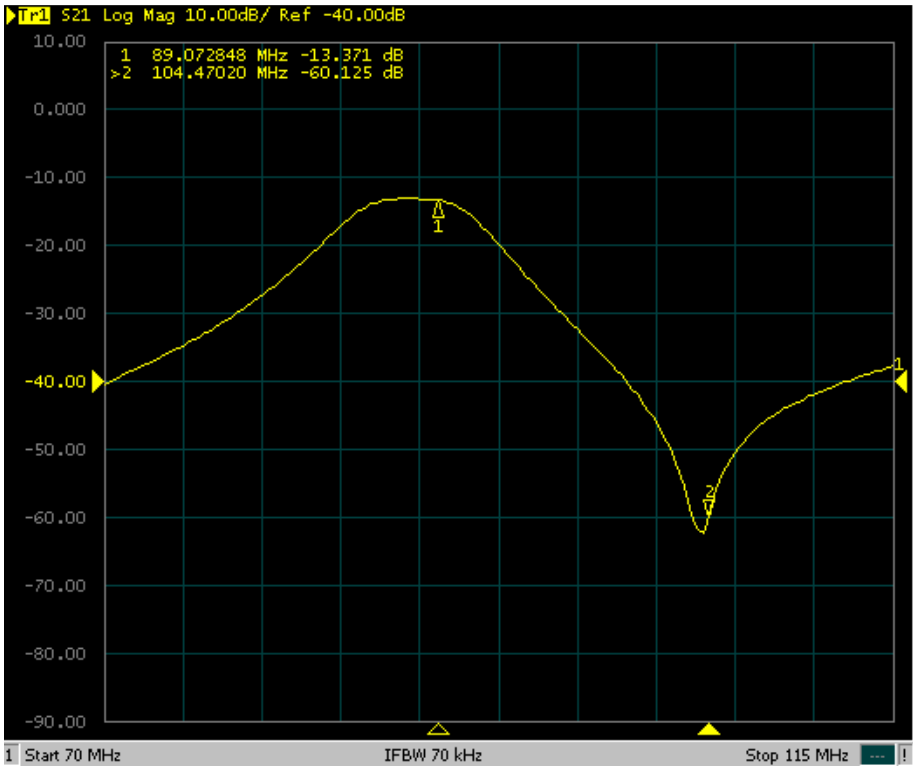

Figure 3.18: The measured insertion loss of the bandpass filter.

By taking the losses into account, it can be seen that the filter has an insertion loss of 1.8 dB at 89 MHz. The filter also has an attenuation of 48.5 dB at 104.5 MHz. Figure 3.19 shows the measured return loss of the filter.

After accounting for the losses, it can be seen that the filter has a return loss of 12.3 dB at 89 MHz. This means that 4% of the signal power is lost due to impedance mismatch. The constructed filter was duplicated so that a filter could be added to both the reference and surveillance channels. The second filter is identical to the first, with the only exception being that the capacitor in parallel with the capacitor of the centre resonator has a value of 4.7 pF instead of 3 pF. This can once again be attributed to component tolerances. It was found that the measured scattering parameters of the second filter are very similar to that of the first.

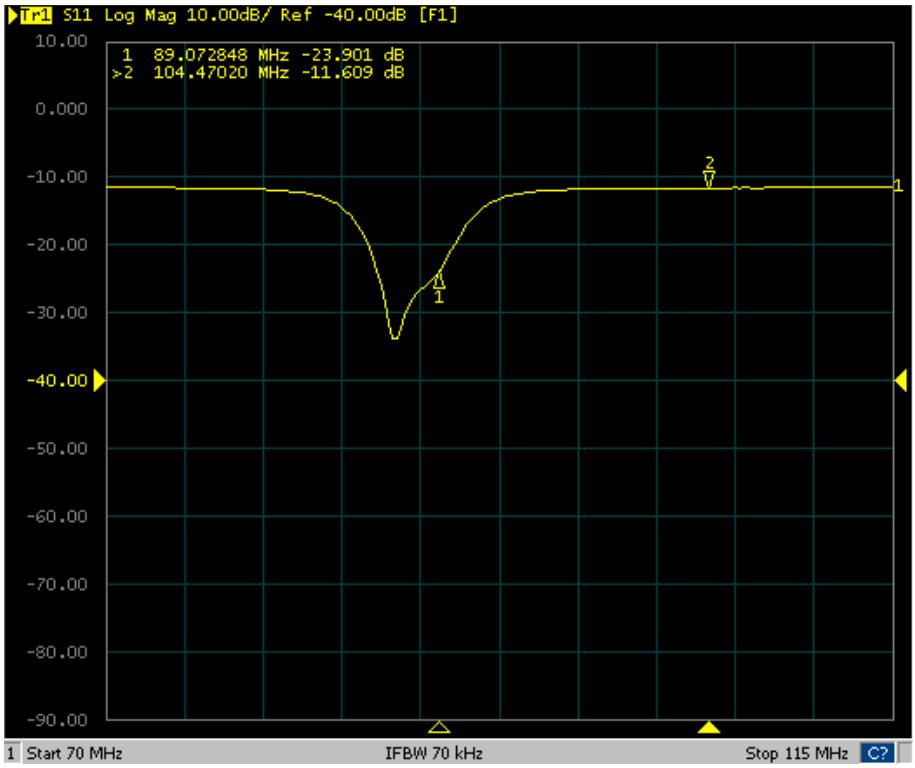

Figure 3.19: The measured return loss of the bandpass filter.

As a final test, the FM band was once again measured at UCT, this time adding the constructed bandpass filter between the folded dipole antenna and the spectrum analyser. Figure 3.20 shows a plot of the data that was obtained.

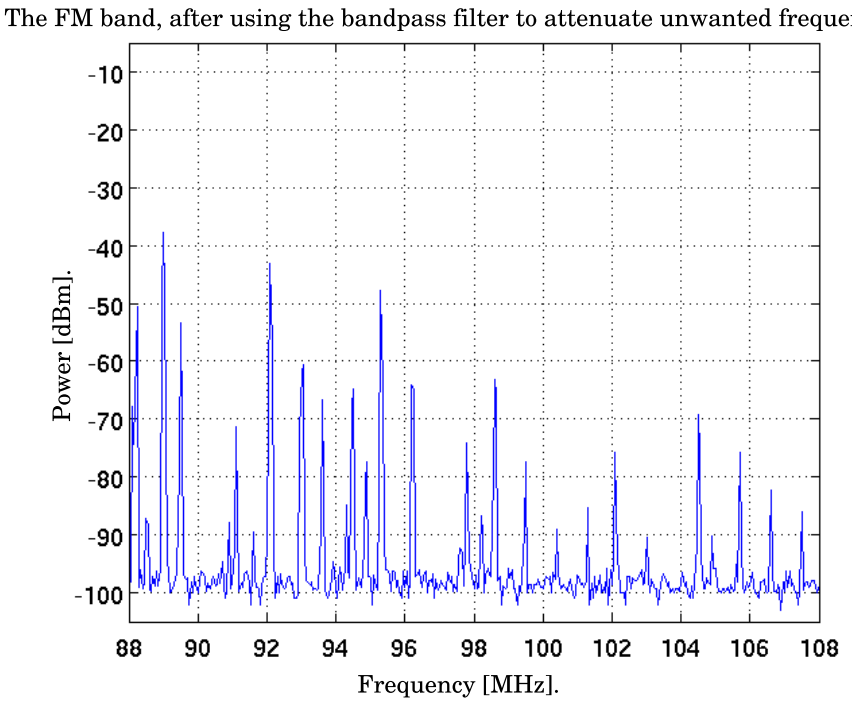

Figure 3.20: The FM band, as measured at UCT, after using the bandpass filter to attenuate higher frequencies in the FM band.

By comparing Figure 3.20 to Figure 3.13, it can be seen that frequencies above the band of interest are attenuated by the bandpass filter. The measured peak power level of the UCT FM radio station has also decreased from approximately -17 dBm to -69 dBm, indicating that the filter performs its intended function.

3.3 Chapter Summary

This chapter presented a performance analysis of the TVRX daughterboard to determine its suitability as a PCL radar receiver. In particular, the following observations were made

- The receiver has a maximum linear dynamic range of 75 dB and a 1-dB compression point of -5 dBm. To fully utilise the 72 dB of A/D converter dynamic range, an output signal power of 7 dBm is required. This means that more than 12 dB of dynamic range is lost.
- The receiver has an IP_3 of 4 dBm, which is quite poor. For a high performance receiver, the IP_3 should be in the order of 24 dBm [34]. Given the very low power of the target reflections, the receiver should suppress the third-order intermodulation products as much as possible.

- The receiver has a total bandwidth of 6 MHz, which will allow signals from multiple FM transmitters to be utilised simultaneously. The receiver attenuates out-of-band signals by 40 dB.

The TVRX daughterboard is not an ideal PCL radar receiver when used with the USRP. Its inability to fully utilise the entire A/D converter dynamic range and its low IP_3 will limit the maximum achievable detection range.

This chapter has also shown that it is possible, using a simple bandpass filter based on shunt-mounted resonators, to attenuate a single strong radio station in the FM band.

Chapter 4

The USRP FPGA

The FPGA on the USRP is tasked with performing the digital upconversion and digital downconversion of signals, while a standard PC is used for all the waveform-specific processing. The firmware on the FPGA is written in the Verilog[1] hardware description language (HDL) and synthesised using the Quartus II Web Edition software, available for free download from the Altera website. This chapter presents an analysis of the signal processing stages used in the receive chain of the FPGA. PCL radar only requires the reception of signals and therefore, the transmit chain of the FPGA will not be considered. The Icarus[2] Verilog simulation Tool is used to simulate each stage. The filtering stages are also evaluated using the Matlab[3] Filter Visualisation Tool. Possible improvements are then identified. Any unnecessary functionality is removed from the Verilog code to free up logic resources. These resources are used to improve the signal processing stages of the receive chain. The improved stages are first simulated using Icarus Verilog, along with the GTKWave[4] viewer, before being integrated into the existing Verilog code. The new Verilog code is then synthesised and the firmware loaded on to the FPGA. This chapter concludes with a discussion of the results of the simulations and the improvements that were made to the FPGA build.

4.1 The Standard FPGA Build

The USRP is shipped with firmware containing two transmit and two receive paths. A block diagram of two complex receive paths is shown in Figure 4.1.

[1]Accessed 27 February 2010, <http://www.verilog.com>.
[2]Accessed 24 December 2009, <http://www.icarus.com/eda/verilog>.
[3]Accessed 24 December 2009, <http://www.mathworks.com/products/matlab.
[4]Accessed 24 December 2009, <http://gtkwave.sourceforge.net>.

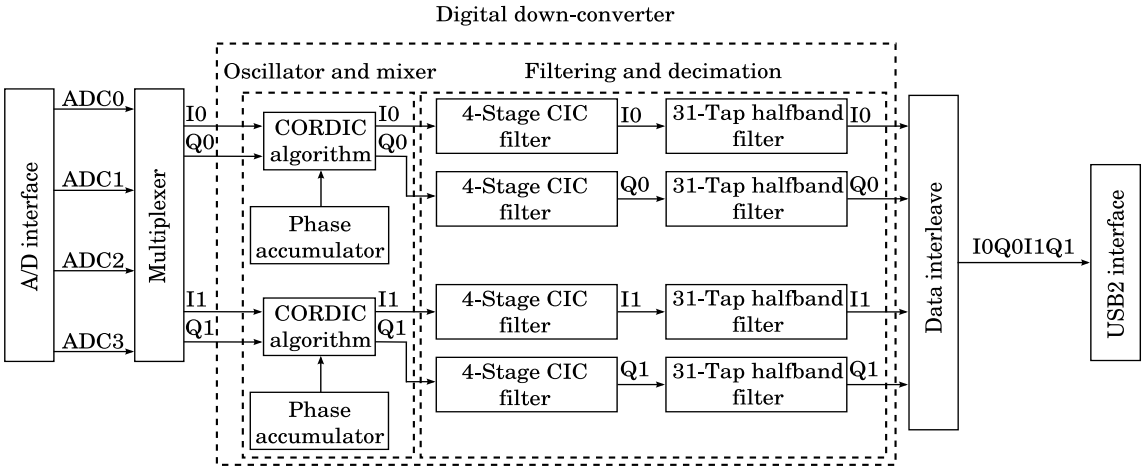

Figure 4.1: A block diagram showing the A/D converter interface, USB 2 interface and two complex DDCs of the USRP.

4.1.1 A/D Interface

The A/D interface receives 12-bit two's complement samples from the A/D converter. Each sample is then sign-extended to 16 bits and passed on to the multiplexer.

4.1.2 Multiplexer

The multiplexer determines which A/D converter inputs are connected to which I and Q paths of the USRP receive chain. The multiplexer is set from a GNURadio application using a 32-bit binary value. When using a TVRX daughterboard, a constant zero is connected to the Q-outputs of the multiplexer.

4.1.3 Oscillator and Mixer

In any DDC, the most performance critical component is the digital oscillator [37]. The oscillator generates a sampled sinusoid, which is multiplied with the incoming signal to shift its spectrum. Phase errors in the oscillator lead to spurious spectral components, while amplitude errors lead to a decrease in signal-to-noise ratio (SNR). On the USRP, the oscillator and mixer are implemented as a phase accumulator and the COordinate Rotation DIgital Computer (CORDIC) algorithm.

Phase Accumulator

The phase accumulator is used to integrate a 32-bit phase increment value, which is then passed to the CORDIC algorithm.

The phase increment value is set by the GNURadio application running on the host PC and is calculated as follows

$$\text{phase increment} = \frac{f}{64000000} \times 2^{32} \tag{4.1}$$

where f is the desired frequency that the digital oscillator needs to generate. The oscillator operates from -32 MHz to 32 MHz. The minimum tunable frequency of the oscillator is controlled by the resolution of the phase accumulator. For the phase accumulator on the USRP, the frequency resolution is given by

$$\begin{aligned} \text{frequency resolution} &= \tfrac{64000000}{2^{32}} \\ &= 0.0149\,\text{Hz} \end{aligned} \tag{4.2}$$

It should be noted that the phase accumulator does not influence the noise performance of the oscillator. Reducing the word width of the phase accumulator only reduces the amount of frequencies that can be synthesised [37].

CORDIC Algorithm

In a DDC, the phase accumulator is often followed by a waveform synthesiser and a pair of multipliers. The waveform synthesiser uses a lookup table to convert the phase value received from the phase accumulator to the corresponding cosine and sine values. The incoming signal is then multiplied by $\cos(\omega t) - j\sin(\omega t) = \exp(-j\omega t)$. The nett effect of multiplying the input signal therefore rotates it by a constantly changing phase angle. An alternative approach to using a waveform synthesiser and a pair of multipliers is to directly rotate the input signal using the CORDIC algorithm [37].

The trigonometric CORDIC algorithms were originally developed by Jack Volder to solve real-time navigation problems. Since then, CORDIC theory has been extended to include a variety of applications. Examples are found in radar signal processors, robotics and the Hewlett Packard HP-35 calculator [38]. The rotational mode CORDIC is derived from the general rotation transform given by

$$\begin{aligned} x' &= x\cos\phi - y\sin\phi \\ y' &= y\cos\phi + x\sin\phi \end{aligned} \tag{4.3}$$

which rotates a vector in the Cartesian plane by an angle, ϕ. The rotation transform can also be rewritten as

$$\begin{aligned} x' &= \cos\phi \cdot [x - y\tan\phi] \\ y' &= \cos\phi \cdot [y + x\tan\phi] \end{aligned} \tag{4.4}$$

If the rotation angles are restricted to values where $\tan\phi = \pm 2^{-i}$, the multiplication by the tangent can be replaced by a simple bit-shift operation. The input vector can be rotated by arbitrary angle values if rotations by successively smaller angles are performed. If we denote the rotation direction by d, the cosine term can be replaced by a constant, K, since $\cos(\phi) = \cos(-\phi)$. The vector rotation at the i^{th} stage is now given by

$$\begin{aligned} x_{i+1} &= K_i \cdot [x_i - y_i \cdot d_i \cdot 2^{-i}] \\ y_{i+1} &= K_i \cdot [y_i + x_i \cdot d_i \cdot 2^{-i}] \end{aligned} \tag{4.5}$$

where $K_i = \cos(\tan^{-1} 2^{-i})$ and $d = \pm 1$, depending on the rotation direction for the current stage. The total gain obtained by multiplying the rotated vector by K_i at each stage approaches 1.647. This value can be treated as part of the total system gain, allowing the multiplication operation to be removed. The result is a vector rotation algorithm using only bit-shift and add operations. To keep track of the residual angle, a third equation is added

$$z_{i+1} = z_i - d_i \cdot \tan^{-1}(2^{-i}) \tag{4.6}$$

If the residual angle at the i^{th} stage is positive, the vector is rotated clockwise and the angle for the current stage, $\tan^{-1}(2^{-i})$, is subtracted from previous residual angle. For negative residual angles, the vector is rotated counterclockwise and the angle for the current stage is added to the residual angle. The rotation angle at each stage can be precomputed and stored as a constant in the FPGA. The output of the final CORDIC stage consists of an I-Q sample pair and a residual angle, z_{i+1}. This final residual angle represents the error in the vector rotation. The CORDIC algorithm on the USRP uses twelve rotation iterations and has 14 bits of amplitude resolution. In general, CORDIC algorithms produce one additional bit of phase accuracy for each iteration [38]. The CORDIC on the USRP is therefore expected to have an SFDR of approximately 72 dB and a SNR of 84 dB.

CORDIC Simulation

To verify the operation of the CORDIC algorithm on the USRP, a simulation was performed. A single real tone with a frequency of 20 MHz was generated, quantisised to 12 bits and converted to 16-bit two's complement representation to create an input signal. 6.4 million samples were used, corresponding to 100 ms of sampled signal on the USRP. The generated signal was then used as input signal to an Icarus Verilog simulation. The simulation used the phase accumulator and CORDIC algorithm on

the USRP to mix the input signal down to a frequency of 10 Hz. The output signal was then converted back to decimal representation and analysed in Matlab. Figure 4.2 shows the output signal spectrum, while Figure 4.3 shows the area around 0 in more detail.

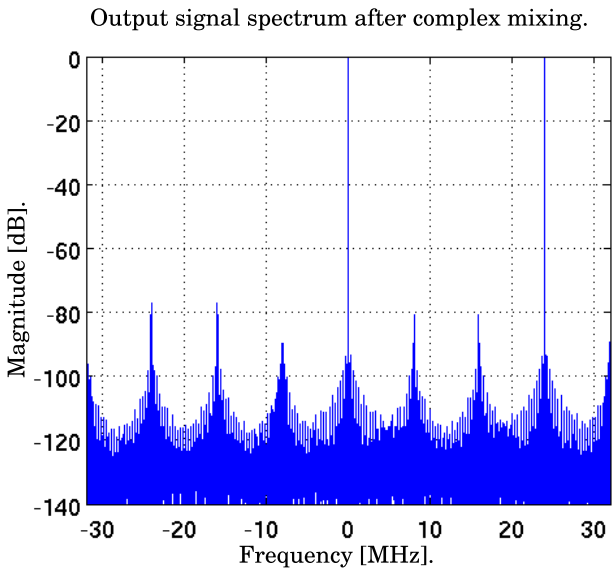

Figure 4.2: The output signal spectrum of the CORDIC simulation.

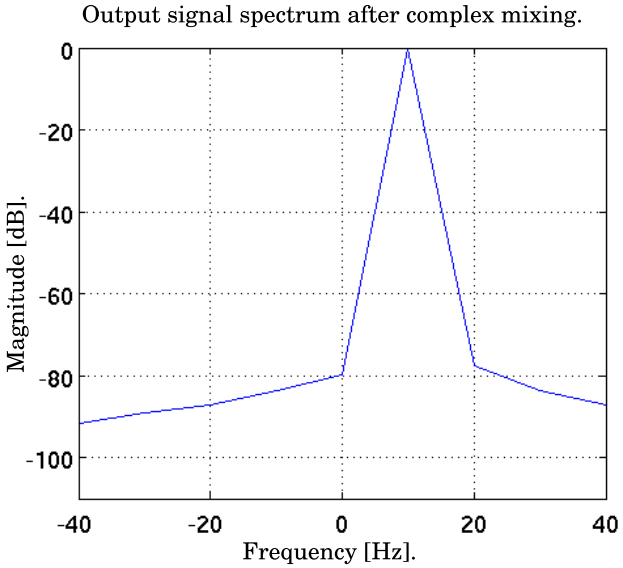

Figure 4.3: The output signal spectrum, showing the area around 0 in more detail.

Figure 4.2 shows two major components. The signal at 10 Hz is the desired signal, mixed down from 20 MHz. Because of the mixing process, an image frequency results at 20 MHz + 19.999990 MHz. The sampling frequency of 64 MHz causes the signal at the image frequency to alias down to 24.000010 MHz. It can also be seen that

the spuruous components are approximately 75 dB below the desired signal, which compares well to the theoretical value.

4.1.4 Filtering and Decimation

On the USRP, filtering and decimation is needed to decrease the sampling rate of signals from 64 MSPS to a lower value. The reason for this is twofold. Firstly, the USRP uses a USB 2 interface to transfer samples to a PC. The theoretical maximum transfer rate of the USB 2 interface is 60 MB/s. Due to packet signaling and other overhead, the actual transfer rate that the USRP can sustain is 32 MB/s. Each I-Q sample pair passing through the USRP is represented using 4 bytes. The maximum single channel transfer rate is therefore

$$\begin{aligned} \text{Maximum rate} &= \tfrac{32\ \text{MB/s}}{4\ \text{bytes}} \\ &= 8\ \text{MSPS} \end{aligned} \tag{4.7}$$

PCL radar needs at least two channels. For two channels, the maximum transfer rate equals 4 MSPS per channel. To reduce the sampling rate of a signal from 64 MSPS to 4 MSPS, a decimation factor of 16 is needed. The second reason for decimation is to lower the data rate so that a standard CPU can process signals in realtime.

Decimation always needs to be preceded by lowpass-filtering, or else, aliasing will occur. Figure 4.4 illustrates a case where a complex signal with a bandwidth of 20 MHz is decimated from a sampling frequency of 64 MHz, down to a sampling frequency of 16 MHz without first lowpass-filtering. Aliasing occurs in the shaded area, leading to a loss of signal bandwidth. In Figure 4.5, the same signal is first lowpass-filtered to reject signal components above 8 MHz, before being decimated. No aliasing occurs in this case.

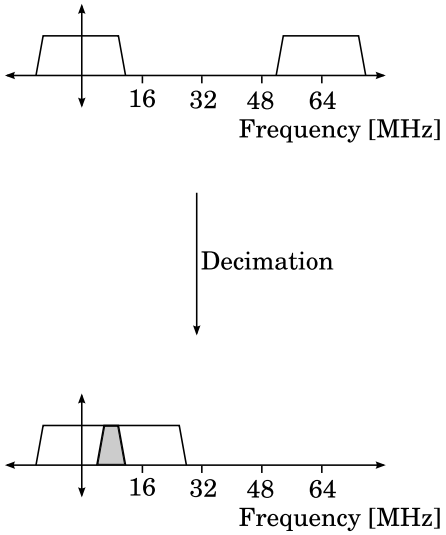

Figure 4.4: Decimation without first lowpass-filtering and the resulting aliasing that occurs.

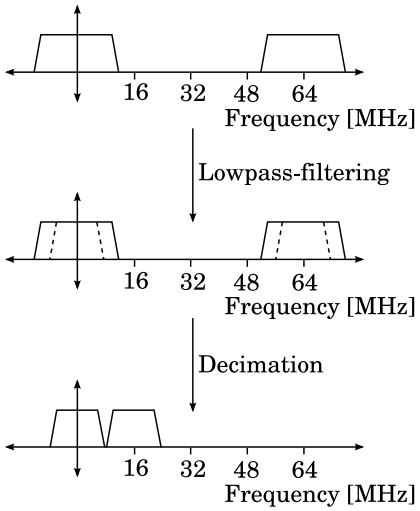

Figure 4.5: Lowpass-filtering, followed by decimation. No aliasing occurs in this case.

CIC Filter

As previously discussed, the maximum single channel sampling rate when using two channels on the USRP, is 4 MSPS. To avoid aliasing due to decimation, a lowpass filter that rejects signal components above 2 MHz is needed. Using a digital finite impulse response (FIR) filter would require a large amount of multipliers and coefficient storage. Unfortunately, the FPGA on the USRP does not possess a large number of logic elements (LEs) and therefore a more economical approach is needed.

Cascaded integrator-comb (CIC) filters are a class of decimation and interpolation filters that are often used when signals need to be decimated or interpolated by large factors. CIC filters have the desirable properties that 1) they require no multipliers; 2) no filter coefficients need to be stored; 3) they consist of two basic building blocks, allowing the order to be easily extended; 4) they are capable of a large range of decimation and interpolation factors [39]. Figure 4.6 shows a single section CIC filter.

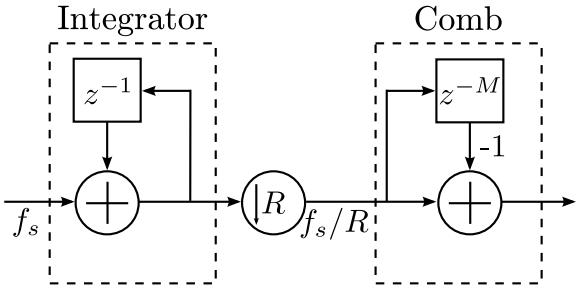

Figure 4.6: Block diagram of a single section CIC filter [7].

The basic building blocks of a CIC filter are an integrator, a down-sampler and a comb. The transfer function for an integrator is given by

$$H_I(z) = \frac{1}{1 - z^{-1}} \tag{4.8}$$

and that of a comb by

$$H_C(z) = 1 - z^{-RM} \tag{4.9}$$

where R is the rate change of the down-sampler and M is a design parameter, known as the *differential delay*. In practice, a value of 1 or 2 is usually used for M. It can be seen that an integrator is a single-pole infinite impulse response (IIR) filter with unity feedback and that a comb is simply an odd-symmetric FIR filter [7]. To increase the number of sections in a CIC filter, additional integrator-comb pairs are added. The transfer function of an N-section CIC filter is given by

$$H(z) = \frac{(1 - z^{-RM})^N}{(1 - z^{-1})^N} = \left(\sum_{k=0}^{RM-1} z^{-k} \right)^N \tag{4.10}$$

which shows that the total transfer function is equivalent to that of N FIR filters, each with a rectangular impulse response. All the coefficients of these FIR filters are unity and therefore a CIC filter has a linear phase response and constant group delay [7]. CIC filters also have large gains. For an N-section filter, the gain is given by

$$G = (RM)^N \tag{4.11}$$

Using two's complement arithmetic, the bit growth can be calculated as

$$B = N \log_2(RM) \tag{4.12}$$

Therefore, to implement a CIC filter on an FPGA, samples first need to be sign-extended by B-bits before filtering. Samples at the output of the CIC filter are then rounded or

truncated to return them to the original bit-width. The standard CIC filters on the USRP have four sections and a differential delay of one. For the maximum sampling rate when two channels are used, the CIC filters on the USRP decimate input signals by a factor of 8. The Matlab Filter Visualisation Tool was used to obtain Figure 4.7, which shows the magnitude response of the CIC filters on the USRP. Figure 4.8 shows the area from 0 to 10 MHz in more detail.

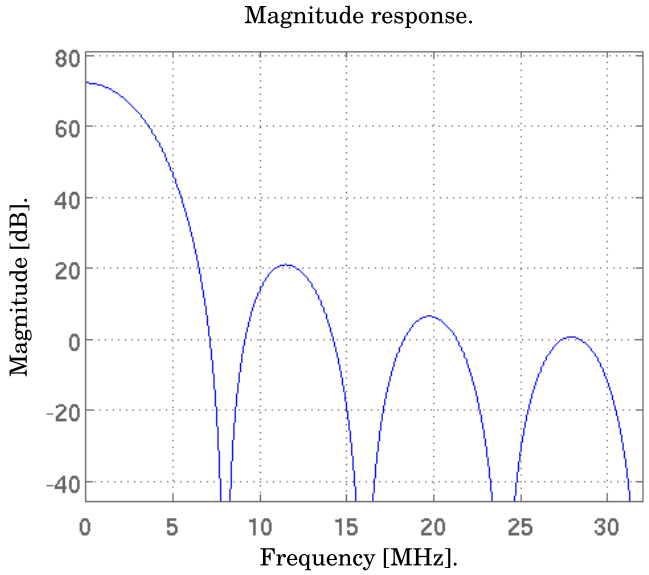

Figure 4.7: The magnitude response of a 4-section CIC filter with $R = 8$ and $M = 1$.

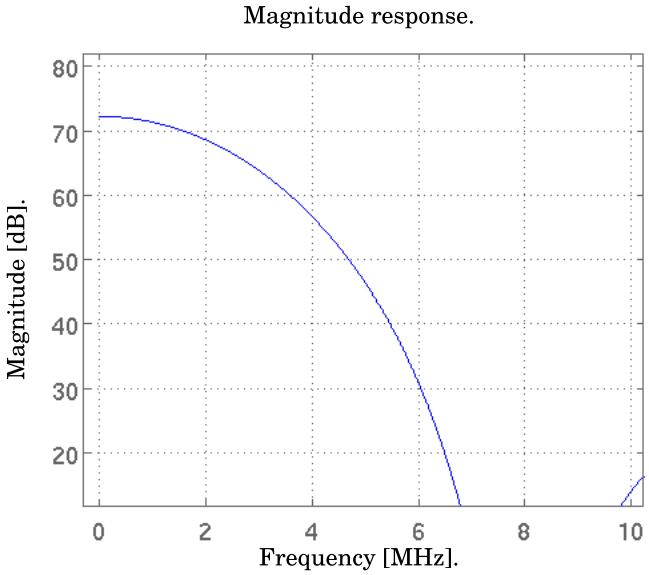

Figure 4.8: The 4-section CIC filter magnitude response from 0 to 10 MHz.

When capturing complex signals with the USRP, the final band of interest lies between -2 MHz and 2 MHz. Using the CIC filter to decimate down to a sampling frequency of 8 MHz will cause the spectral components between 6 MHz and 10 MHz to alias down to our desired signal band. It can be seen from Figure 4.8 that unwanted spectral components are attenuated by approximately 40 to 60 dB before being aliased. Figures 4.7 and 4.8 also reveal that CIC filters have an unwanted rolloff in the passband. In this case, the magnitude response drops by approximately 3 dB between 0 and 2 MHz. Increasing any of the three parameters associated with a CIC filter increases this rolloff.

CIC Filter Simulations

To verify the operation of the CIC filters on the USRP, two simulations were performed. The first simulation was aimed at comparing the passband magnitude response of the CIC filters on the USRP to the plots obtained with the Matlab Filter Visualisation Tool. Signal tones were generated every 500 kHz, from 500 kHz to 4 MHz and added to create in input signal. The signal was then converted to 16-bit two's complement representation using the procedure described for the CORDIC simulation, before using Icarus Verilog to simulate the CIC filters on the USRP when decimating a signal from a sampling rate of 64 MSPS to a sampling rate of 8 MSPS. The simulation output for the real channel is shown in Figure 4.9.

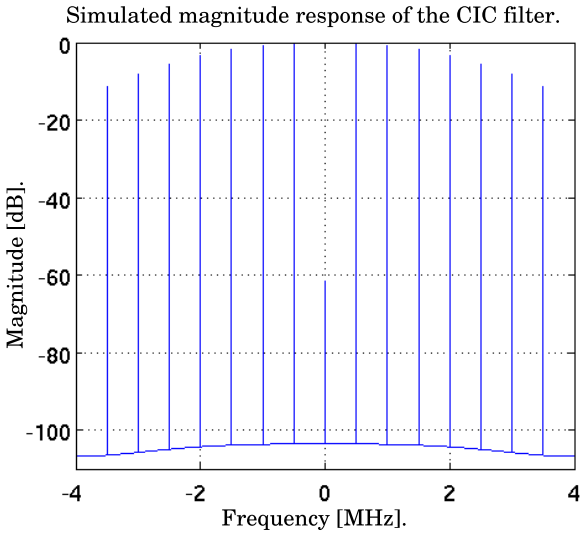

Figure 4.9: The simulated magnitude response of a 4-section CIC filter.

The passband rolloff is clearly visible. The passband response is also very similar when compared to Figure 4.8, with a 3 dB rolloff at 2 MHz.

The second CIC simulation was aimed at determining the out-of-band attenuation of unwanted signals. For this simulation, three real tones of equal magnitude were generated at 500 kHz, 6 MHz and 9.5 MHz and added to create an input signal. The signal was then converted to 16-bit two's complement representation and used as input to the Icarus Verilog simulation. Figure 4.8 shows that after CIC filtering and decimation, the tone at 6 MHz will be attenuated by about 40 dB, before aliasing down to 2 MHz, while the tone at 9.5 MHz will be attenuated by about 65 dB and alias down to 1.5 MHz. The simulation output for the real channel is shown in Figure 4.10.

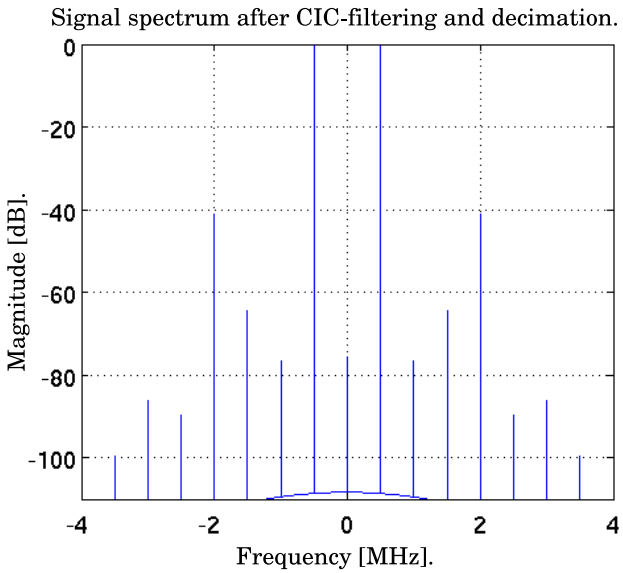

Figure 4.10: The output signal spectrum of the out-of-band attenuation simulation for the 4-section CIC filter.

The simulation output is consistent with the magnitude response obtained in Matlab. The two out-of-band signals alias back to the correct frequencies at levels that are close to the predicted values.

Halfband Filter

In FPGA-based DDCs, the CIC filter is usually followed by a final stage of filtering and decimation [37]. This filter is used to improve the final magnitude response and to decimate the input signal by a small factor. On the USRP, this final filter is implemented as a *halfband* FIR filter. Halfband filters have the property that the -3 or -6 dB cutoff frequency is located at $f_s/2$. Every second filter coefficient, apart from the centre one, is also zero, making efficient implementations possible [40]. Because halfband filters are symmetric FIR filters, they have a linear phase response.

The halfband filters on the USRP have 31 coefficients, of which 14 are zero-valued. The centre coefficient has a value of 32768, allowing the multiplication to be substituted by a bit-shift operation. The 16 remaining coefficients are all symmetric, and therefore, eight multiplications are required to produce one output value. With a maximum single channel sampling frequency of 8 MHz and a clock frequency of 64 MHz, a multiplier can be used eight times before a new input sample is accepted. Each halfband filter on the USRP therefore requires only a single multiplier. The halfband filter coefficients are located in the *coeff_rom.v* file, which can be found in the /usrp/fpga/sdr_lib directory of the GNURadio installation. The Matlab Filter Visualisation Tool was used to obtain Figure 4.11, which shows the magnitude response of one of the halfband filters when decimating from a sampling rate of 8 MSPS to a sampling rate of 4 MSPS.

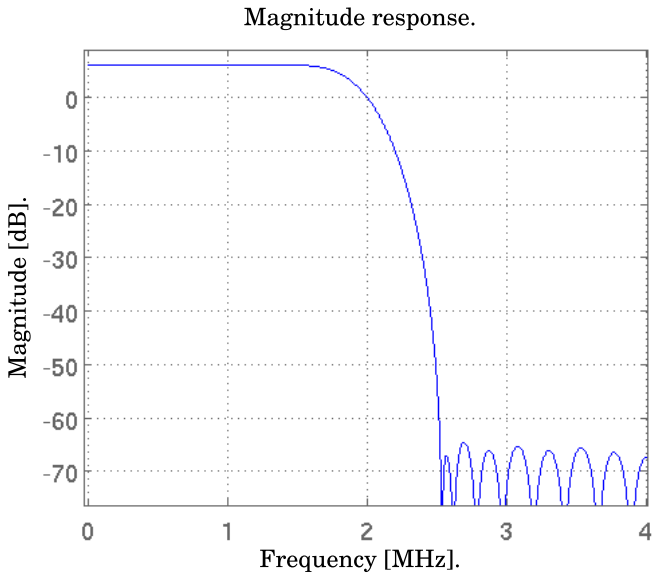

Figure 4.11: The magnitude response of the halfband filter.

Figure 4.11 confirms that the halfband filters have a -6 dB cutoff frequency at $f_s/2$. The filter gain of 6 dB indicates that the filter output grows by 1 bit and that the output samples should be rounded accordingly.

Halfband Filter Simulations

Two simulations were performed to verify the operation of the halfband filters on the USRP. The first simulation was aimed at comparing the passband magnitude response of the filters to the plot obtained with the Matlab Filter Visualisation Tool. Signal tones were generated every 300 kHz from, 300 kHz to 1.8 MHz, converted to 16-bit two's complement representation and used as input signal to an Icarus Verilog simulation. The simulation output for the real channel is shown in Figure 4.12.

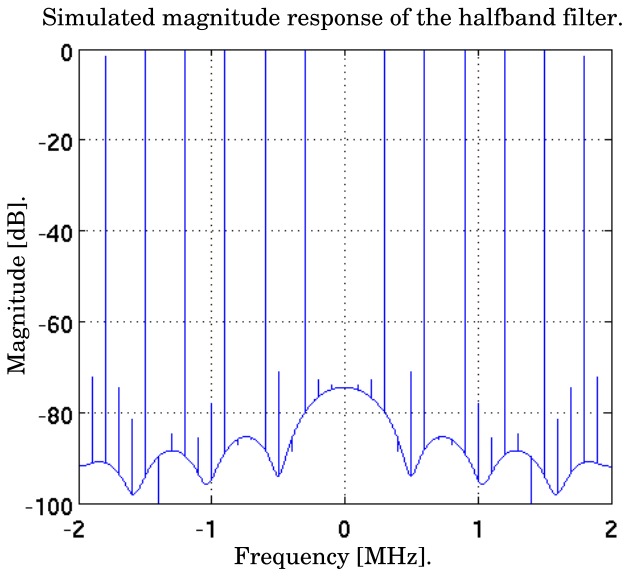

Figure 4.12: The simulated magnitude response of the halfband filter.

Figure 4.12 compares well to the magnitude response plot obtained with Matlab. Both figures indicate an attenuation of approximately 1.4 dB at 1.8 MHz.

The second Icarus Verilog simulation was aimed at determining the halfband filter's attenuation of signals above the cutoff frequency. Signal tones of equal magnitude were generated at 100 kHz, 2.1 MHz, 2.3 MHz and 2.5 MHz and added to create an input signal for the Icarus Verilog simulation. The halfband filter was then simulated when decimating an input signal from a sampling rate 8 MSPS to a sampling rate of 4 MSPS. The simulation output for the real channel is shown in Figure 4.13.

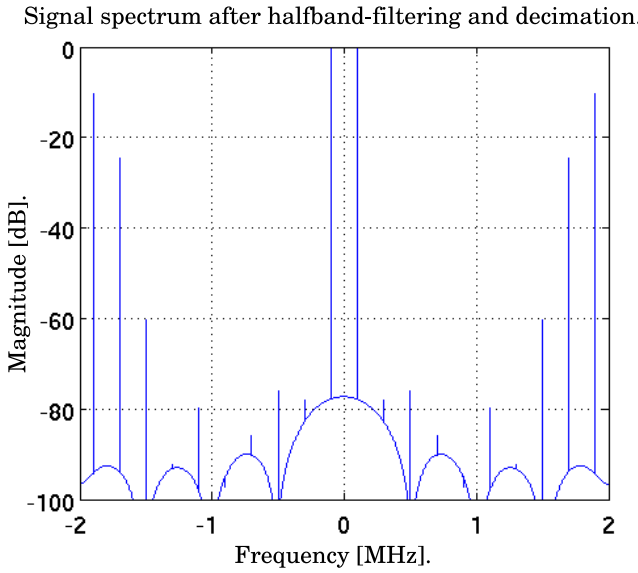

Figure 4.13: The output signal spectrum of the out-of-band attenuation simulation for the halfband filter.

The three tones that were generated above the cutoff frequency of the filter can clearly be seen, aliasing back into the band of interest. The aliasing levels are comparable to the magnitude response obtained in Matlab. Although the final complex sampling rate is 4 MSPS, the total usable bandwidth is less than 3 MHz due to the aliasing that occurs.

4.1.5 Data Interleave

The data interleave stage in the receive chain is used to transform the samples received from the separate channels into a single serial stream. This single stream of samples is then passed to the USB 2 interface. For two complex channels, the interleaved stream is sent across the USB 2 interface in the following order: I0Q0I1Q1. At the PC side, a de-interleaver is used to connect each receive chain to the appropriate signal processing blocks in the GNURadio application.

4.1.6 USB 2 Interface

The USB 2 interface receives the serial stream of samples from the data interleave stage. The samples are then stored in a First In, First Out (FIFO) buffer, before being transferred to the Cypress FX2 microcontroller. From here they are transferred to the host PC.

4.2 The Improved FPGA Build

The results of the Icarus Verilog simulations were used to identify signal processing stages that offered room for improvement. The simulation of the CORDIC algorithm showed that it has a sufficient SFDR and SNR for our required application. The frequency resolution and range of frequencies that the oscillator can generate is also sufficient. It was decided to increase the number of sections in each CIC filter to improve the attenuation of out-of-band signals. This comes at the expense of a slight increase in passband rolloff. It was also decided to replace the halfband filter in each DDC with a FIR filter that provides higher attenuation of out-of-band signals.

4.2.1 6-Section CIC Filter

The Matlab Filter Visualisation Tool was used to obtain the magnitude response of a 6-section CIC filter. Figure 4.14 shows a plot of the magnitude response, while Figure 4.15 shows the area between 0 and 10 MHz in more detail.

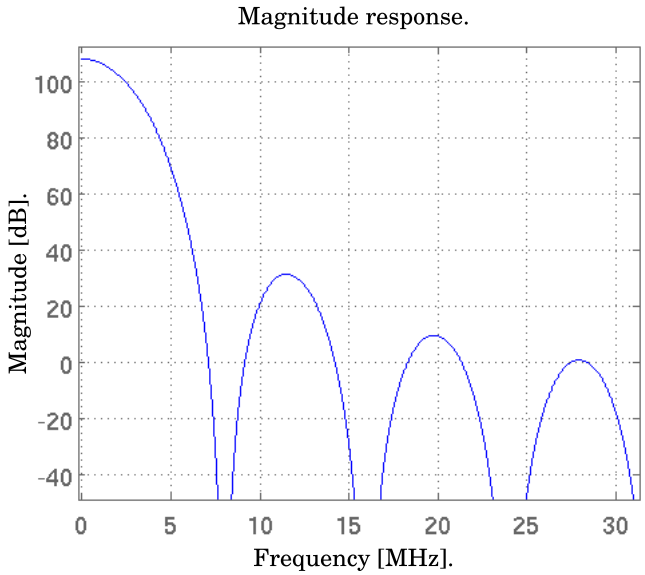

Figure 4.14: The magnitude response of a 6-section CIC filter with $R = 8$ and $M = 1$.

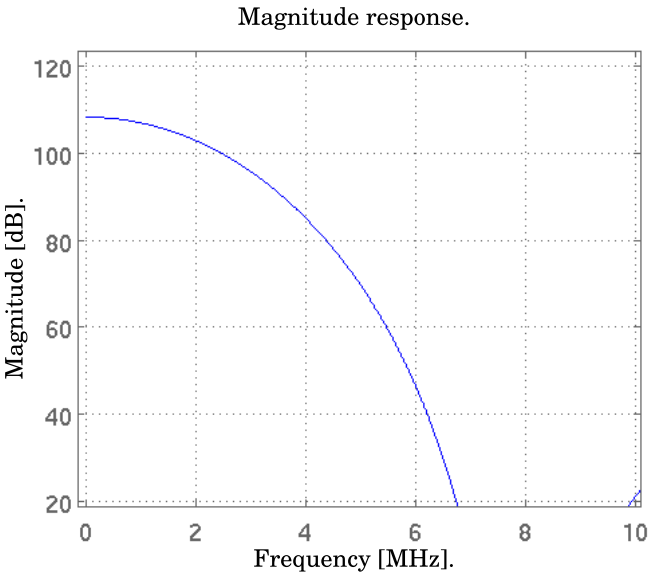

Figure 4.15: The 6-section CIC filter magnitude response from 0 to 10 MHz.

It can be seen from Figure 4.15 that the passband rolloff from 0 to 2 MHz increases to approximately 5 dB when adding two extra stages to the CIC filter. The attenuation at 6 MHz increases by about 20 dB.

6-Section CIC Filter Simulations

The Verilog code was modified to extend the CIC filters on the USRP to six sections. The new CIC filter was then simulated to compare the passband magnitude response

and out-of-band attenuation to that of the 4-section CIC filter. Figure 4.16 shows the real channel output of the simulation.

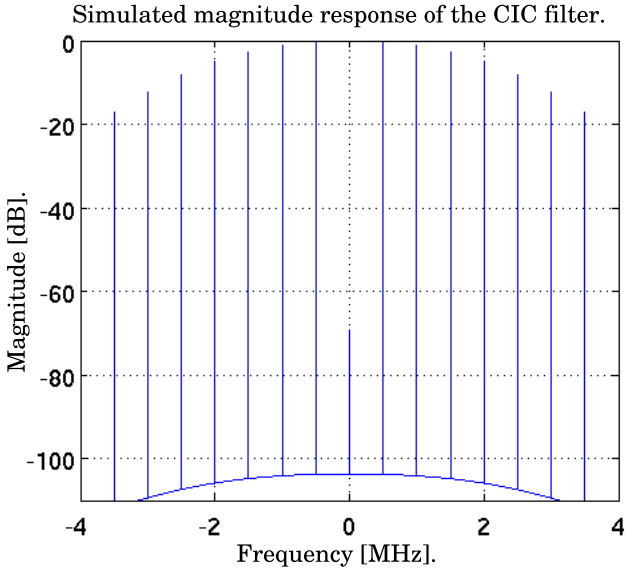

Figure 4.16: The simulated magnitude response of a 6-section CIC filter.

The simulation output is very similar when compared to Figure 4.15, with a passband rolloff of approximately 5 dB at 2 MHz. Figure 4.17 shows the real channel output for the out-of-band attenuation simulation.

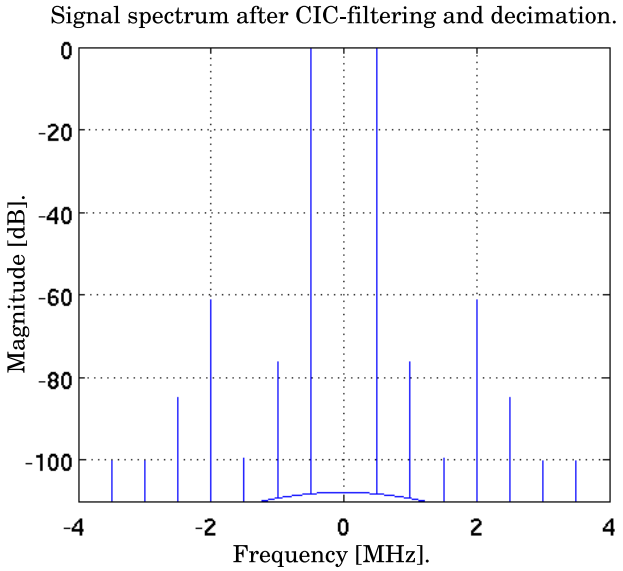

Figure 4.17: The output signal spectrum of the out-of-band attenuation simulation for the 6-section CIC filter.

It can be seen that the original input tone at 6 MHz is attenuated by approximately 60 dB before aliasing down to 2 MHz. This is consistent with the magnitude response

shown by Figure 4.15. The input tone at 9.5 MHz is attenuated by about 100 dB, before aliasing down to 1.5 MHz. Figure 4.15 shows that any unwanted signals will be attenuated by at least 75 dB before aliasing down to the region between 0 and 1.5 MHz.

4.2.2 FIR Filter

The final filter in the USRP receive chain should have an out-of-band attenuation of more than 70 dB and decimate the input signal by a final factor of two. The first step in designing this filter was to determine the amount of LEs available on the FPGA after removing all the unnecessary functionality, extending the CIC filters and removing the halfband filters. Figure 4.18 shows the Quartus report after synthesising the FPGA Verilog build.

Fitter Status	Successful - Thu Nov 26 19:57:48 2009
Quartus II Version	8.0 Build 231 07/10/2008 SP 1 SJ Web Edition
Revision Name	usrp_std
Top-level Entity Name	usrp_std
Family	Cyclone
Device	EP1C12Q240C8
Timing Models	Final
Total logic elements	7,020 / 12,060 (58 %)
Total pins	173 / 173 (100 %)
Total virtual pins	0
Total memory bits	73,728 / 239,616 (31 %)
Total PLLs	0 / 2 (0 %)

Figure 4.18: The Quartus report after synthesising the FPGA build, showing the LE usage.

The output shows that there are 5040 LEs available for the final filtering stage. Four identical filters are required, resulting in a maximum of 1260 LEs per filter. It was found that a 16-bit multiplier occupies 337 LEs when synthesised. Each of the four filters can therefore use two multipliers. The remaining LEs are needed to implement the delay lines and accumulators required by a digital filter.

Polyphase Decomposition

Polyphase decomposition is a method used for, amongst other things, the efficient real-time implementation of decimation filters [8]. The transfer function of a digital FIR

filter is given by

$$H(z) = \sum_{n=-\infty}^{\infty} h(n)z^{-n} \tag{4.13}$$

Using polyphase decomposition, Equation 4.13 can be rewritten as

$$H(z) = E_0(z^2) + z^{-1}E_1(z^2) \tag{4.14}$$

The impulse response coefficients of the original filter are now grouped into even-numbered samples, $e_0(n) = h(2n)$, and odd-numbered samples, $e_1(n) = h(2n+1)$. Another method used in the implementation of decimation and interpolation filters are the so-called *noble identities*. The noble identity for decimation implies that a filter, followed by a decimator, is equivalent to a decimator, followed by a filter running at the slower rate, provided that the transfer function of the filter is rational [8]. The original operation of lowpass-filtering and decimation is shown in Figure 4.19.

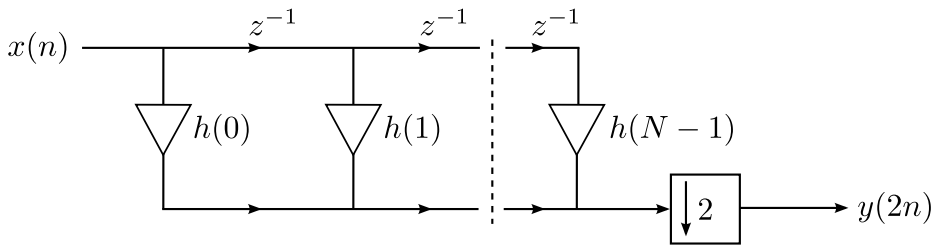

Figure 4.19: A FIR lowpass-filter, followed by a decimator [8].

Figure 4.20 shows the structure obtained after using polyphase decomposition to split the original filter into two sub-filters, along with the noble identity to move the decimator to the front of the filter.

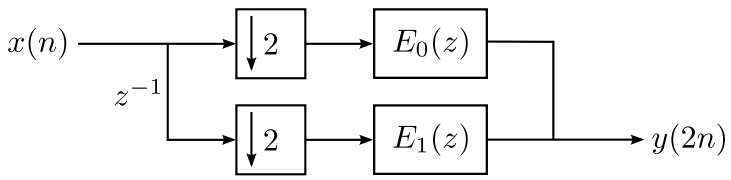

Figure 4.20: The FIR lowpass-filter in polyphase form, preceded by a decimator [8].

The advantage of this structure is that the original filter now runs at half the clock rate. The length of the filter can therefore be doubled, allowing the design of filters with a better out-of-band attenuation and a narrower transition band. The Matlab Filter Design and Analysis Tool was used to design the final filter. The parameters of the filter are given in Table 4.1.

Table 4.1: Polyphase FIR filter parameters.

Design method	Equiripple
Density factor	20
Sampling frequency	8 MHz
Passband edge frequency	1.3 MHz
Stopband edge frequency	2 MHz
Passband attenuation	1 dB
Stopband attenuation	75 dB
Filter order	28

Using two multipliers allows a 32-coefficient filter to be designed. Two clock cycles were reserved for synchronisation purposes, resulting in a slightly smaller design. The magnitude response of the filter is shown in Figure 4.21.

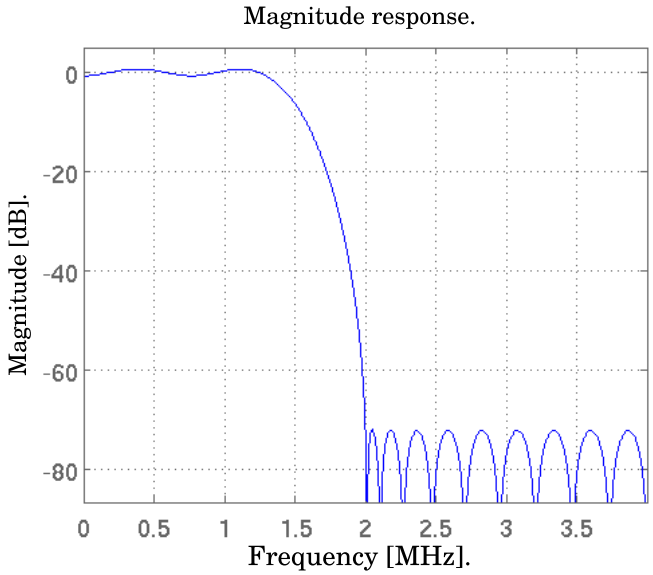

Figure 4.21: The magnitude response of the polyphase FIR filter.

FIR Filter Simulations

After implementing the polyphase FIR filter on the FPGA, Icarus Verilog was used to compare the passband magnitude response and the out-of-band attenuation to the response obtained with the Matlab Filter Visualisation Tool. The real channel output for the passband magnitude response simulation is shown in Figure 4.22.

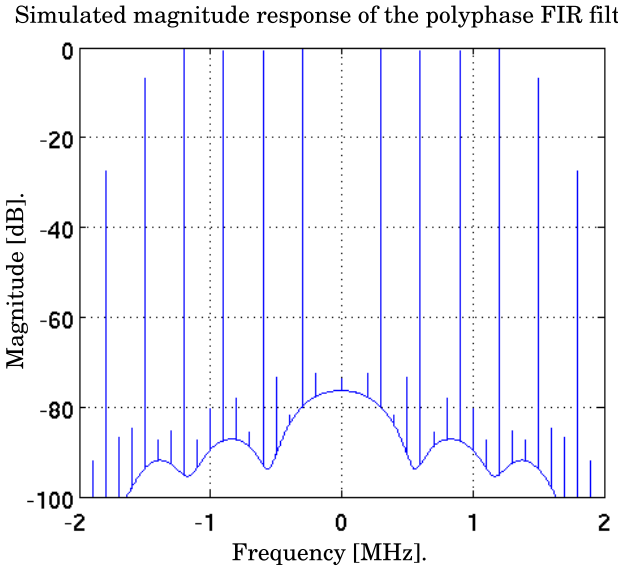

Figure 4.22: The simulated magnitude response of the polyphase FIR filter.

The passband magnitude response compares well to the response obtained in Matlab, with an attenuation of approximately 28 dB at 1.8 MHz. To determine the out-of-band attenuation of the filter, the simulation that was performed for the halfband filter was repeated for the polyphase FIR filter. The real channel output for the simulation is shown in Figure 4.23.

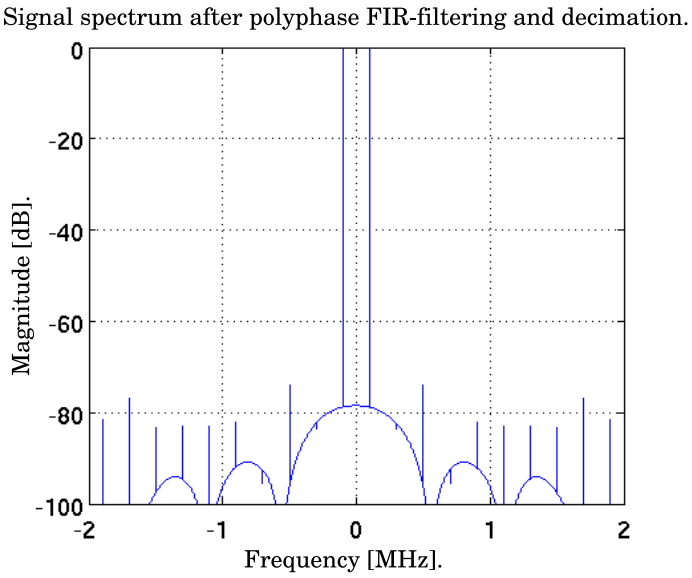

Figure 4.23: The output signal spectrum of the out-of-band attenuation simulation for the polyphase FIR filter.

Figure 4.23 shows that the signal tones at 2.1 MHz, 2.3 MHz and 2.5 MHz are attenuated by at least 75 dB before aliasing back to the final band of interest. The final

simulations indicate that the designed filter was correctly implemented on the FPGA. The Quartus report after synthesising the final design is shown in Figure 4.24.

Fitter Status	Successful - Thu Aug 13 19:50:39 2009
Quartus II Version	8.0 Build 231 07/10/2008 SP 1 SJ Web Edition
Revision Name	usrp_std
Top-level Entity Name	usrp_std
Family	Cyclone
Device	EP1C12Q240C8
Timing Models	Final
Total logic elements	11,024 / 12,060 (91 %)
Total pins	173 / 173 (100 %)
Total virtual pins	0
Total memory bits	73,728 / 239,616 (31 %)
Total PLLs	0 / 2 (0 %)

Figure 4.24: The Quartus report after synthesising the final FPGA build.

It can be seen that only 1036 LEs remain after synthesising the final design. Dividing them between four channels would not enable any further significant improvements to be made.

4.3 Chapter Summary

This chapter presented an analysis of the signal processing stages of the receive path of the USRP FPGA. The Icarus Verilog simulation tool was used to compare the theoretical performance of each stage to the actual performance. The following observations regarding the standard FPGA build were made

- The phase accumulator and CORDIC algorithm perform sufficiently to take advantage of the full A/D converter dynamic range and do not need to be improved.
- The number of sections in each CIC filter can be increased to achieve a better attenuation of out-of-band signals. This comes at the expense of an increase in passband rolloff.
- The final halfband filters cause signals to alias back to a portion of the band of interest at high levels. The final filter in each channel should be improved to minimise the aliasing levels. The stopband attenuation of the final filter should also be above 70 dB.

The required improvements were made to each receive channel. It was found that

- Increasing the CIC filters by two stages resulted in a passband rolloff increase of approximately 2 dB over the band of interest, while the attenuation of out-of-band signals increased by approximately 20 dB.
- A final usable bandwidth of 2.6 MHz could be achieved, with a stopband attenuation of 75 dB at 2 MHz.
- The improvements to the receive chain are marginal. The FPGA on the USRP has a very limited number of LEs, allowing only basic filters to be implemented. A larger FPGA would have allowed filters with a narrower transition band to be implemented, resulting in a wider usable bandwidth.

Chapter 5

PCL Radar Signal Processing

The anatomy of a PCL radar system was presented in Chapter 2. In particular, the signal processing stages are

- DPI and clutter suppression
- Matched filter processing
- Target detection
- Target association
- Target state estimation

This chapter presents an analysis of the first two sections. The matched filter lies at the core of the PCL radar signal processing, and is also required to evaluate the performance of any DPI and clutter suppression algorithms, and will therefore be discussed first. For the DPI and clutter suppression section, three different algorithms are briefly presented and implemented. A FERS simulation is used to compare the convergence time and amount of suppression of each of the algorithms. This chapter concludes with a discussion of the results. A suitable DPI suppression algorithm to be used in the experimental PCL radar system is also chosen.

5.1 Matched Filter Processing

The matched filter was introduced in Chapter 2. Using discrete time notation, it can be written as

$$\left|\Psi(\tau,\nu)^2\right| = \left|\sum_{n=0}^{N-1} s(n)d^*(n-\tau)\mathbf{exp}(j2\pi\nu n/N)\right|^2 \tag{5.1}$$

where τ denotes the time-delay of interest and ν denotes the Doppler-shift of interest. The ARD surface, $|\Psi(\tau,\nu)^2|$, can be calculated as follows

- Rotate $d(n)$ and conjugate to obtain $d^*(n-\tau)$.
- Calculate the dot-product of $d^*(n-\tau)$ and $s(n)$.
- Calculate the fast Fourier transform (FFT) of the above dot-product.
- Discard the FFT bins that are not of interest.
- Repeat the above steps for the next range of interest [11].

The reference signal can also be weighted using a windowing function to reduce the range and Doppler sidelobes [41]. This causes a small loss in processing gain and a slight broadening of the main peak of the ARD surface [11]. The ARD surface contains Doppler and bistatic delay (or range) information, indicating the presence of reflections of the reference signal. A reflection from a moving target will have an associated bistatic range and Doppler frequency, while reflections from stationary clutter are confined to the zero-Doppler bins. The matched filter serves an additional purpose in a PCL radar system. Reflections from moving targets are very weak and are often beneath the noise floor of the receiver. For a reasonable false alarm rate, an SNR of at least 10 dB is needed [42]. The matched filter provides integration gain, causing the noise floor to lower, thereby increasing the SNR. The integration gain can be calculated as follows [21]

$$G_P = T_{MAX} B \tag{5.2}$$

where T_{MAX} is the total coherent integration time and B is the signal bandwidth. For a typical PCL radar utilising FM transmitters, $T_{MAX} = 1$ s and $B = 50$ kHz, resulting in a theoretical processing gain of 47 dB. The target dynamics place a limit on the maximum integration time. A rule of thumb for this limit is

$$T_{MAX} = \left(\frac{\lambda}{A_R}\right)^{1/2} \tag{5.3}$$

where A_R is the radial component of the target acceleration. Kulpa [43] investigated long integration time PCL radar by incorporating range-mitigation effects into the processing.

5.1.1 Matched Filter Implementation

For initial testing purposes, a matched filter was implemented in Matlab. A Hanning window was used to weigh the reference signal before the matched filter processing. After verifying that the matched filter functioned correctly, a second version was implemented in the C++ programming language. To test the matched filter, a FERS simulation was performed. A 1-second portion of an audio signal was first FM modulated and then upsampled to a sampling frequency of 500 kHz using a GNURadio script. The spectrum of the resulting signal is shown in Figure 5.1, while Figure 5.2 shows the self-ambiguity function of the signal.

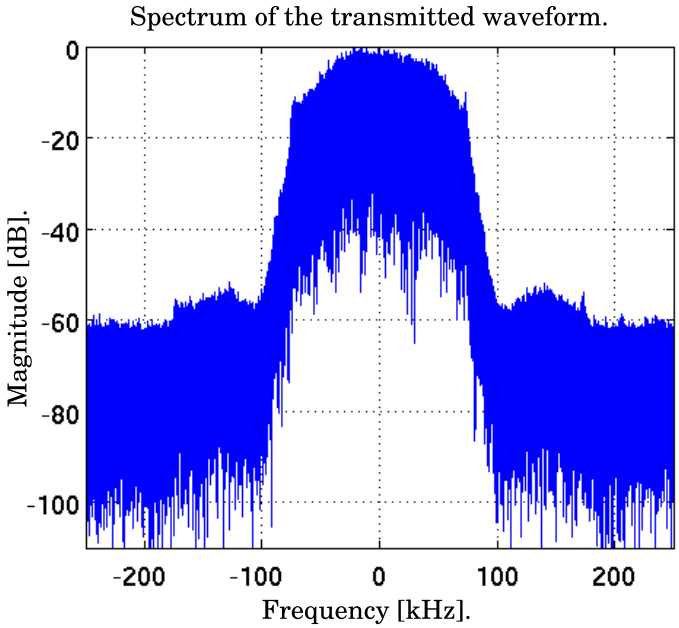

Figure 5.1: Spectrum of the transmitted waveform.

Figures 5.1 and 5.2 show the correct spectrum and self-ambiguity function of an FM signal, indicating that the signal was correctly generated. A FERS script file was written to reflect the geometry shown in Figure 5.3.

The carrier frequency of the transmitted waveform is 88.2 MHz, while the the target has an RCS of 20 m^2. The theoretical signal-to-interference ratio (SIR) plot for the simulated geometry is shown in Figure 5.4.

For the given geometry, the reflected signal from the target should be between 80 and 85 dB below the direct signal. For testing purposes, the system was first simulated without the target to obtain a clean reference signal. The simulation was then repeated, this time including the target. The clean reference signal was then subtracted

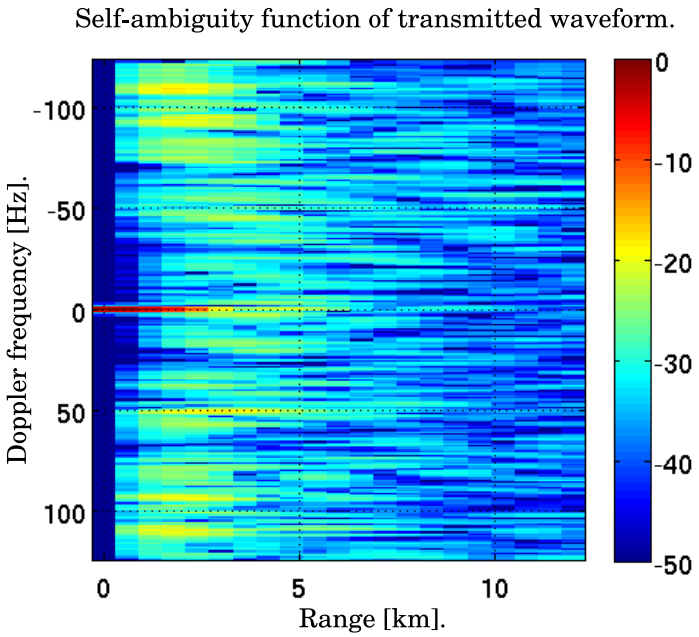

Figure 5.2: Self-ambiguity function of the transmitted waveform.

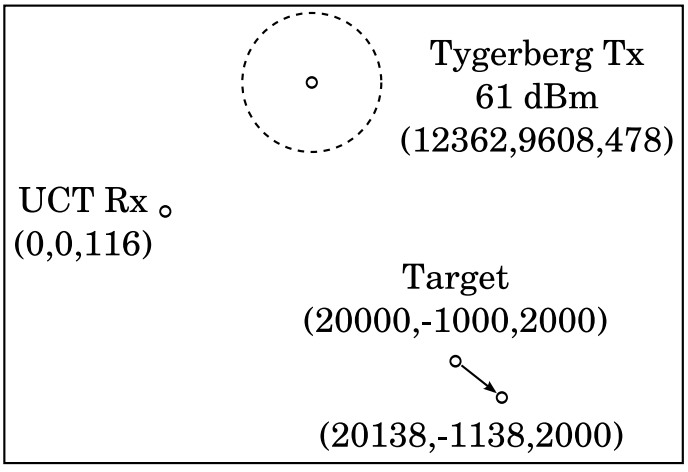

Figure 5.3: Geometry of the FERS simulation. All the coordinates are in metres. The two target positions are at $t = 0$ s and $t = 1$ s. The Tygerberg transmitter is modelled as having an omnidirectional antenna.

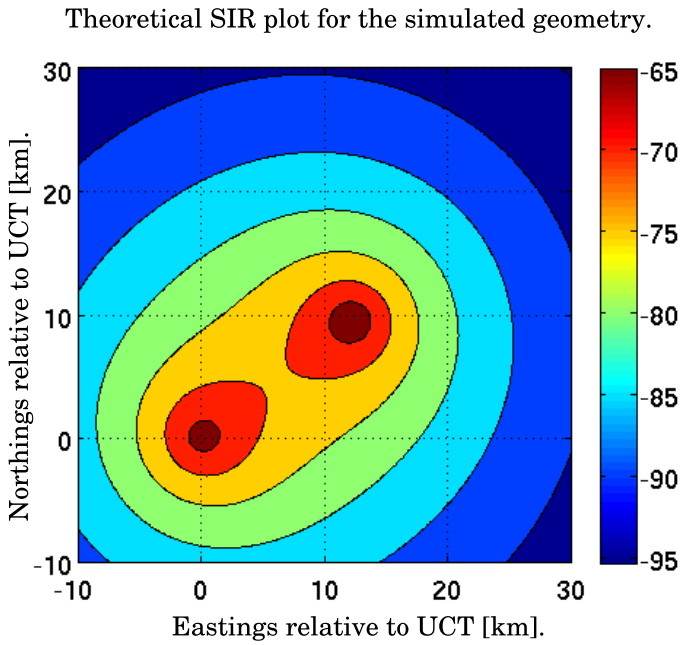

Figure 5.4: Theoretical SIR for the simulated geometry.

from the surveillance signal, leaving only the target reflection in the surveillance channel. The spectra of the received reference and and target reflection signals are shown in Figures 5.5 and 5.6 respectively. The magnitude of the reflected signal is normalised relative to the magnitude of the direct signal.

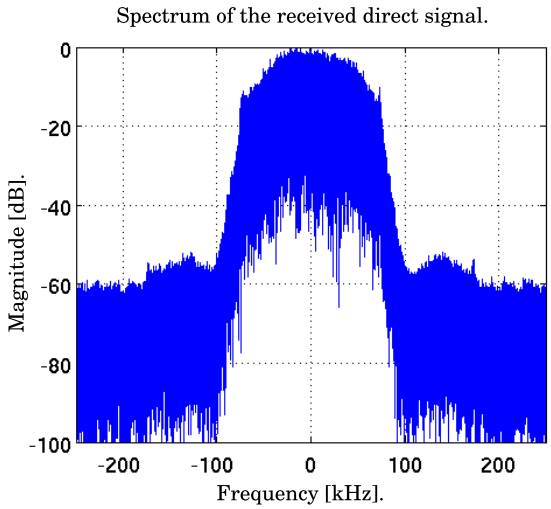

Figure 5.5: Spectrum of the received direct signal.

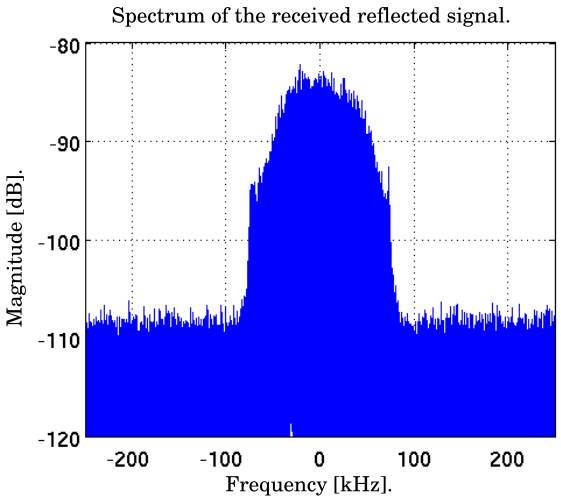

Figure 5.6: Spectrum of the received reflected signal.

It can be seen that the SIR is approximately -83 dB, which compares well to Figure 5.4. In a real-world PCL radar system, sufficient DPI suppression would need to be employed to make the reflected signal detectable on the ARD surface. The ARD surface

produced by the matched filter processing is shown in Figure 5.7, while Figure 5.8 shows the target reflection in more detail.

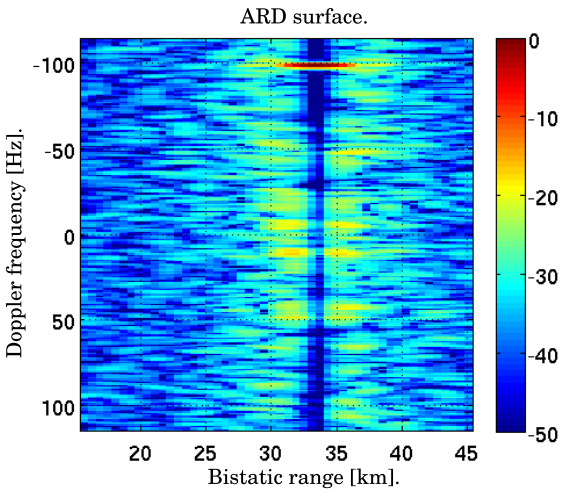

Figure 5.7: The ARD surface produced by the matched filter.

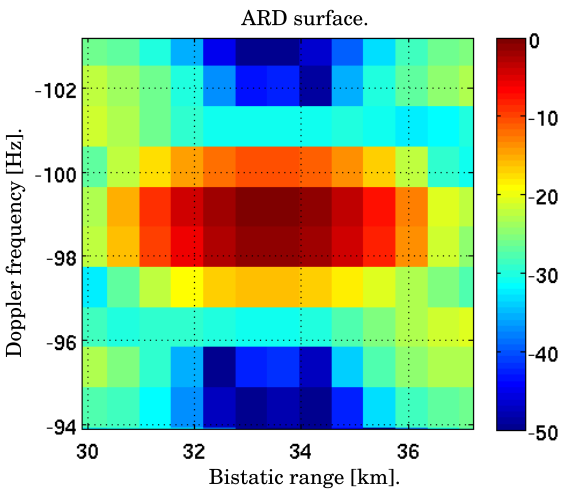

Figure 5.8: The ARD surface, showing the area around the target reflection in more detail.

The ARD surface indicates that the target has a bistatic range of approximately 34 km and a Doppler frequency of -99 Hz. This was verified against the theoretical values by using Equations 2.4 and 2.5.

5.1.2 Accelerating the Matched Filter

The computational cost of the matched filter can be reduced by observing that target reflections can only be present within a limited range of Doppler frequencies. For a monostatic geometry, the Doppler shift is given by

$$f_d = \frac{2v}{\lambda} \tag{5.4}$$

For FM radio signals, $\lambda = 3$ m, and anticipating targets with a maximum velocity of 250 m.s^{-1} (900 km.h^{-1}), yields a maximum Doppler frequency of 167 Hz. A more efficient approach to implementing the matched filter would therefore be to downsample the data after calculation of the dot-product in order to perform a smaller FFT [11]. This sample rate reduction can be achieved by using a CIC filter to decimate from a sampling frequency of 500 kHz to a sampling frequency of 2 kHz, followed by a short FIR filter to attenuate out-of-band frequencies. Using only a FIR filter for the decimation process would not be possible, since the filter would be several thousand coefficients long. The magnitude response of a single section CIC filter when decimating

from a sampling frequency of 500 kHz to a sampling frequency of 2 kHz is shown in Figure 5.9.

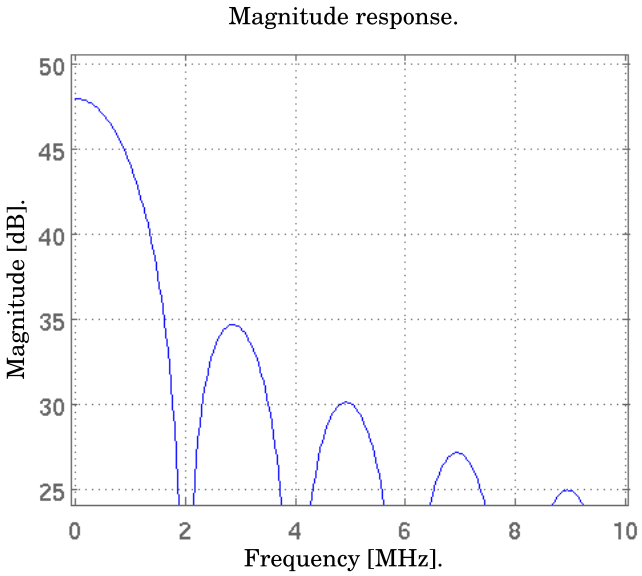

Figure 5.9: The magnitude response of a 1-section CIC filter with $R = 250$ and $M = 1$.

The out-of-band attenuation of this filter is sufficient, since the strongest components on the ARD surface are the direct signal, clutter reflections and reflections from moving targets. These components are all found at frequencies below 1 kHz. The CIC filter also has a passband rolloff of less than 0.2 dB from 0 to 200 Hz, which is negligible. For testing purposes, a FIR filter with the parameters shown in Table 5.1 was designed.

Table 5.1: Parameters of the FIR filter.

Design Method	Equiripple
Density Factor	20
Sampling Frequency	2 kHz
Passband Edge Frequency	200 Hz
Stopband Edge Frequency	800 Hz
Passband Attenuation	1 dB
Stopband Attenuation	65 dB
Filter Order	5

The magnitude response of the filter is shown in Figure 5.10.

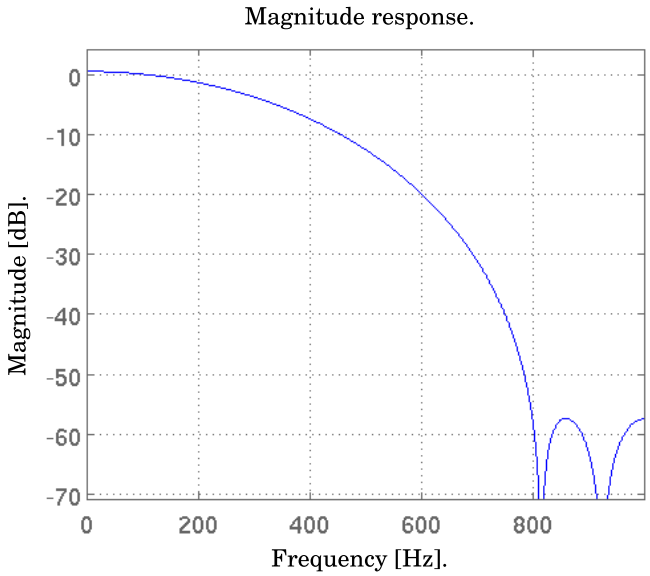

Figure 5.10: Magnitude response of the FIR filter.

The modified matched filter can now be calculated as follows

- Rotate $d(n)$ and conjugate to obtain $d^*(n-\tau)$.
- Calculate the dot-product of $d^*(n-\tau)$ and $s(n)$.
- Perform a high-rate decimation using a CIC filter.
- Lowpass-filter the downsampled data using a short FIR filter.
- Calculate the FFT of the downsampled data.
- Repeat the above for the next range of interest.

The modified matched filter was implemented and used to process the reference and surveillance channel signals of the previous simulation. The resulting ARD surface is shown in Figure 5.11.

Comparing Figure 5.11 to Figure 5.7 shows that the same result can be obtained by using a smaller FFT in the matched filter, provided that the data is first lowpass-filtered and decimated. It should be noted that the Doppler frequencies where target reflections can be expected is dependent on the carrier frequency of the utilised transmitter. Equation 5.6 shows that the maximum target Doppler frequency increases with an increase in transmitter frequency.

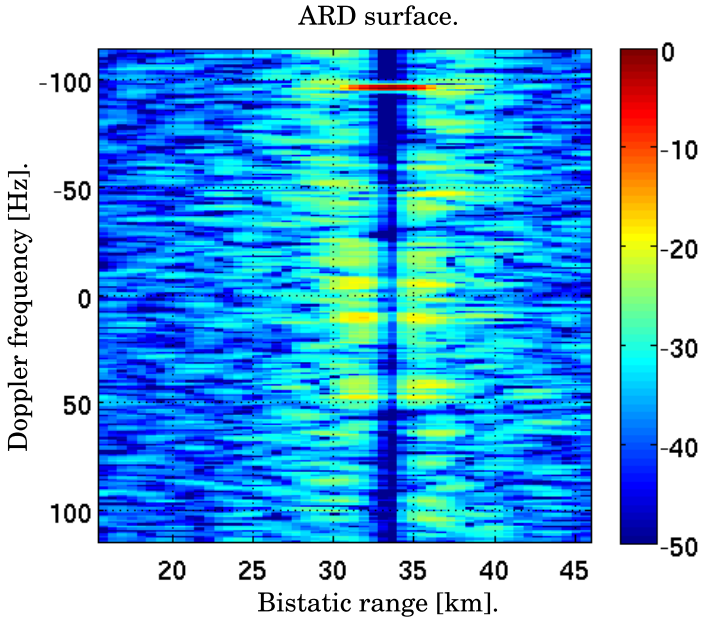

Figure 5.11: The ARD surface produced by the accelerated matched filter.

5.1.3 Computational Cost of the Matched Filter

Howland [11] presents an analysis of the computational cost involved in performing the matched filter processing of the reference and surveillance channel signals in terms of complex operations. To calculate the FFT for a certain range of interest involves $N \log_2 N$ complex operations, where $N = 2^{19}$ (524288) for the original matched filter. The number of complex operations therefore equals 9 961 472. The computational cost after adding the CIC and FIR filters involves

- N complex additions for the one stage integrator and $N_d = \frac{N}{R}$ complex additions for the one stage comb, where $N = 500\,000$ and $R = 250$.
- $5N_d$ complex multiplications and $5N_d$ complex additions for the lowpass filter, where $N_d = 2000$.
- $N_d \log_2(N_d)$ complex operations for the FFT, where N_d is the same as above.

The new computational cost is calculated to be 544 528 complex operations. The theoretical computational speed increase due to the decimation before the FFT is therefore approximately 18 times. To test this speedup, a C++ application was written to implement both versions of the matched filter. The *ctime* library was used to determine the total time needed to calculate the ARD surface for a maximum bistatic range of 30 km. This requires 50 FFTs to be performed when the sampling frequency equals 500 kHz. Ten iterations were used to obtain an average value. It was found that the

first matched filter takes 5.7 seconds to be processed on average, while the decimated version takes 1.4 seconds. The speedup factor is therefore four times. This can be attributed to the fact that the C++ code was written sequentially, with the filtering of the real and imaginary signal paths performed separately. Using threads to process the two paths in parallel, as well as processing the CIC and FIR filters in parallel, would bring the total speed increase closer to the theoretical value.

5.2 Direct Signal and Clutter Suppression

A typical interference suppression scheme is shown in Figure 5.12.

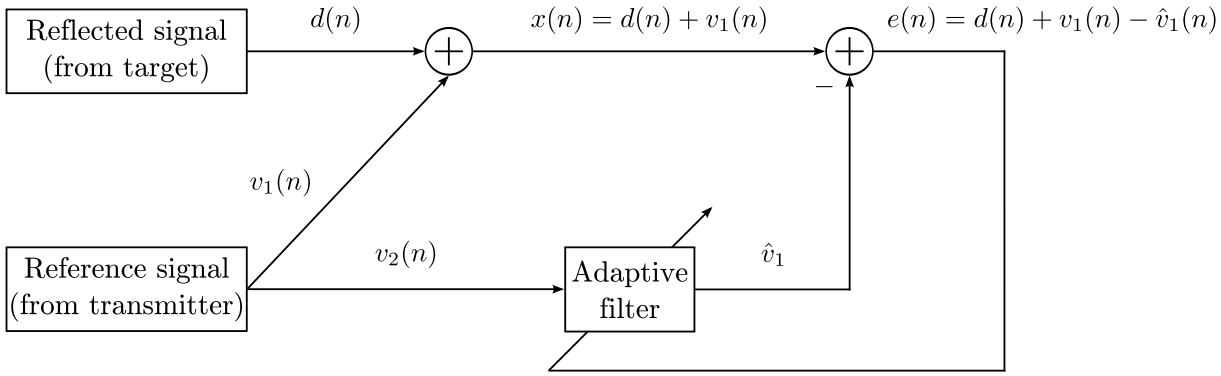

Figure 5.12: Interference suppression using an adaptive filter [9].

The desired signal, $d(n)$, is received by the primary sensor, along with an interference signal, $v_1(n)$. A secondary sensor is used to obtain a clean copy of the interference signal, $v_2(n)$. An adaptive filter is then used to provide an estimate of the interference component received by the primary sensor, $\hat{v}_1(n)$, by observing $v_2(n)$. This estimate is subtracted from the signal received by the primary sensor to obtain an estimate of the desired signal, $e(n)$. This resulting signal is now used to update the taps of the adaptive filter.

In a PCL radar system, the desired signal contains reflections from moving targets, while the interference is made up of the strong DPI from the transmitter, as well as clutter components. A number of different adaptive filters can be used for DPI suppression. Malanowski [44] provides a comparison of the convergence performance of a number of these filters when applied to PCL radar. For this dissertation, the *normalised least-mean square* (NLMS), *recursive least-squares* (RLS) and *signal projection* algorithms were implemented and tested. For the sake of clarity, each of these algorithms will be briefly introduced. For a more complete description, see Haykin [45].

5.2.1 The Normalised Least-Mean Square Algorithm

The NLMS algorithm is a variant of the popular least-mean square (LMS) algorithm, developed by Widrow and Hoff in 1960 [45]. The LMS algorithm consists of two processes:

1. Filtering, which involves (a) computing the output of a transversal filter by multiplying a set of inputs by a set of filter taps and (b) generating an estimation error by comparing the filter output to a desired response.

2. An adaptive process which uses the estimation error to update the set of filter taps.

The tap update equation of the LMS filter for complex signals is given by

$$\mathbf{w}(n+1) = \mathbf{w}(n) + 2\mu e^*(n)\mathbf{x}(n) \tag{5.5}$$

where $\mathbf{w}(n)$ is the set of filter taps at time n, μ is the adaptation constant, $e^*(n)$ is the complex conjugate of the error and $\mathbf{x}(n)$ is the input data. When the input data is large, the LMS algorithm experiences a so-called *gradient noise amplification* problem. The NLMS algorithm alleviates this problem by normalising the coefficient update equation with respect to the squared-norm of the input data [45].

Algorithm 5.1 The NLMS algorithm [45].

Parameters: M = number of taps
$\tilde{\mu}$ = adaptation constant
$0 < \tilde{\mu} < 2$
a = positive constant

Initialisation. If prior knowledge on the tap-weight vector, $\hat{\mathbf{w}}(n)$, is available, use it to select an appropriate value for $\hat{\mathbf{w}}(0)$. Otherwise, set $\hat{\mathbf{w}}(0) = 0$.

Data

(a) Given: $\mathbf{u}(n)$: M-by-1 tap input vector at time n
$d(n)$: desired response at time n

(b) To be computed: $\hat{\mathbf{w}}(n+1)$ = estimate of tap-weight vector at time $n+1$

Computation: $n = 0, 1, 2, ...$

$e(n) = d(n) - \hat{\mathbf{w}}^H(n)\mathbf{u}(n)$
$\hat{\mathbf{w}}(n) = \hat{\mathbf{w}}(n) + \frac{\tilde{\mu}}{a+\|\mathbf{u}(n)\|^2}\mathbf{u}(n)e^*(n)$

5.2.2 The Recursive Least-Squares Algorithm

The RLS algorithm aims at minimising the following cost function

$$J(n) = \sum_{k=1}^{n} \lambda^{n-k} e^2(k) \tag{5.6}$$

where $e^2(k)$ is the square of the error and λ is an exponential weighting factor, also known as the *forgetting factor*. A value between 0.98 and 1 is usually used for λ. The RLS algorithm utilises information extending to the time that the filter was initialised, resulting in an adaptive algorithm with tracking capabilities [9].

Algorithm 5.2 The RLS algorithm [45].

Initialise the algorithm by setting

$\mathbf{P}(0) = \delta^{-1}\mathbf{I}$ $\quad$ δ = small positive constant

$\hat{\mathbf{w}}(0) = 0$

For each instant of time, $n = 1, 2, ...$, compute

$$\mathbf{k}(n) = \frac{\lambda^{-1}\mathbf{P}(n-1)\mathbf{u}(n)}{1+\lambda^{-1}\mathbf{u}^H(n)\mathbf{P}(n-1)\mathbf{u}(n)}$$

$$\xi(n) = d(n) - \hat{\mathbf{w}}^H(n-1)\mathbf{u}(n)$$

$$\hat{\mathbf{w}}(n) = \hat{\mathbf{w}}(n-1) + \mathbf{k}(n)\xi^*(n)$$

$$\mathbf{P}(n) = \lambda^{-1}\mathbf{P}(n-1) - \lambda^{-1}\mathbf{k}(n)\mathbf{u}^H(n)\mathbf{P}(n-1)$$

5.2.3 Signal Projection

Signal projection can be used to project the surveillance signal into the subspace orthogonal to the reference signal [46]. The surveillance signal after projection becomes

$$\mathbf{v} = [\mathbf{I} - \mathbf{A}(\mathbf{A}^T\mathbf{A})^{-1}\mathbf{A}^T].\mathbf{s} \tag{5.7}$$

where $\mathbf{I}$ is an identity matrix, $\mathbf{A}$ contains samples of the reference signal and $\mathbf{s}$ is the original surveillance signal. The size and entries of $\mathbf{A}$ are determined by the number of range bins that the DPI and clutter span on the ARD surface. The complete description of the algorithm is quite lengthy and will not be repeated here. For a more detailed description, the reader is referred to Colone [47].

5.2.4 Adaptive Filter Performance Comparison

A FERS simulation was used to compare the convergence performance of the different DPI suppression algorithms. The simulation setup is shown in Figure 5.13.

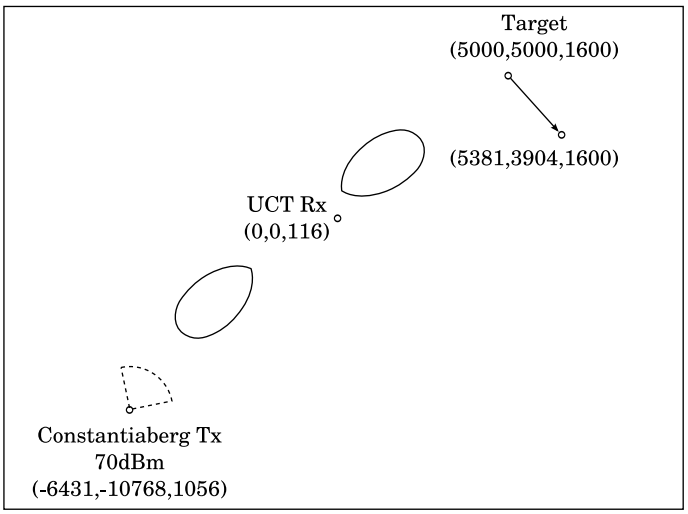

Figure 5.13: Geometry of the FERS simulation. The two target positions are at $t = 0$ s and $t = 10$ s.

This time a single simulation was performed, with two Yagi antennas to receive the reference signal from the transmitter and the reflected signal from the target respectively. The RCS of the target is 20 m^2, yielding a theoretical SIR of -80 dB. The Yagi antenna pointing in the direction of the target has a front-to-back ratio of approximately 10 dB and therefore, the target reflection still remains about 70 dB below the DPI component. An adaptive filter would need to suppress this DPI component to make the target detectable on the ARD surface.

The Normalised Least-Mean Square Algorithm

The NLMS algorithm was used to suppress the DPI in the surveillance channel. For the simulation, a 16-tap adaptive filter was used, enabling DPI suppression up to a range of 9.6 km on the ARD surface. Figure 5.14 shows the surveillance signal after suppressing the DPI using different adaptation constants.

It can be seen that the NLMS algorithm only converges after approximately 500 000 samples, corresponding to 1-second of output data. The target will therefore only be detected after processing the second 1-second block of data. The NLMS algorithm converges faster for larger adaptation constants, but this comes at the expense of a larger mean-squared error after adaptation [45]. The four plots also show that the NLMS algorithm provides approximately 20 dB of DPI suppression. The ARD surface that was obtained after DPI suppression using the NLMS algorithm with an adaptation constant of 1.5, and processing the first 1-second block of data is shown in Figure 5.15.

Convergence performance of the NLMS filter for different adaptation constants.

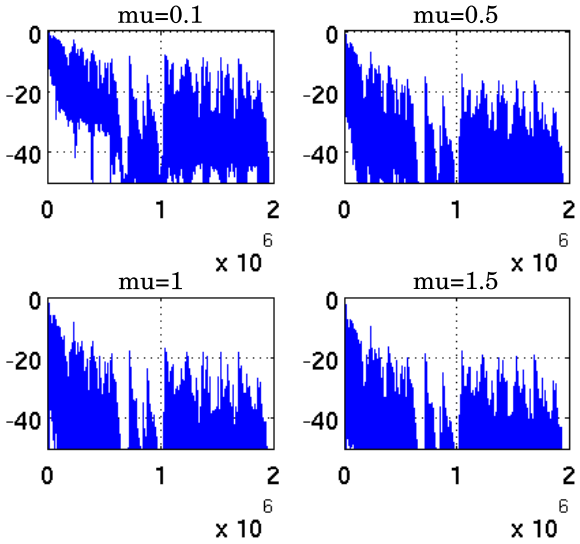

Figure 5.14: Convergence performance of the NLMS algorithm for different adaptation constants. The y-axis represents the magnitude of the complex signal in dB, while the x-axis represents samples. Each plot shows four seconds of data.

ARD surface.

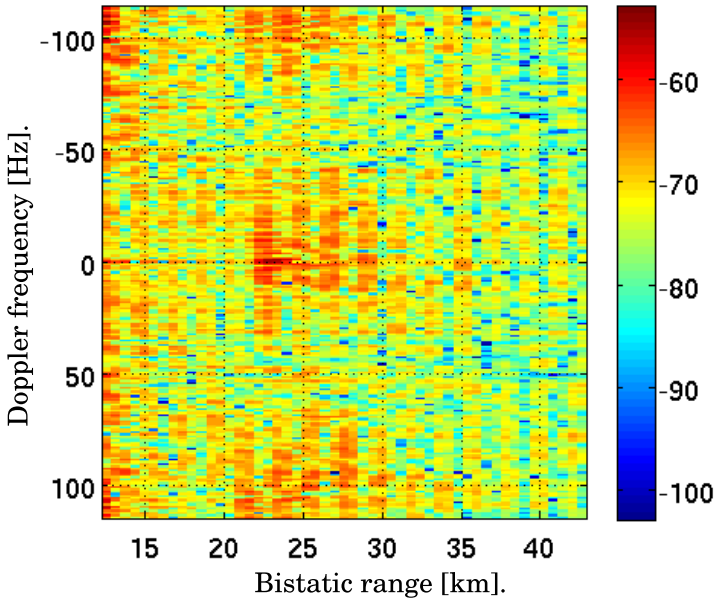

Figure 5.15: The ARD surface obtained after using the NLMS algorithm to suppress the direct signal and processing the first 1-second block of data. The filter has not yet converged and the target reflection is still hidden by the DPI component.

As expected, the target is still hidden by the sidelobes of the DPI in the surveillance channel. The ARD surface obtained after processing the second 1-second block of data is shown in Figure 5.16.

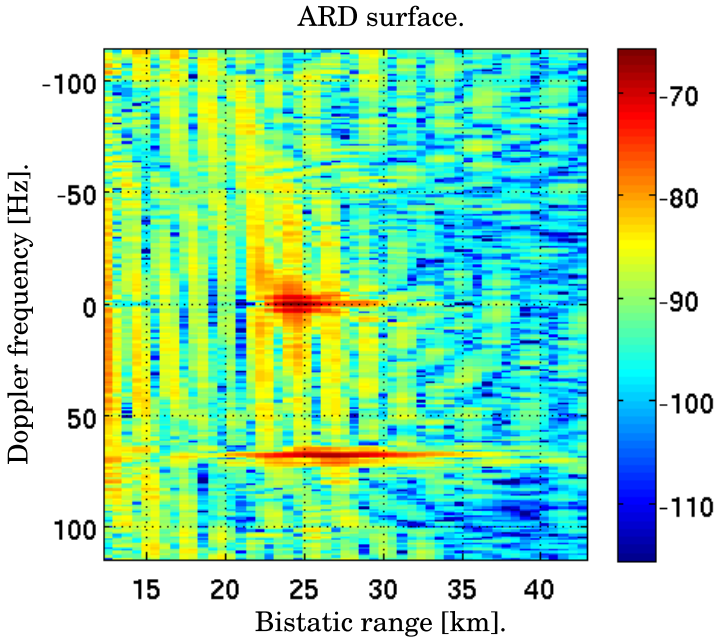

Figure 5.16: The ARD surface obtained after using the NLMS algorithm to suppress the direct signal and processing the second 1-second block of data. The filter has converged, causing the target to be detected.

The target can now clearly be seen. Due to the slow convergence rate, the NLMS algorithm is not suitable for PCL radar systems where 1-second blocks of data need to be processed at a time. Howland used the *joint process estimator* algorithm to improve the convergence rate of the NLMS algorithm [11].

The Recursive Least-Squares Algorithm

The RLS algorithm was also used to suppress the DPI in the surveillance channel. The surveillance signal, after suppressing the DPI with a 16-tap RLS filter with a forgetting factor of 0.99 is shown in Figure 5.17.

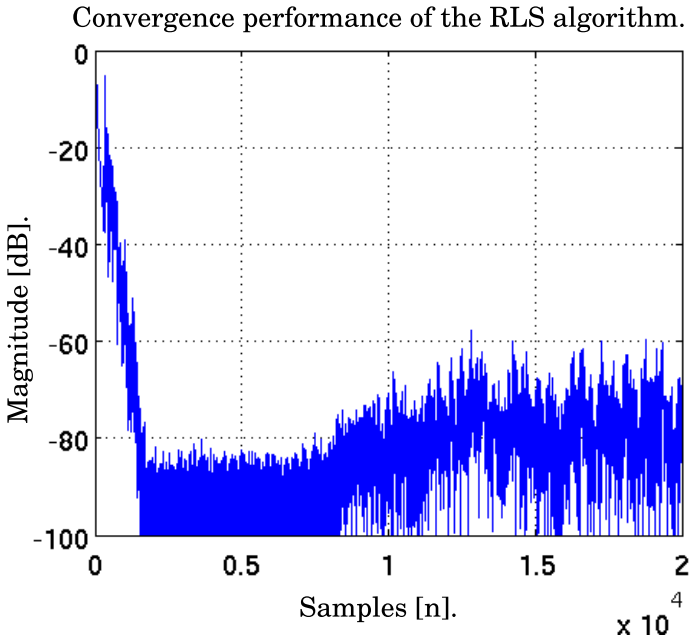

Figure 5.17: Convergence performance of the RLS filter for a forgetting factor of 0.99.

The convergence of the RLS algorithm is very rapid when compared to that of the NLMS algorithm. In this case, convergence takes only about 10 000 iterations of the algorithm. It can also be seen that the RLS algorithm provides approximately 60 dB of DPI suppression. The ARD surface obtained after suppressing the DPI in the surveillance channel and processing the first 1-second block of data is shown in Figure 5.18.

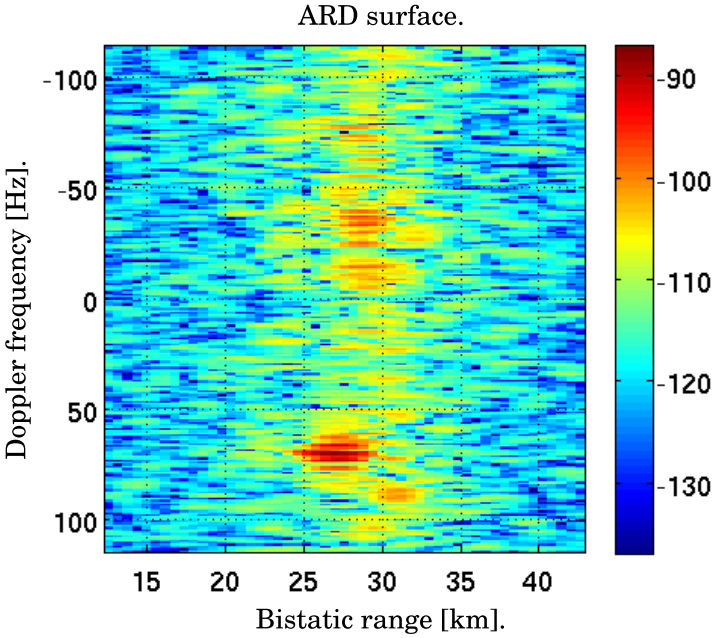

Figure 5.18: The ARD surface obtained after using the RLS algorithm to suppress the direct signal and processing the first 1-second block of data. The target is clearly visible.

The target is clearly visible on the ARD surface. The RLS algorithm converges much faster than the NLMS algorithm, but this comes at the expense of a higher computational cost [45].

Signal Projection

The signal projection algorithm was used to suppress the DPI in the first 16 range bins of the ARD surface. The surveillance signal, after DPI suppression, is shown in Figure 5.19.

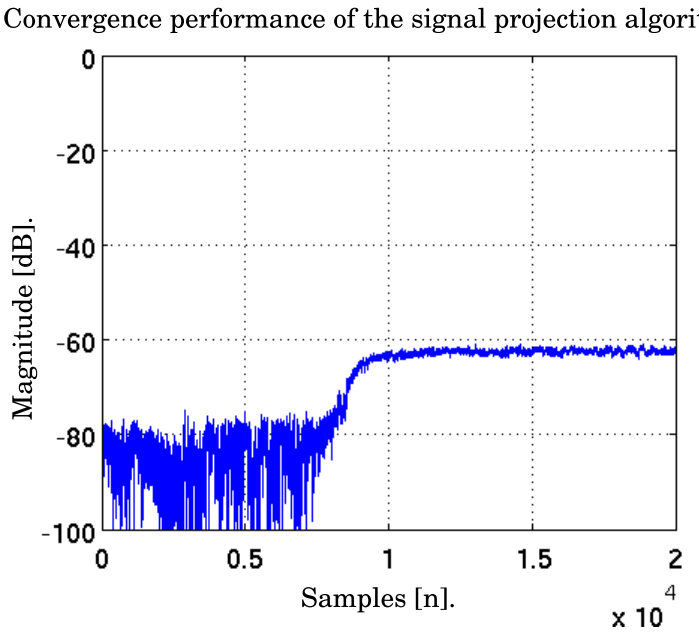

Figure 5.19: Convergence performance of the signal projection algorithm.

The time needed for the signal projection algorithm to converge is comparable to that of the RLS algorithm. The signal projection algorithm also provides approximately 60 dB of DPI suppression. The ARD surface obtained after DPI suppression with the signal projection algorithm and processing the first 1-second block of data is shown in Figure 5.20.

The target is clearly visible on the ARD surface. The computational cost of the signal projection algorithm is also higher than that of the NLMS algorithm, since the algorithm needs to invert a relatively large matrix.

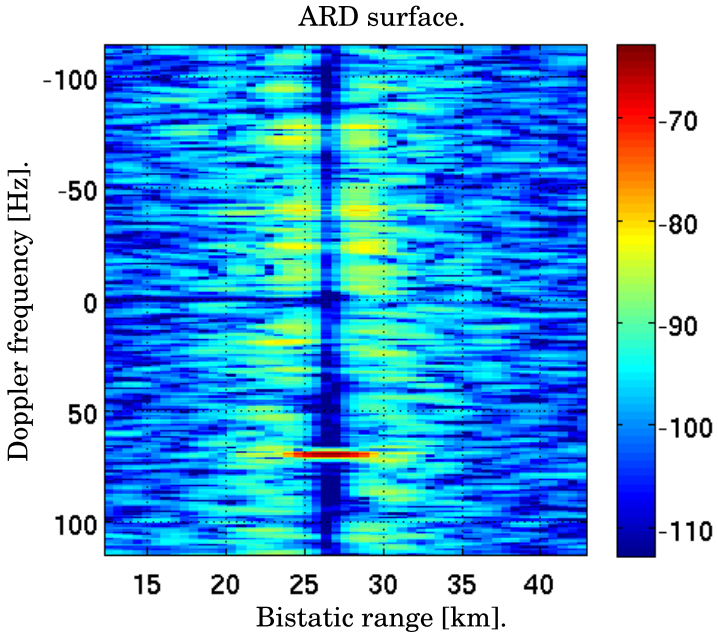

Figure 5.20: The ARD surface obtained after using signal projection to suppress the direct signal and processing the first 1-second block of data. The target is visible.

5.2.5 Clutter Suppression

The matched filter processing confines reflections from stationary targets to the zero-Doppler axis on the ARD surface. Unfortunately, these strong reflections still 'mask' reflections from smaller targets, even when there is a large separation in range and Doppler between them [47]. To investigate the effect of clutter on the ARD surface, another FERS simulation was performed. The simulation setup is similar to the one from the previous section, apart from the fact that there are three targets and two clutter sources. Each target has an RCS of 20 m^2, while each clutter source has an RCS of 5000 m^2. This section will investigate clutter suppression using the RLS and signal projection algorithms, since these algorithms exhibit superior convergence and suppression performance when compared to the NLMS algorithm. Figure 5.21 shows the result of performing the matched filter processing on the reference and surveillance channel signals without suppressing the DPI.

It can be seen that neither the clutter, nor any targets are visible on the ARD surface due to the strong DPI component in the surveillance channel.

RLS Algorithm

Figure 5.22 shows the ARD surface obtained after suppressing the DPI using a 16-tap RLS filter, and performing the matched filter processing on the reference and surveil-

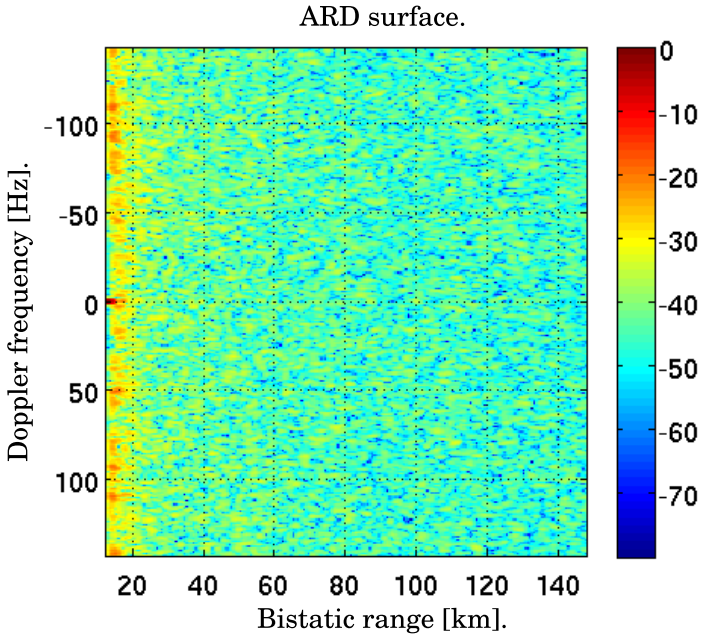

Figure 5.21: The ARD surface obtained after matched filter processing and no direct signal suppression. The strong DPI component clearly masks the clutter and targets on the ARD surface.

lance channel signals.

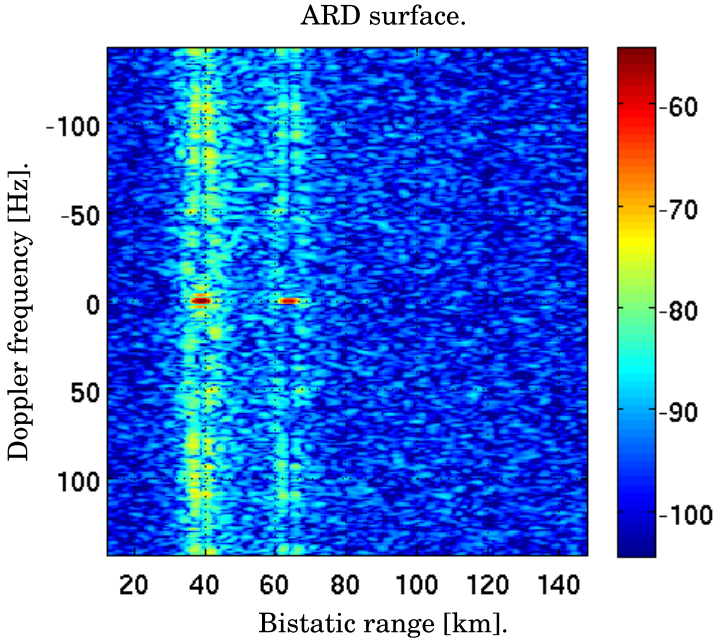

Figure 5.22: The ARD surface obtained after suppressing the DPI component in the surveillance channel using a 16-tap RLS filter and performing the matched filter processing. The two clutter sources are now visible.

The DPI suppression causes the two strong clutter components to be visible on the ARD surface, however, neither of the three targets are yet visible due to the masking effect of the clutter. Figure 5.23 shows the resulting ARD surface after suppressing both the DPI and the clutter using a 100-tap RLS filter, yielding suppression up to a range of 60 km.

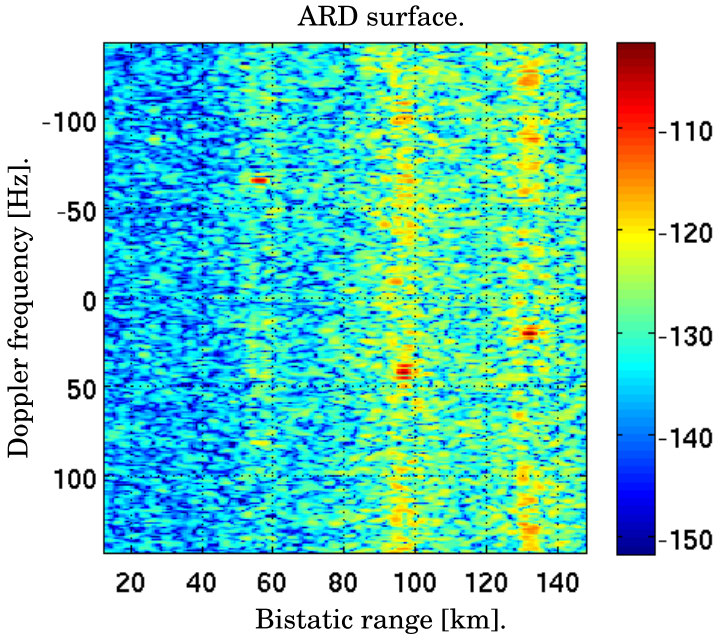

Figure 5.23: The ARD surface obtained after suppressing both the DPI and clutter components using a 100-tap RLS filter. All three targets are now visible.

All three targets are now clearly visible on the ARD surface. The first target falls within the suppression range and is slightly attenuated. The RLS filter also has the effect of suppressing the Doppler sidelobes of the first target.

Signal Projection Algorithm

Figure 5.24 shows the ARD surface after using the signal projection algorithm to suppress the DPI and clutter components over 90 range bins.

The first target is clearly visible, while the two distant targets appear as very small components on the ARD surface. The signal projection algorithm possesses some flexibility in that the A-matrix can be set up to suppress components on the ARD surface at arbitrary range and Doppler values. Figure 5.25 shows the ARD surface after suppressing the closest target.

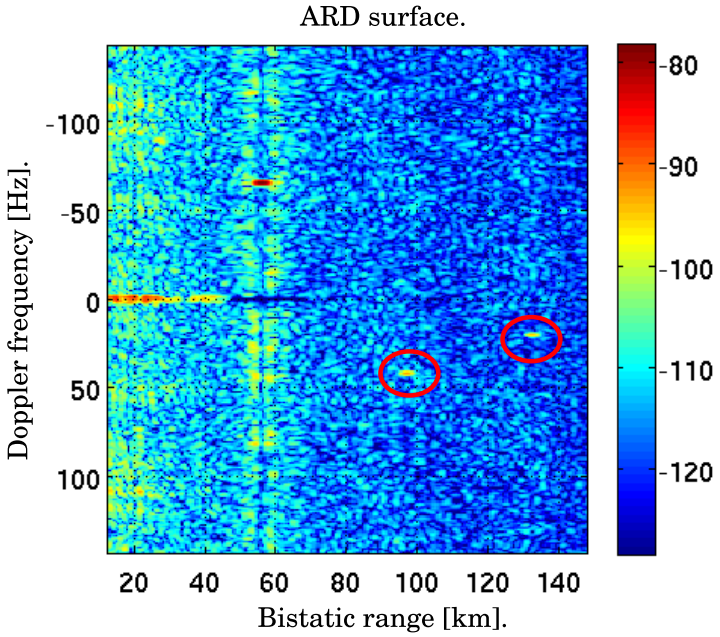

Figure 5.24: The ARD surface obtained after using the signal projection algorithm to suppress the DPI and clutter over 90 range bins. The first target is clearly visible, while the two distant targets appear as small components on the ARD surface.

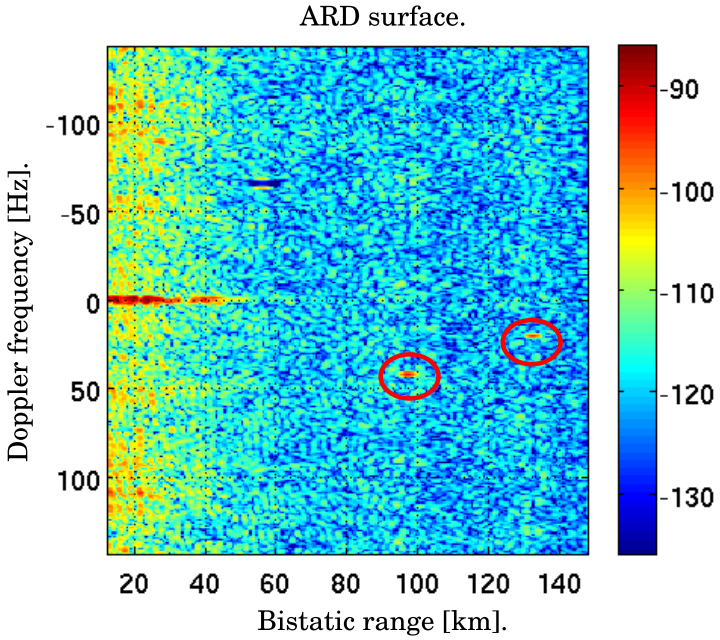

Figure 5.25: The ARD surface obtained after using the signal projection algorithm to suppress the closest target. The two distant targets now appear with higher intensities on the ARD surface.

The two distant targets now appear with higher intensities on the ARD surface. Colone [47] developed a version of the signal projection algorithm, known as the *Extensive Cancellation Algorithm* (ECA). The ECA operates by first suppressing the DPI and clutter

components on the ARD surface. The matched filter processing is then performed and all the strong target returns on the ARD surface are marked and suppressed. The matched filter processing is then repeated, causing previously masked targets to become visible.

5.3 Chapter Summary

This chapter investigated the matched filter and DPI and clutter suppression processing stages of a PCL radar system.

It was found that matched filter processing is required in order to detect targets at different bistatic ranges and Doppler frequencies on the ARD surface. The matched filter also provides the integration gain that is needed for reliable target detection. A simple technique to accelerate the matched filter was investigated. It was found that a theoretical speedup factor of 18 times can be achieved by downsampling the data before calculation of the FFT for each range of interest.

Three different DPI and clutter suppression algorithms were investigated, namely the NLMS, RLS and signal projection algorithms. It was found that the RLS and signal projection algorithms exhibit superior convergence and suppression performance when compared to the NLMS algorithm. This chapter only evaluated the convergence and suppression performance for simulated data. O'Hagan [48] found that the amount of suppression that can be achieved is limited by co-channel interference in the FM band, as well as decorrelating effects and spurious components introduced by analogue components in the receiver. It is therefore expected that the amount of suppression that can be achieved will be lower for real PCL radar data.

Based on the simulation results of the suppression algorithms, it was decided to use the signal projection algorithm in the experimental PCL radar system. The signal projection and RLS algorithms have similar convergence and suppression performances when used to process simulated data. Unlike the RLS and NLMS algorithms, the signal projection algorithm does not require a variable to control the rate of adaptation. This should help the algorithm to be more robust when used in different signal environments.

Chapter 6

Channelisation and Target Location

The geometry of a typical PCL radar system was discussed in Chapter 2. While Figure 2.1 showed only one transmitter, there are often more transmitters in an area transmitting the same waveform, each at a different carrier frequency. Adding a reference antenna for each transmitter and capturing a frequency band wide enough to include all the transmitted frequencies in the surveillance channel, enables a multistatic PCL radar system to be formed. This concept is illustrated in Figure 6.1.

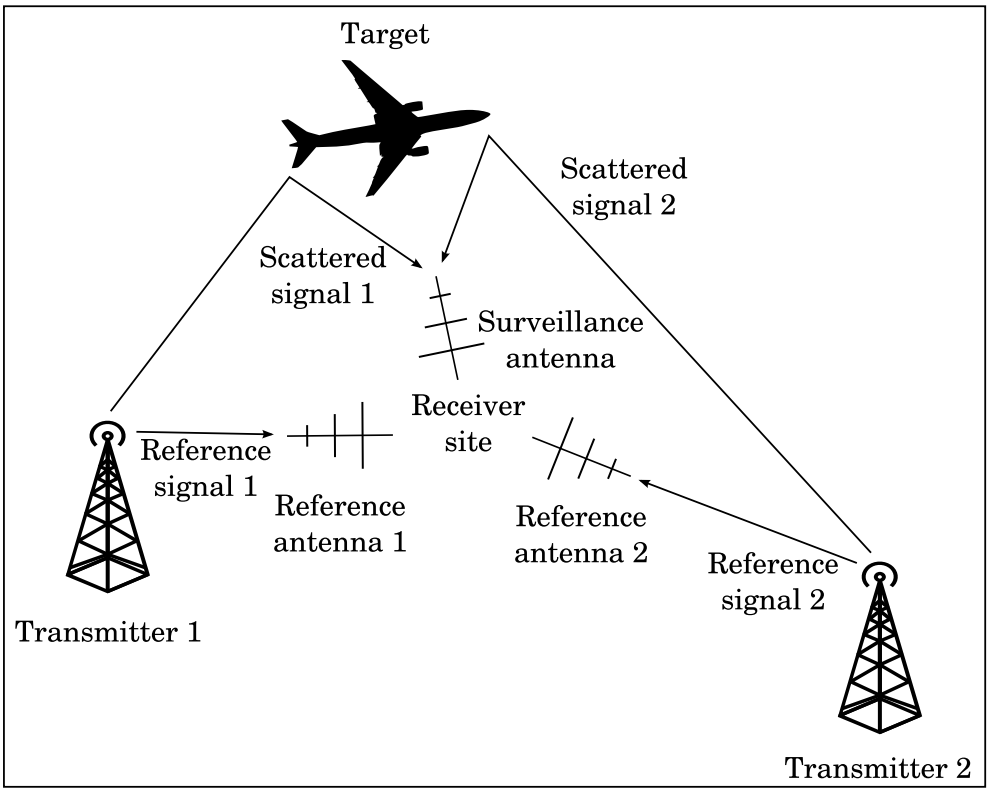

Figure 6.1: The geometry of a PCL radar system that utilises more than one transmitter.

Each additional transmitter forms a bistatic radar with the receiver and provides a unique set of target parameters. By combining the parameters of more than one of these bistatic radars, a target can be located more accurately. This chapter will investigate target location using TDOA measurements. This is known as multilateration [49]. Other useful parameters that are used for target location include Doppler and AOA [50].

6.1 Channelisation

Channelisation is the process whereby a single, a few, or all the channels in a certain frequency band are separated for further processing. Figure 6.2 shows the channelisation of a portion of spectrum into four different channels.

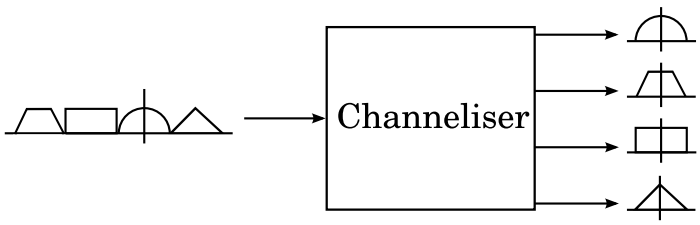

Figure 6.2: Channelising a portion of spectrum into four separate channels.

A number of different channelisation algorithms exist. Savir [51] studied the most commonly used ones, namely the per-channel approach, the pipelined frequency transform (PFT) and the polyphase FFT (PFFT), or PFB. It was found that the FPGA LE requirements of the PFB are by far superior to that of the per-channel approach and the PFT, leading to much smaller designs on FPGAs. For this reason, the PFB will be considered in this chapter.

6.1.1 Polyphase Filterbank

The conventional architecture for a channeliser employs a complex mixer, digital lowpass filter and down-sampler for each channel of interest. A single channel is shown in Figure 6.3.

The equivalency theorem states that a mixer, followed by a lowpass filter is equivalent to a bandpass filter, followed by a mixer [10]. This is illustrated in Figure 6.4.

Due to the down-sampler, only every M^{th} output sample is retained. The mixer therefore only needs to down-convert the retained samples and can be moved through the down-sampler. This is illustrated in Figure 6.5.

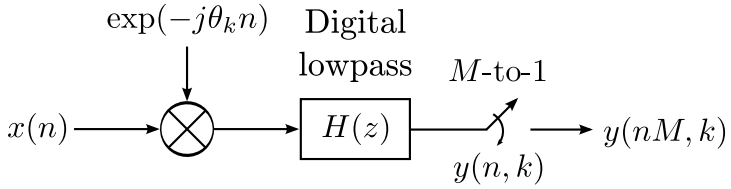

Figure 6.3: Block diagram of a single path in a channeliser [10].

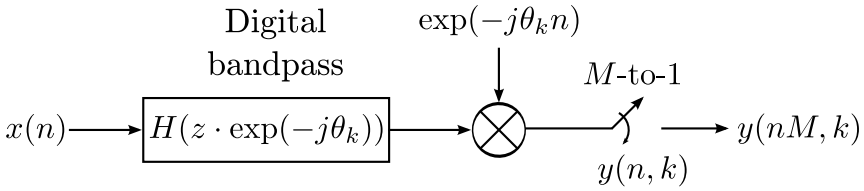

Figure 6.4: Using the equivalency theorem to transform a complex mixer, followed by a lowpass filter to a bandpass filter, followed by a complex mixer [10].

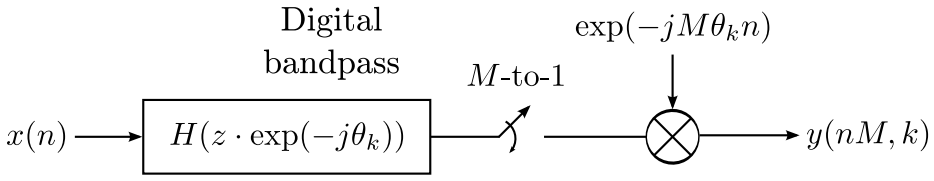

Figure 6.5: Moving the complex mixer through the down-sampler [10].

A further simplification is now possible. The down-sampler causes the rotation rate of the sampled complex sinusoid to change from θ_k to $M\theta_k$. This change in rotation rate has an aliasing effect on the generated sinusoid. By restricting the centre frequencies of the channels of interest so that $\theta_k = \frac{k2\pi}{M}$, each channel will alias to 0, since the rotation rate change is now a multiple of 2 π. The complex mixer can therefore be discarded, leading to the architecture shown in Figure 6.6.

Using polyphase decomposition to split the filter into M-subfilters and invoking the noble identity for decimation, leads to the architecture shown in Figure 6.7.

A lowpass filter can be transformed to a bandpass filter by applying the frequency translation property of the Z-transform [10]. Each z-element is now replaced by $z \cdot \exp(-j\theta)$, where θ is chosen according to the restriction imposed earlier in this section. It should also be noted that the delay elements and down-samplers of the system can be implemented as an input commutator. This leads to the architecture shown in Figure 6.8.

It can be seen that the output of the system, $y(nM,k)$, is computed as the phase coherent summation of the M-output series, $y_r(nM)$. This phase coherent summation is equivalent to a discrete Fourier transform (DFT), which can be implemented as an

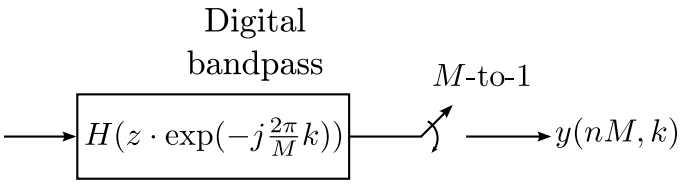

Figure 6.6: Constraining the centre frequency of each channel so that $\theta_k = \frac{k2\pi}{M}$ and discarding the complex mixer [10].

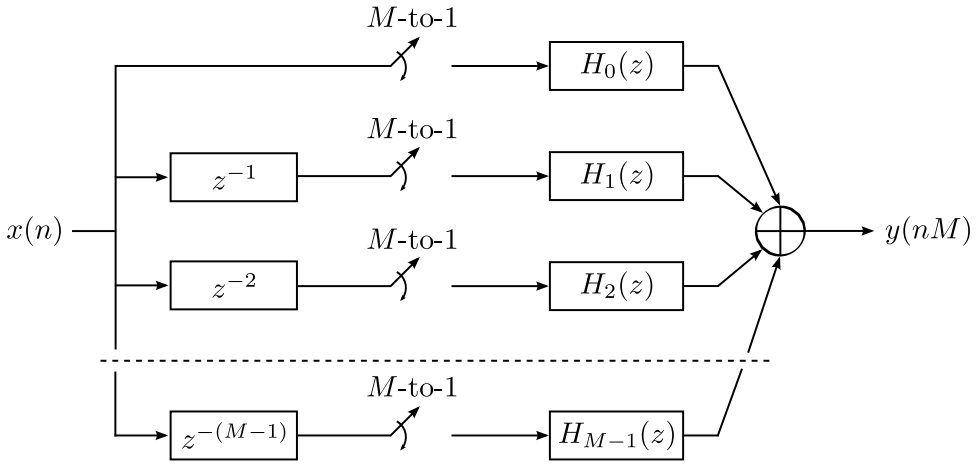

Figure 6.7: Using polyphase decomposition to split the original filter into M-subfilters and invoking the noble identity to move the down-sampler to the front of the filter [10].

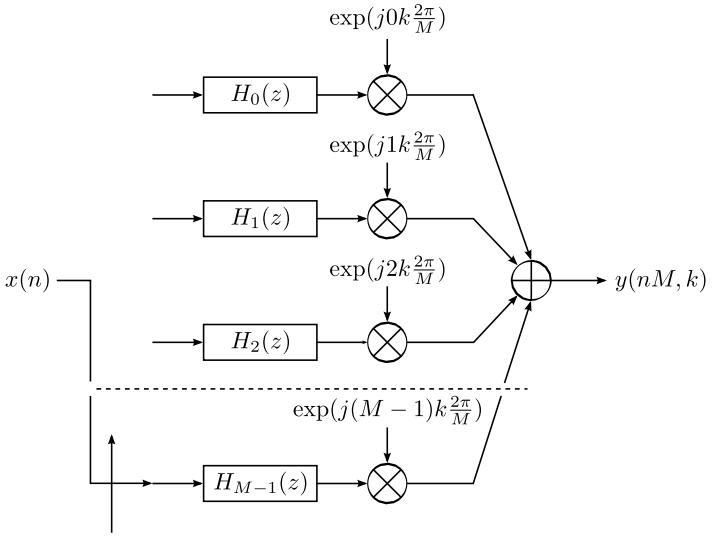

Figure 6.8: Using an input commutator to implement the delay elements and down-samplers and transforming the lowpass filters to bandpass filters [10].

FFT. The final PFB architecture is shown in Figure 6.9.

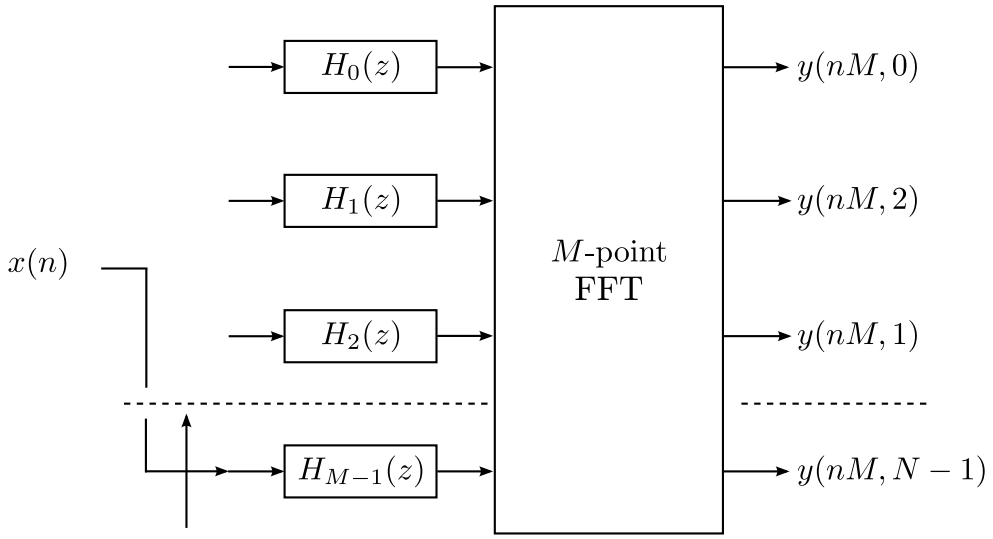

Figure 6.9: The final polyphase filterbank, with input commutator, polyphase filter and FFT [10].

6.1.2 Channelisation and GNURadio

The initial objective was to implement a channeliser on the USRP that would be able to separate a portion of the FM band into different channels. It was found however, that the amount of logic resources on the USRP FPGA are very limited, restricting the customisation that can be performed on the standard FPGA build. It was decided to instead implement a PFB using GNURadio signal processing blocks. The GNURadio filterbank would then be compared to a filterbank written in Matlab to verify its functionality.

GNURadio Polyphase Filterbank

It was shown in Chapter 4 that the USRP can sustain a maximum single channel transfer rate of 4 MSPS, corresponding to a sampling frequency of 4 MHz. Each FM radio station is allocated a 200 kHz-wide portion of the FM radio band. Therefore, to separate 4 MHz of bandwidth into channels that are 200 kHz wide, a 20-channel PFB is required.

The first step in implementing a PFB requires a prototype filter to be designed. For the required application the prototype filter should have a stopband edge frequency of 100 kHz. Table 6.1 shows the parameters of the filter that was designed, while Figure 6.10 shows its magnitude response.

Table 6.1: Parameters of the prototype lowpass filter.

Design Method	Equiripple
Density Factor	20
Sampling Frequency	4 MHz
Passband Edge Frequency	50 kHz
Stopband Edge Frequency	100 kHz
Passband Attenuation	1 dB
Stopband Attenuation	78.5 dB
Filter Order	200

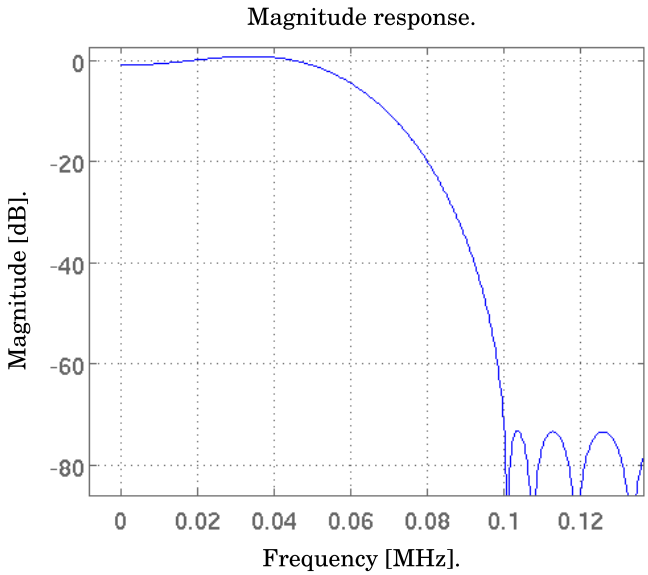

Figure 6.10: Magnitude response of the prototype lowpass filter.

Using polyphase decomposition on the filter yields twenty 10-tap subfilters. Figure 6.11 shows the GNURadio blocks that were used to implement the PFB.

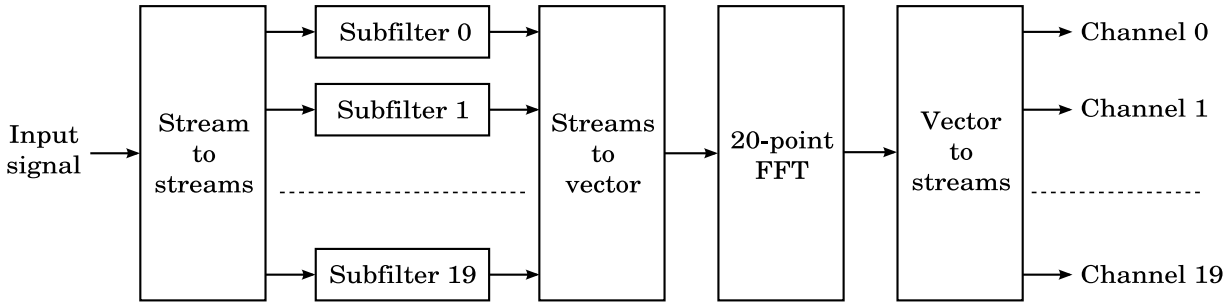

Figure 6.11: A block diagram of the GNURadio PFB.

The *stream to streams* block is used to split the input signal into different streams and performs the role of the input commutator. The *streams to vector* and *vector to streams* blocks are required when interfacing to the GNURadio FFT block.

To test the GNURadio PFB, a 4 MHz-wide portion of the FM band was captured at UCT. The signal spectrum is shown in Figure 6.12.

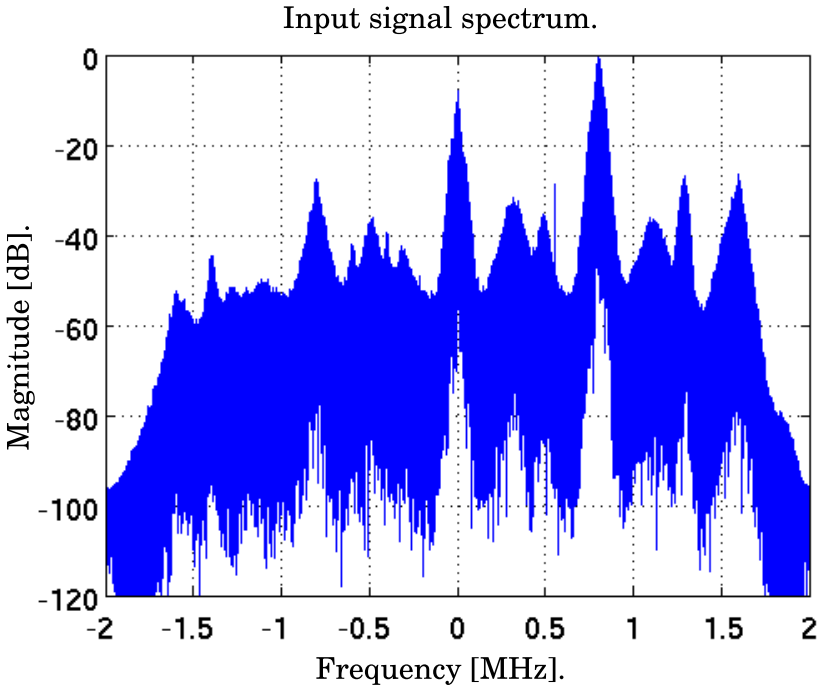

Figure 6.12: The spectrum of the captured signal that was used to test the PFB.

The captured portion of the FM band was mixed down by 88.2 MHz. Therefore, 0 on the above figure corresponds to the station located at 88.2 MHz in the FM radio band, while the strong signal at 800kHz corresponds to the signal located at 89 MHz. As mentioned in Chapter 3, the 5FM radio station is transmitted by the Tygerberg FM transmitter at 88.2 MHz and by the Constantiaberg FM transmitter at 89 MHz.

Both the GNURadio PFB and the PFB written in Matlab were used to channelise the input signal. Because of the output order of an FFT, the Channel 0 output shown in Figure 6.11 should contain the FM radio station at 0, Channels 1 to 9 should contain the stations from 200 kHz up to 1.8 MHz, Channel 10 should contain half of the station at 2 MHz and half of the station at -2 MHz, while channels 11 to 19 should contain the stations from -1.8 MHz up to -200 kHz. Figure 6.13 shows the Channel 0 output spectrum of both the Matlab PFB and the GNURadio PFB, while Figure 6.14 shows the Channel 4 output spectrum.

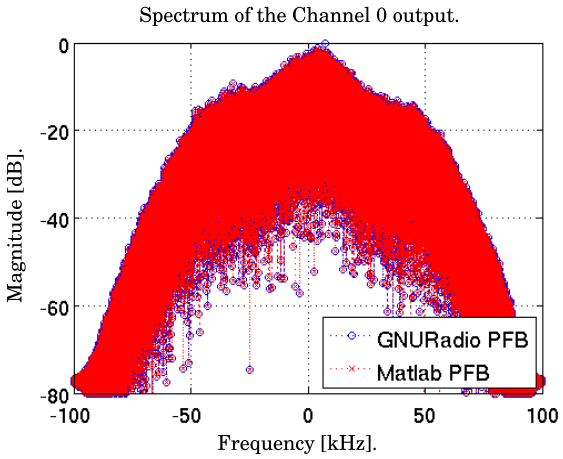

Figure 6.13: Spectrum of the Channel 0 PFB output signal, corresponding to the FM radio station located at 88.2 MHz.

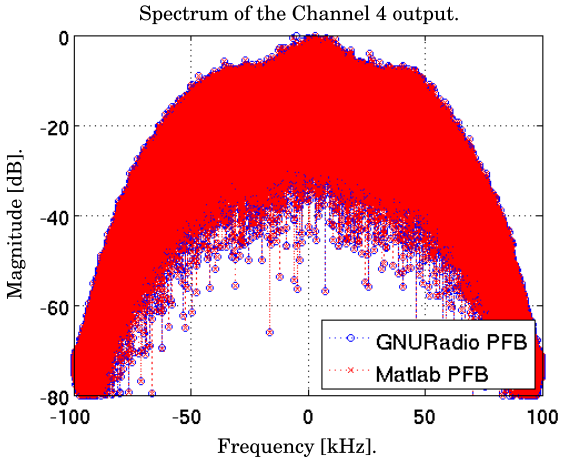

Figure 6.14: Spectrum of the Channel 4 PFB output signal, corresponding to the FM radio station located at 89 MHz.

Figures 6.13 and 6.14 both show that the output obtained with the GNURadio PFB exactly matches the output obtained with the Matlab PFB. The spectra shown in Figures 6.12 and 6.13 are also very similar, since both contain the same FM signal, originating from two different transmitters. As a final test, a GNURadio application was written to demodulate the outputs of the PFB. It was found that all the output channels occupied by FM radio stations could be correctly demodulated and listened to. The Channel 0 and Channel 4 outputs also produce the same demodulated audio signal, since both contain the same FM radio station. The GNURadio PFB was therefore found to be functioning correctly.

6.2 Multilateration

The contour of constant bistatic range was introduced in Chapter 2. For each additional transmitter utilised in a PCL radar system, an additional contour of constant bistatic range is obtained, with the receiver and transmitter as the foci. Two of these contours intersect in two different points, one being the location of the target and the other that of a false target. Utilising three different transmitters allows the correct target location to be determined.

The ellipsoids describing the bistatic range of a target when using three different transmitters and a single receiver are defined as

$$\begin{aligned}
\sqrt{(x_R-x)^2+(y_R-y)^2+(z_R-z)^2}+\sqrt{(x_1-x)^2+(y_1-y)^2+(z_1-z)^2} &= R_1 \\
\sqrt{(x_R-x)^2+(y_R-y)^2+(z_R-z)^2}+\sqrt{(x_2-x)^2+(y_2-y)^2+(z_2-z)^2} &= R_2 \\
\sqrt{(x_R-x)^2+(y_R-y)^2+(z_R-z)^2}+\sqrt{(x_3-x)^2+(y_3-y)^2+(z_3-z)^2} &= R_3
\end{aligned} \tag{6.1}$$

where

(x_R, y_R, z_R)	are the receiver coordinates
(x_1, y_1, z_1)	are the first transmitter's coordinates
(x_2, y_2, z_2)	are the second transmitter's coordinates
(x_3, y_3, z_3)	are the third transmitter's coordinates
R_1	is the bistatic range of the first contour
R_2	is the bistatic range of the second contour
R_3	is the bistatic range of the third contour

Rearranging terms and squaring both sides of each ellipsoid equation yields three equations of the form

$$\begin{aligned}
\sqrt{(x_R-x)^2+(y_R-y)^2+(z_R-z)^2} = -\tfrac{1}{2R_N}[2x(x_R-x_N)+2y(y_R-y_N)+\dots \\
\dots 2z(z_R-z_N)-x_R^2-y_R^2-z_R^2+x_N^2+y_N^2+z_N^2-R_N^2]
\end{aligned} \tag{6.2}$$

where N refers to the transmitter associated with the current ellipsoid [52]. Equating the first ellipsoid with the second and third produces two plane equations of the form

$$x = A_N y + B_N z + C_N \tag{6.3}$$

Equating the two plane equations produces a linear equation in terms of y and z. Substituting this linear equation into any of the two plane equations produces a linear equation in terms of x and z. These two linear equations are now substituted back into the equation of any of the three ellipsoids. By squaring both sides of the ellipsoid equation and rearranging terms, it can be shown that

$$Dz^2 - Ez - F = 0 \tag{6.4}$$

The roots of the above equation are easily obtained. Any of the two solutions for z can now be substituted back into the two linear equations to obtain the x-and y-coordinates. A Python script was written to calculate the target coordinates by using three TDOA measurements. It was found that the x-and y-coordinates of a target could be correctly calculated, but that a height ambiguity exists. This is represented by the two roots of

Equation 6.4. It was also found that the ambiguous height is negative in most cases and can therefore be discarded. As a further investigation, the solution was extended to four transmitters and a single receiver. It was found that the additional TDOA measurement provided by the fourth transmitter allowed the height of the target to be calculated unambiguously.

6.2.1 Multilateration Simulation

To determine how channelisation and multilateration could be utilised by a PCL receiver located at UCT, a FERS simulation was performed. Three high-power transmitters are detectable at UCT. The coordinates relative to UCT, and the effective radiated power (ERP) of each transmitter is shown in Figure 6.15.

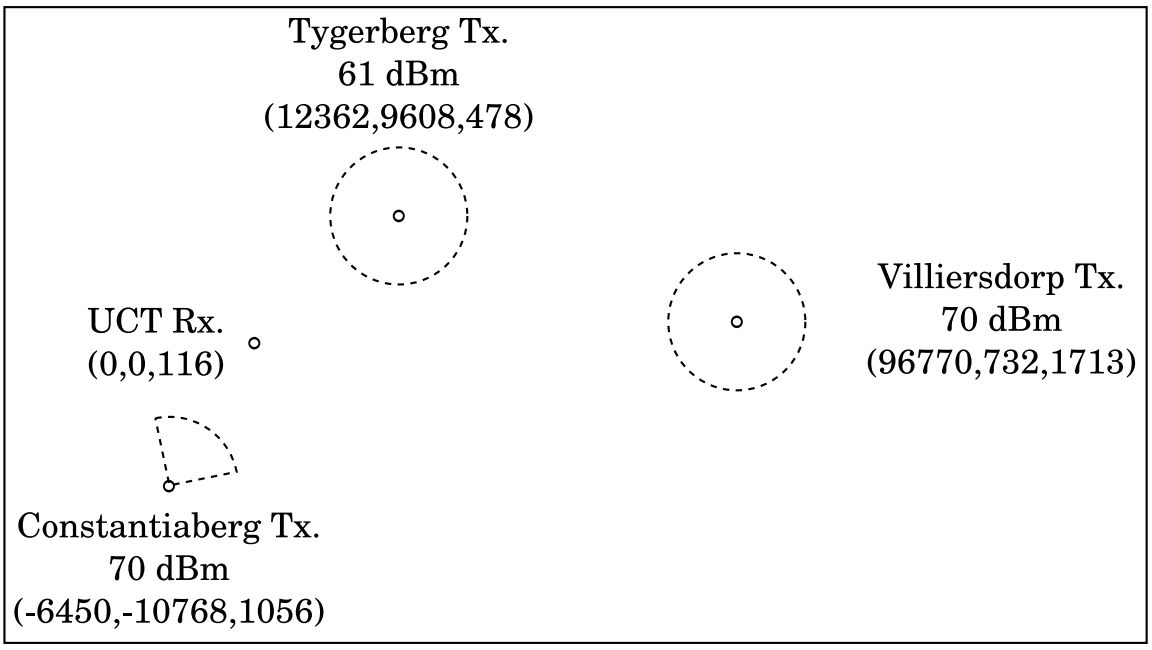

Figure 6.15: The high-power transmitters in the UCT area. All the coordinates are in metres.

Both the Villiersdorp and the Tygerberg transmitters have omnidirectional antennas, while the approximate antenna pattern of the Constantiaberg transmitter is shown in the figure. For the simulation, 1 second of an audio signal containing music was FM modulated using a GNURadio script. The Tygerberg, Constantiaberg and Villiersdorp transmitters were modelled as having transmit frequencies of 88.8 MHz, 89 MHz and 89.2 MHz respectively. For simplicity, all the transmitters were also modelled as having omnidirectional antennas. A target was then simulated with coordinates $(-10000, 30000, 1600)$ at $t = 0$ s and $(-9800, 30000, 1600)$ at $t = 1$ s. DPI suppression was performed by first running the simulation without a target to obtain a clean reference

signal. The simulation was then repeated, this time including a target. The clean reference signal was then subtracted from the received surveillance signal to obtain the reflected target signal. The spectrum of the surveillance channel after subtracting the reference signal is shown in Figure 6.16. The received surveillance signals are all normalised relative to the strongest direct signal.

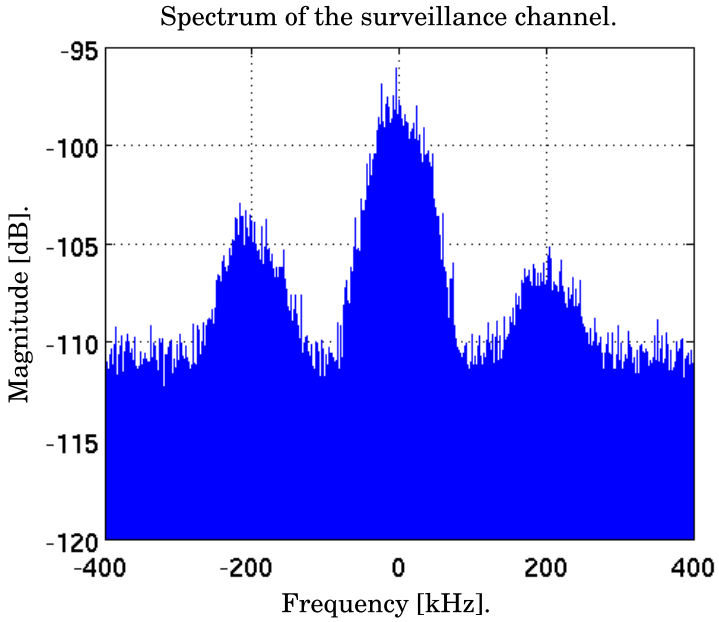

Figure 6.16: Spectrum of the surveillance channel. The received surveillance signals are all normalised relative to the strongest direct signal.

A simple 4-channel PFB was written in Matlab and used to separate the above spectrum into four different channels, of which three are of interest. Each channel was then matched-filtered with the appropriate direct signal to produce an ARD surface. The ARD surface produced by matched-filtering the signal received from the Tygerberg transmitter with the associated output channel from the PFB, is shown in Figure 6.17, while Figure 6.18 shows the area around the target reflection in more detail.

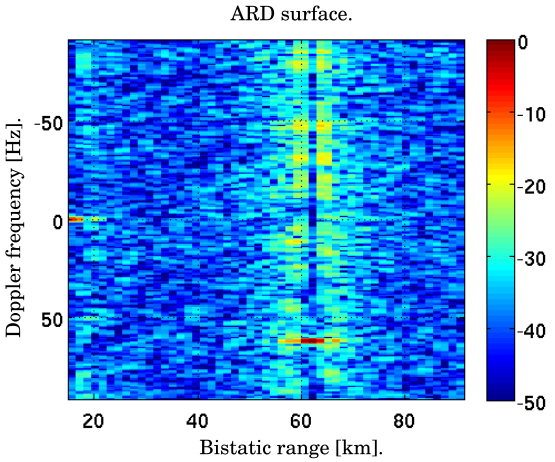

Figure 6.17: The ARD surface produced by matched-filtering the direct signal received from the Tygerberg transmitter with the associated surveillance signal channel.

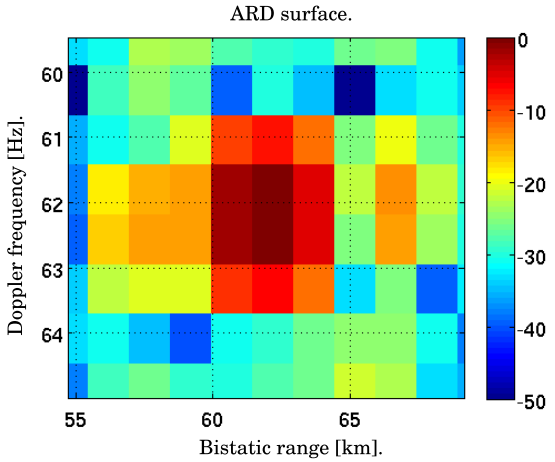

Figure 6.18: The area around the target reflection in more detail.

Figure 6.19 shows the ARD surface produced by matched-filtering the signal received from the Constantiaberg transmitter with the associated output channel from the PFB, while Figure 6.20 shows the area around the target reflection in more detail.

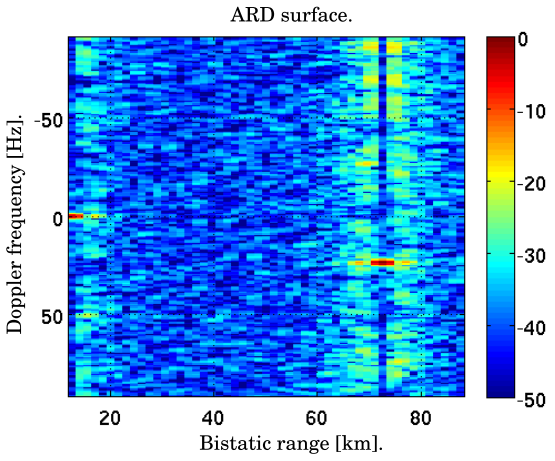

Figure 6.19: The ARD surface produced by matched-filtering the direct signal received from the Constantiaberg transmitter with the associated surveillance signal channel.

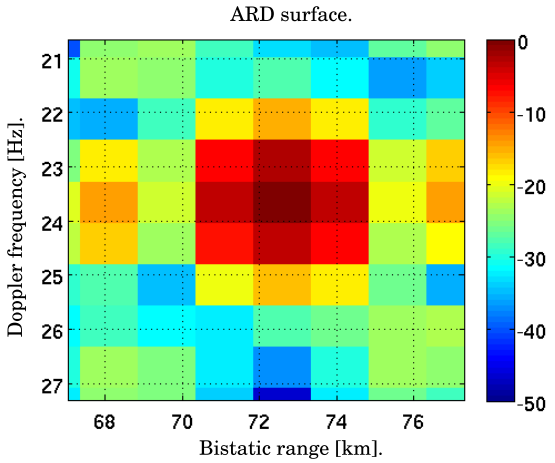

Figure 6.20: The area around the target reflection in more detail.

Figure 6.21 shows the ARD surface produced by matched-filtering the signal received from the Villiersdorp transmitter with the associated output channel from the PFB, while Figure 6.22 shows the area around the target reflection in more detail.

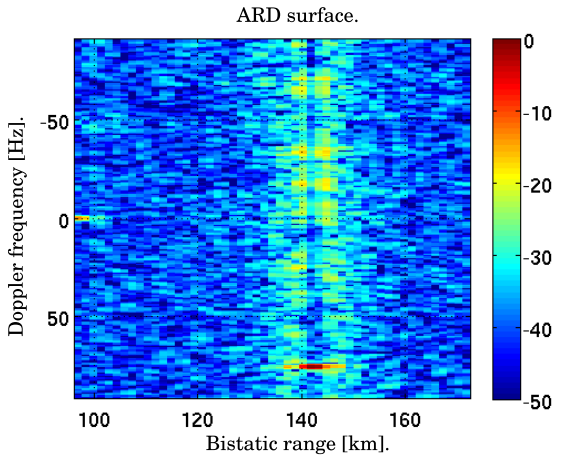

Figure 6.21: The ARD surface produced by matched-filtering the direct signal received from the Villiersdorp transmitter with the associated surveillance signal channel.

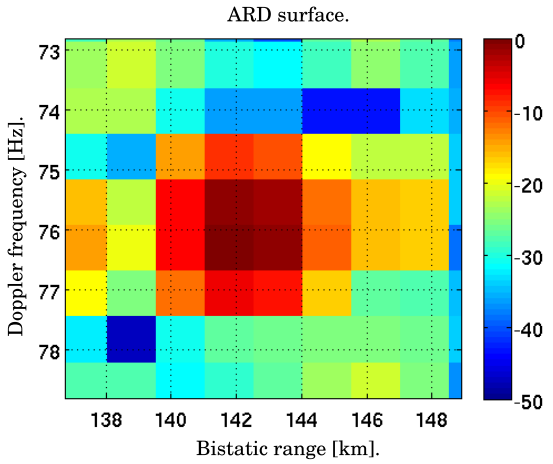

Figure 6.22: The area around the target reflection in more detail.

A basic Matlab function was written to determine the bistatic range of the target reflection on each ARD surface by searching for the maximum peak. Table 6.2 compares the obtained values with the actual calculated values.

Table 6.2: Comparing the target bistatic range of each ARD surface to the actual calculated values.

Tygerberg transmitter			
	ARD surface	Calculated	Error
Bistatic range	62160.9 m	61942.1 m	218.8 m
Constantiaberg transmitter			
	ARD surface	Calculated	Error
Bistatic range	72577.4 m	72585.1 m	7.7 m
Villiersdorp transmitter			
	ARD surface	Calculated	Error
Bistatic range	142520.56 m	142366 m	154.56 m

Table 6.2 shows a maximum bistatic range error of 218.8 m. The range errors can be attributed to the poor range resolution of FM signals. For the simulation, an FM signal

modulated by an audio signal containing music was used. The range errors will be larger for FM signals that are modulated by audio signals containing speech, due to the smaller resulting bandwidth and poorer range resolution. Figure 6.23 shows the three contours of constant bistatic range for the simulated target. The position of the target is represented by the intersection of the three contours.

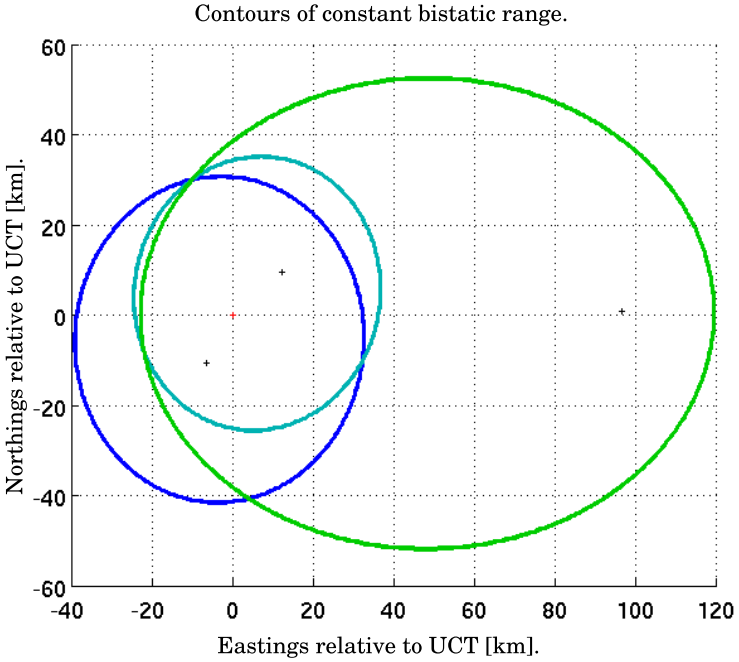

Figure 6.23: The contours of constant bistatic range for the three transmitters. The target is located at the intersection of all three contours.

The bistatic range value of each ARD surface was used, along with the Python script, to calculate the coordinates of the target by solving the intersection of the three contours. Figure 6.24 shows a screen capture of the Python script after calculating the target coordinates.

The calculated coordinates of the target are $(-10117.077, 29802.614, 4109.655)$, while the actual coordinates are $(-10000, 30000, 1600)$. The calculated x-and y-coordinates are close to the actual values, with a significant error in the calculated z-coordinate. As a further investigation, the Python script was used to calculate the target coordinates when using the actual bistatic range values. Figure 6.25 shows a screen capture of the Python script after calculating the coordinates.

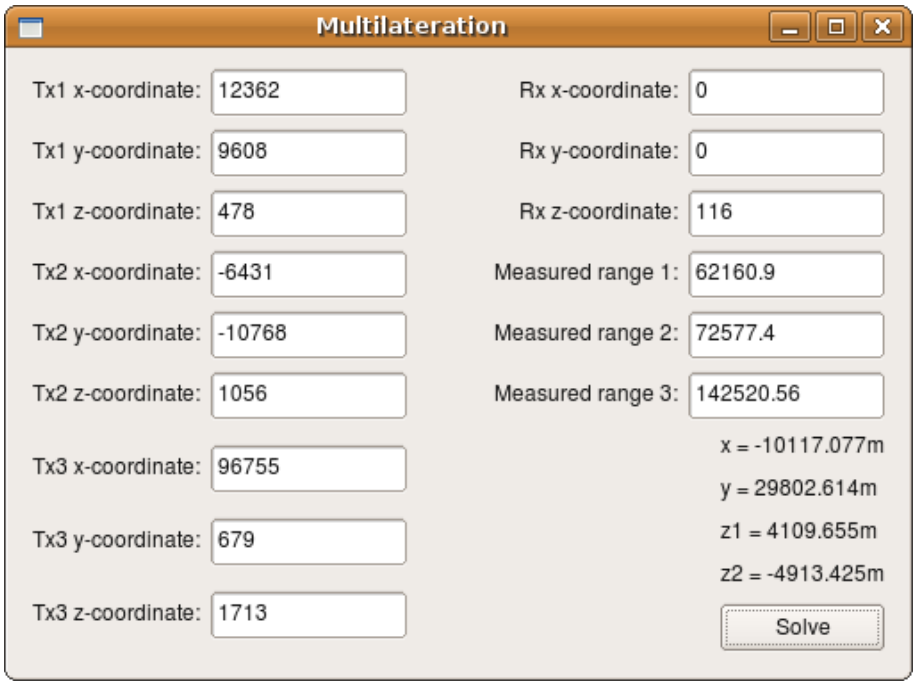

Figure 6.24: A screen capture of the Python script that was written to calculate the coordinates of a target by using three different bistatic range measurements.

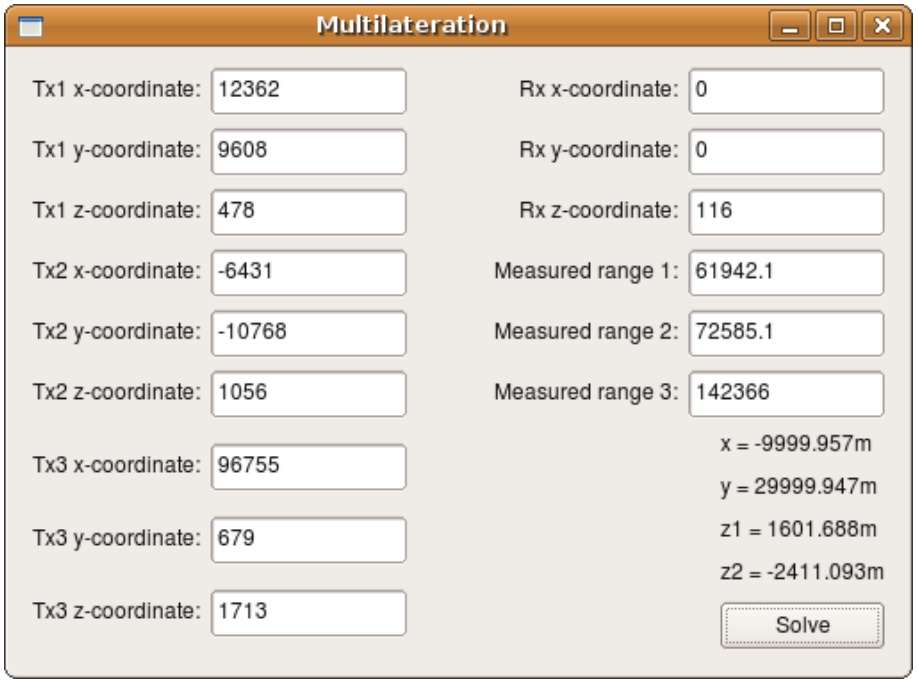

Figure 6.25: A screen capture of the Python script when using the actual bistatic ranges to calculate the target coordinates.

It can be seen that the calculated target coordinates are very close to the correct coordinates. Norouzi [53] showed that the accuracy of the calculated target coordinates are highly sensitive to the TDOA (or bistatic range) errors when using multilateration for target location. In his work, Norouzi also discusses a joint target location technique using TDOA, as well as AOA measurements and shows that greater accuracy can be achieved.

A further problem with multilateration occurs when multiple targets are present in the environment. Multiple contours of constant bistatic range now exist for each transmitter-receiver pair, and calculating the exact intersection of the contours from three different transmitters becomes a difficult task. For N transmitter-receiver pairs and M targets in an environment, the number of intersections are equal to $N.(N-1)M^2$ [42]. Therefore, using 3 transmitter-receiver pairs and having 5 targets present in the environment leads to 150 contour intersections, of which only 5 correspond to real targets. Clearly, other techniques that use additional target information such as AOA and Doppler measurements should be used for target location in practical, real-world PCL radar systems.

6.3 Chapter Summary

This chapter investigated the channelisation of a portion of spectrum into different channels with the aim of implementing a channeliser on the USRP FPGA. Target location using multilateration was also investigated. With regards to channelisation, the following observations were made

- The PFB is the most efficient channeliser structure for FPGA implementation, as it occupies the least amount of logic resources when compared to other structures.
- The USRP FPGA has a very limited number of logic resources available for customisation. These resources are not sufficient to implement a PFB on the FPGA. The USRP 2[1] uses a Xilinx[2] Spartan3-2000 FPGA. This particular FPGA has almost four times the amount of LEs than the Cyclone FPGA on the USRP. The FPGA also has 40 hardware multipliers. The larger FPGA should make the implementation of a PFB on the USRP 2 possible.
- A downside to using a PFB for channelisation is that all the channels need be spaced at equal intervals. In the FM band, each channel is allocated 200 kHz of

[1]Accessed 1 March 2010, <http://gnuradio.org/redmine/wiki/gnuradio/USRP2>.
[2]Accessed 1 March 2010, <http://www.xilinx.com>.

bandwidth, but all the channels are not found at multiples of this value. The PFB will therefore not be able to extract every channel from a portion of the FM band.

- A channeliser can be used to implement *dynamic waveform selection* [54]. Because the range resolution of FM signals is dependent on the content of the modulating signal, there will always be instances in time when some signals are more suitable for PCL radar than others. By channelising the FM band into separate channels, each channel can be monitored, allowing the most favourable signals to be used for target detection. This will ensure maximum temporal coverage.

With regards to multilateration, the following observations were made

- The coordinates of a target can be calculated by solving the intersection of three contours of constant bistatic range. A FERS simulation showed that the accuracy of the calculated coordinates is influenced by the accuracy of the bistatic range measurements. The simulation also showed that small bistatic range errors lead to a large error in the calculated z-coordinate of a target. High-bandwidth signals such as DVB-T transmissions, which allow very accurate bistatic range measurements, are therefore the most suitable candidates for target location using multilateration.

- Multilateration presents new challenges and requires the design of more complicated PCL radar systems. For a multilateration system exploiting three transmitters, three highly-directional reference signal antennas are required, as well as a surveillance signal antenna with nulls in the direction of each transmitter, to provide DPI suppression.

- When multiple targets are present in the environment, a large amount of false targets are created. Therefore, more advanced techniques employing TDOA, AOA and Doppler measurements should be used to distinguish actual targets from false ones.

Chapter 7

A Complete PCL Radar System

The previous chapters all detailed the design and evaluation of various components of a PCL radar system. This chapter draws all the components together into a complete system that is able to detect commercial passenger aircraft. This chapter commences with a description of the receiver site that was chosen to perform the final PCL radar experiment on the 22nd of January 2010. Details of the experimental setup, as well as an explanation as to how all the components were integrated into the final PCL radar system are given. The measurements that were taken are presented, as well as the results after processing the data with the signal processing algorithms that were implemented in Chapter 5. This chapter concludes with a discussion of the results.

7.1 The Receiver Site

To test the PCL radar system, it was decided to use a location with the following properties

- It should be in an area with a high volume of commercial air traffic. The bistatic geometry should also be of such a nature that aircraft present a high Doppler to the receiver.
- The location of the receiver should allow both the Constantiaberg and Tygerberg transmitters to be placed in the backlobe of the surveillance channel antenna.

Figure 7.1 shows the location of the receiver, the Constantiaberg and Tygerberg transmitters and Cape Town International Airport. The arrow indicates the direction that landing aircraft fly as they approach the airport.

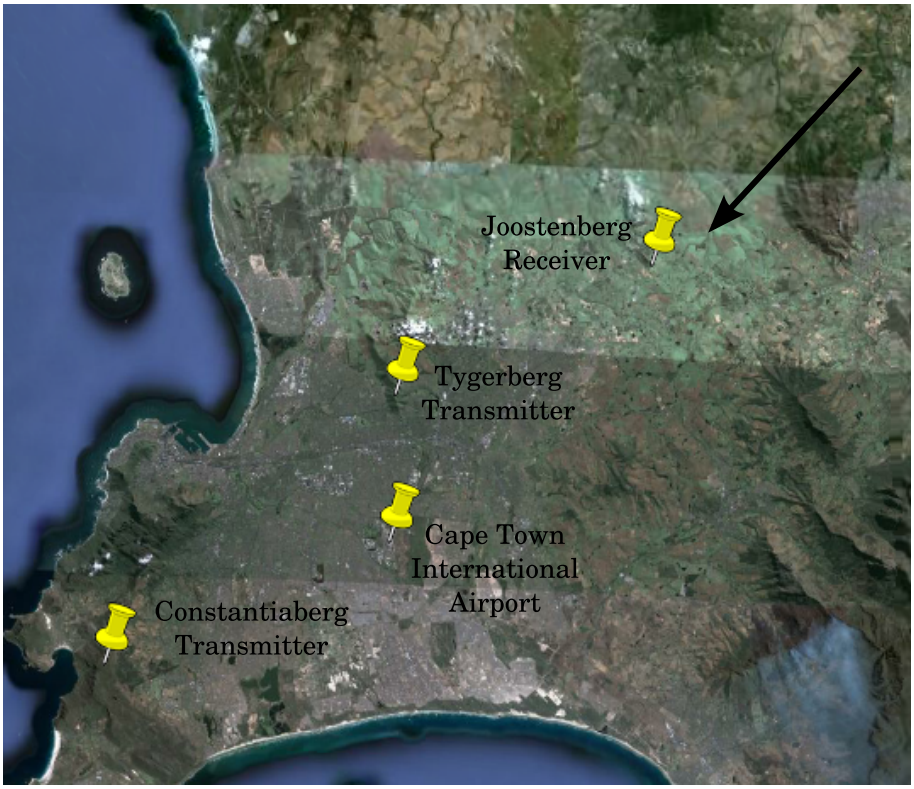

Figure 7.1: The location of the receiver, the two transmitters and Cape Town International Airport. The arrow indicates the direction that landing aircraft fly.

It can be seen that the surveillance antenna can be pointed in a northeastern direction, thereby placing both transmitters in its backlobe. The location of the receiver and transmitters, and the direction that the aircraft fly from creates a geometry that is close to monostatic. Aircraft should therefore present a high Doppler to the receiver. The distance from the receiver site to the Tygerberg transmitter is 21 km, while the distance to the Constantiaberg transmitter is 48.3 km.

7.2 The Experimental Setup

Figure 7.2 shows the receiver site in more detail. Two 4-element Yagi antennas were used as the reference and surveillance channel antennas. The directions in which the reference and surveillance antennas were pointing at is also shown.

For additional DPI suppression, the surveillance antenna was mounted horisontally. The Constantiaberg and Tygerberg transmitters transmit FM radio stations with a vertical polarisation. Mounting the surveillance antenna horisontally provides additional cross-polarisation suppression of the direct signal [48]. Figure 7.3 shows a block diagram of the experimental setup.

Figure 7.2: The receiver site in more detail. The directions in which the reference and surveillance antennas were pointing at is also shown.

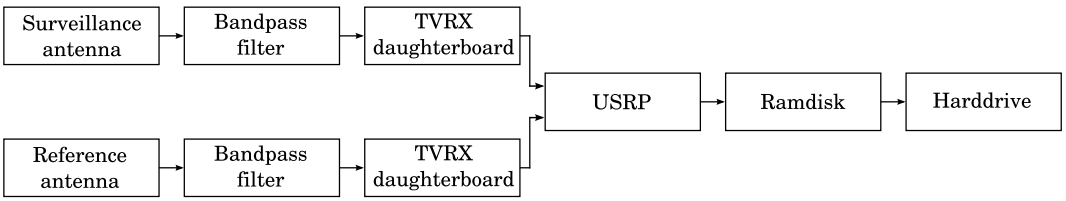

Figure 7.3: A block diagram of the experimental setup used to capture the measurements.

To minimise aliasing due to decimation of data in the USRP, the surveillance and reference channels were sampled at the maximum achievable rate of 4 MSPS. It was found that capturing data at this rate produced a large number of USRP overruns, resulting in samples being dropped. After investigating this problem, it was found that the hard disk drive of the laptop computer that was used for the field measurements could not write the samples to disk at the required speed. The solution to this problem involved first writing samples to a file on a ramdisk, before transferring the file to the hard disk drive. A ramdisk is a Linux feature that allows a portion of random-access memory (RAM) to be used like a normal hard disk drive, but with increased transfer speeds. It was found that this approach corrected the problem and allowed the surveillance and reference channels to be sampled at the maximum rate. Figure 7.4 shows a picture of the USRP, two TVRX daughterboards and the two bandpass filters.

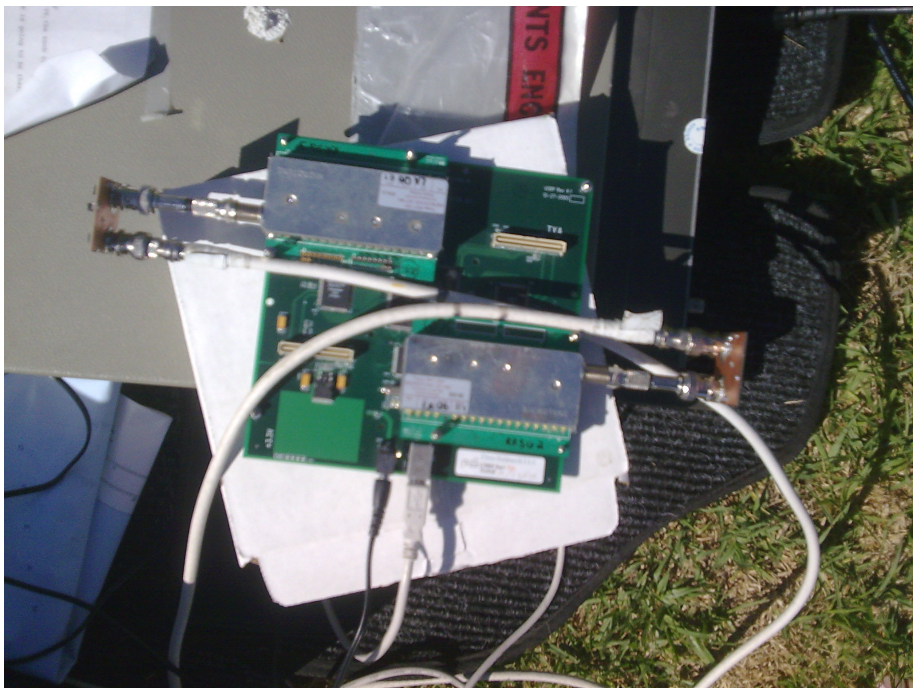

Figure 7.4: The USRP setup, showing two TVRX daughterboards and two bandpass filters, as well as the cables coming from the antennas.

To determine the correct amplifier gain settings, an Agilent N9912A FieldFox handheld spectrum analyser was used to measure the band power in a 6 MHz bandwidth around 88.2 MHz. Table 7.1 shows the measured band powers for the reference and surveillance channels, as well as the amplifier gain settings that were chosen.

Table 7.1: The measured band powers of the reference and surveillance channels, as well as the amplifier gain settings that were chosen.

	Band power [dBm]	RF amplifier [dB]	IF amplifier [dB]
Reference channel	-37.6	35	0
Surveillance channel (V)	-48.6	35	20
Surveillance channel (H)	-57.6	35	30

Table 7.1 shows that 11 dB of DPI suppression is obtained by placing the strong transmitters in the backlobe of the surveillance antenna. Mounting the surveillance antenna horisontally adds an additional 9 dB of DPI suppression, for a total of 20 dB. By referring to Figure 3.7 of Chapter 3, it can be seen that for an input signal power of -57.6 dBm, and RF and IF amplifier gain settings of 35 dB and 20 dB, the output signal power should be approximately -10 dBm. 17 dB of A/D converter dynamic range is therefore lost. Figure 3.11 of Chapter 3 also shows that for an output signal power of -10 dBm, the power of the third-order distortion products is approximately 20 dB below the power of the desired signal.

7.3 PCL Measurements and Processing Results

PCL measurements were performed by capturing 5-second bursts of reference and surveillance channel data and saving it to disk. For all the measurements, the two TVRX daughterboards were tuned to 87 MHz, causing signals above 90 MHz to be attenuated by the bandpass filters in the receivers. The DDC was then used to down-convert the desired signals to baseband. Figure 7.5 shows the spectrum of the reference channel that was captured during one of the bursts.

The strong signals at 500 kHz and 1.3 MHz correspond to the 5FM radio station transmitted by the Tygerberg and Constantiaberg transmitters respectively. Figure 7.5 also shows that the 5FM radio station from Tygerberg is received with an SNR of approximately 55 dB, while the 5FM radio station from Constantiaberg is received with an SNR of approximately 45 dB. Figure 7.6 shows the spectrum of the corresponding surveillance channel.

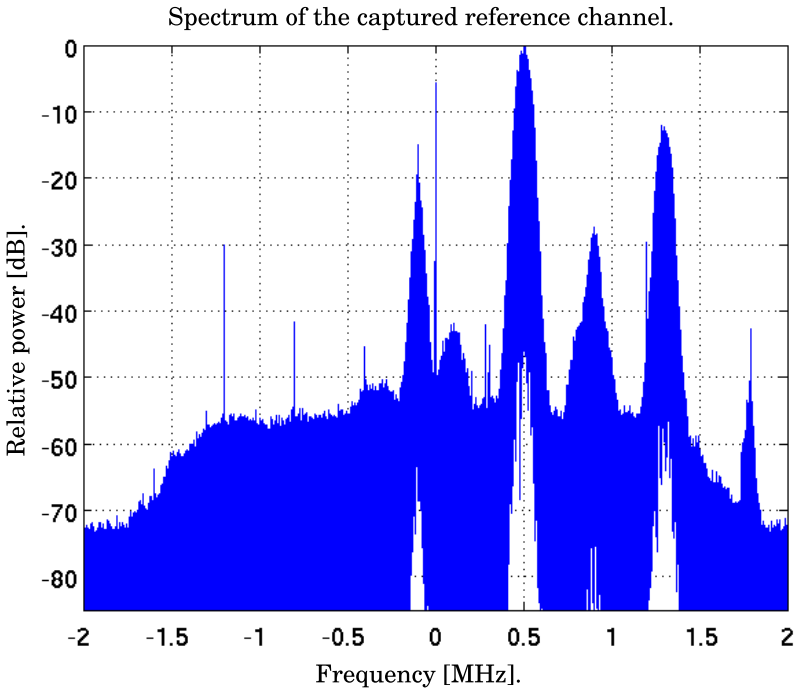

Figure 7.5: The spectrum of the captured reference channel. The two signals of interest are at 500 kHz and 1.3 MHz.

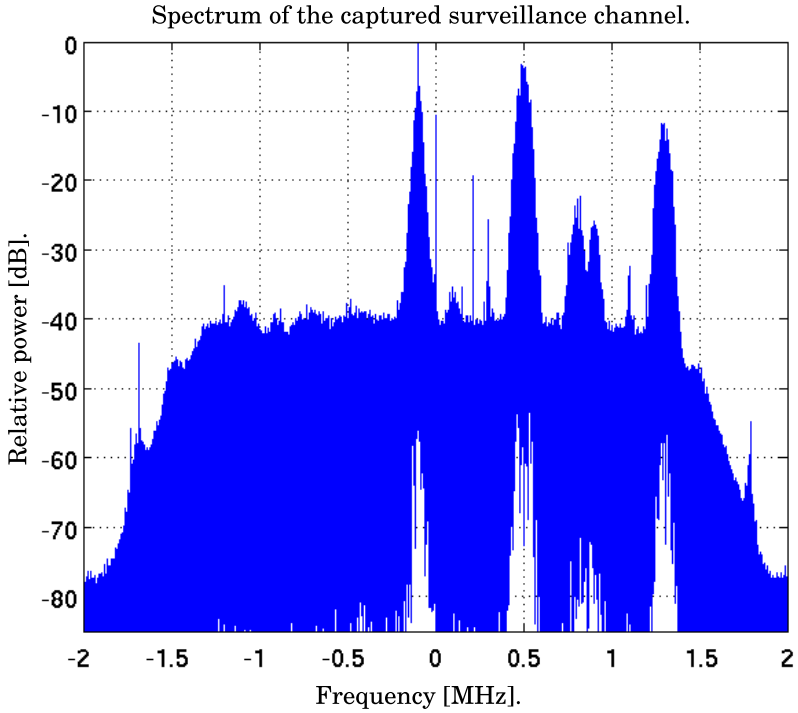

Figure 7.6: The spectrum of the corresponding captured surveillance channel.

It can be seen that the 5FM radio station transmitted by the Tygerberg transmitter is received with an SNR of approximately 37 dB, while the 5FM radio station transmitted by the Constantiaberg transmitter is received with an SNR of approximately 30 dB. Figure 7.7 shows a block diagram of the different signal processing stages that were performed on the captured reference and surveillance channel signals.

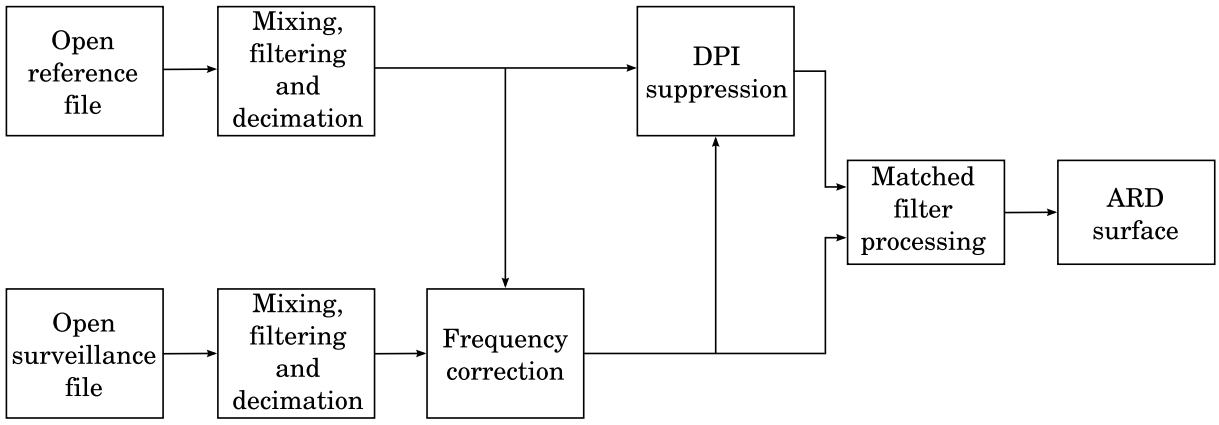

Figure 7.7: A block diagram showing the different signal processing stages that were used to process the reference and surveillance signals.

The mixing, filtering and decimation stages involves mixing the desired channel down from an IF to baseband, lowpass-filtering the channel and decimating it from a sampling rate of 4 MSPS to a rate of 250 ksps. A complex sampling rate of 250 ksps is sufficient to retain all the information in the FM signal. Table 7.2 shows the parameters of the lowpass filter used in the decimation stage, while Figure 7.8 shows its magnitude response.

Table 7.2: The parameters of the FIR filter that was used to decimate each channel to a sampling rate of 250 ksps.

Design Method	Equiripple
Density Factor	20
Sampling Frequency	4 MHz
Passband Edge Frequency	50 kHz
Stopband Edge Frequency	100 kHz
Passband Attenuation	1 dB
Stopband Attenuation	80 dB
Filter Order	204

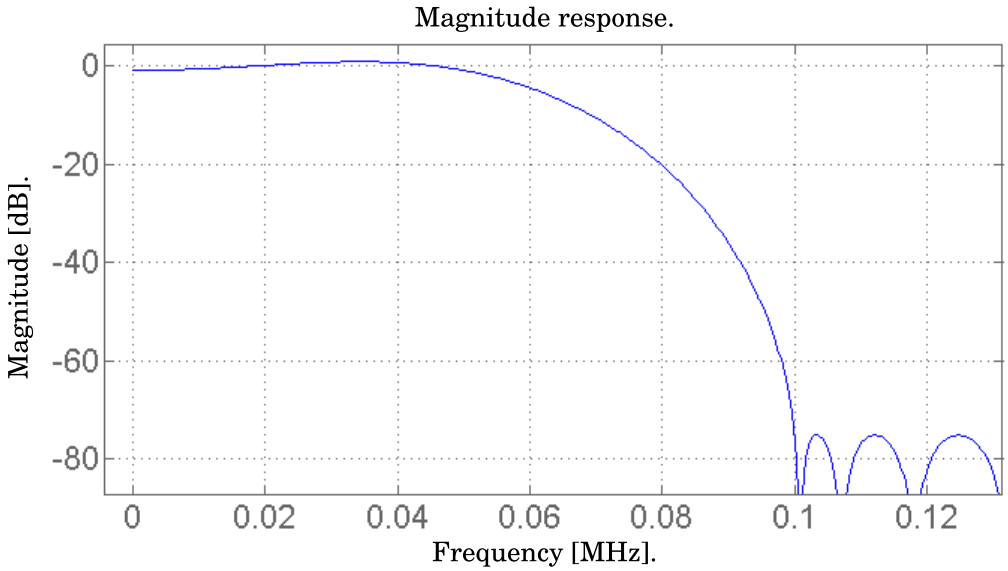

Figure 7.8: The magnitude response of the FIR decimation filter.

The frequency correction stage contains a simple Matlab script that was written to determine and correct the frequency offset between the reference and surveillance channels. The oscillators on the two TVRX daughterboards are not synchronised, and Volkwin [33] found that both oscillators drift over time. Performing the matched filter processing on the reference and surveillance channels without correcting this offset will result in target echoes appearing at much higher or lower frequencies than expected. The DPI suppression and matched filter processing stages contain the signal projection algorithm and the matched filter that were presented in Chapter 5.

7.3.1 Processing Results

Figure 7.9 shows the result of performing the matched filter processing on a 1-second block of captured reference and surveillance channel signal without suppressing the DPI. The transmitter that was used is the Tygerberg transmitter.

As expected, without any DPI suppression, the high level of correlation between the reference signal and the DPI in the surveillance channel mask any potential target reflections. A reflection originating from a clutter source can be seen at a bistatic range of approximately 45 km. Figure 7.10 shows the matched filter processing after using the signal projection algorithm to suppress the DPI in the first 10 range bins and for Doppler frequencies of -2 to 2 Hz.

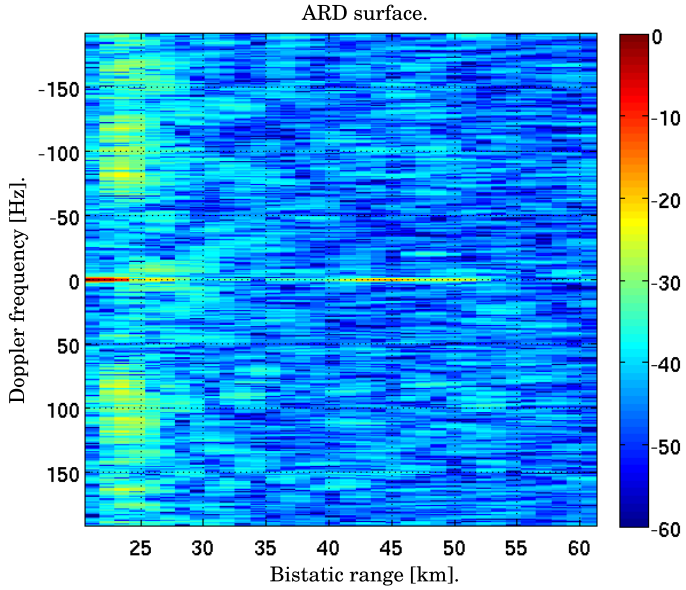

Figure 7.9: The result after processing the reference and surveillance channel signals from the Tygerberg transmitter without DPI and clutter suppression. A strong clutter source is visible at a bistatic range of 45 km.

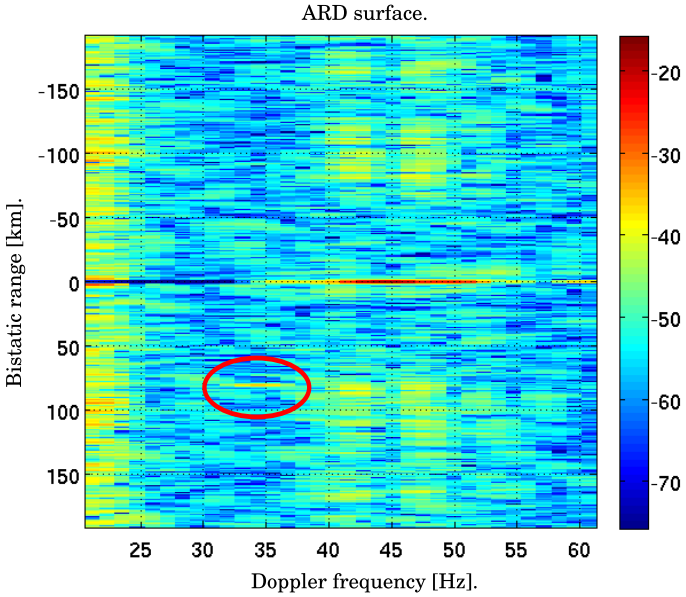

Figure 7.10: The result after processing the reference and surveillance channel signals for the Tygerberg transmitter and suppressing the DPI. A target is now visible at a bistatic range of approximately 35 km. It is evident that the DPI suppression should be extended to cancel the clutter as well.

By referring to the colourbar, it can be seen that the DPI is suppressed by approximately 17 dB. The clutter reflection is now the strongest component on the ARD surface and therefore, it should also be suppressed by the signal projection algorithm. Due to the DPI suppression, a target reflection becomes visible at a bistatic range of approximately 35 km and a Doppler frequency of 80 Hz. Figure 7.11 shows the matched filter processing result after using the signal projection algorithm to suppress the DPI and clutter in the first 34 range bins.

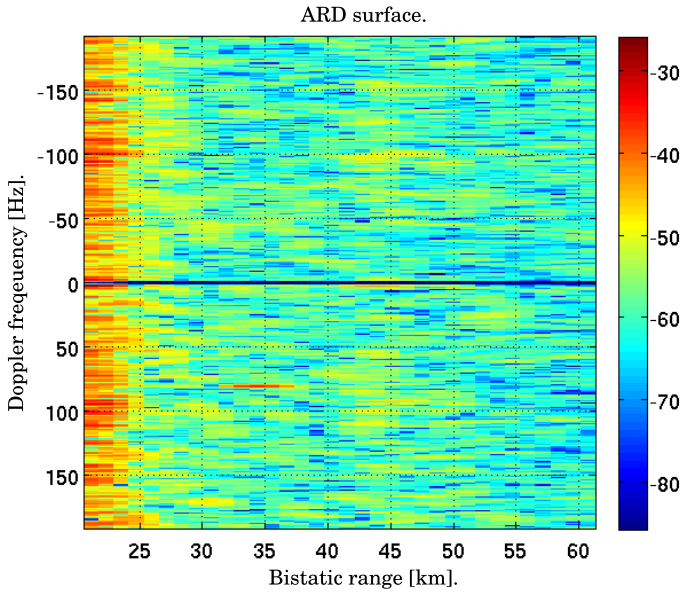

Figure 7.11: The result of processing the reference and surveillance channel signals for the Tygerberg transmitter after suppressing the DPI and clutter. The target is now clearly visible.

The target is now clearly visible and appears as a strong component on the ARD surface. The colourbar shows that the total DPI and clutter suppression equals approximately 27 dB. To illustrate the ability of a PCL radar to utilise multiple transmitters, the same processing was performed, this time using the Constantiaberg transmitter. Figure 7.12 shows the resulting ARD surface that was obtained.

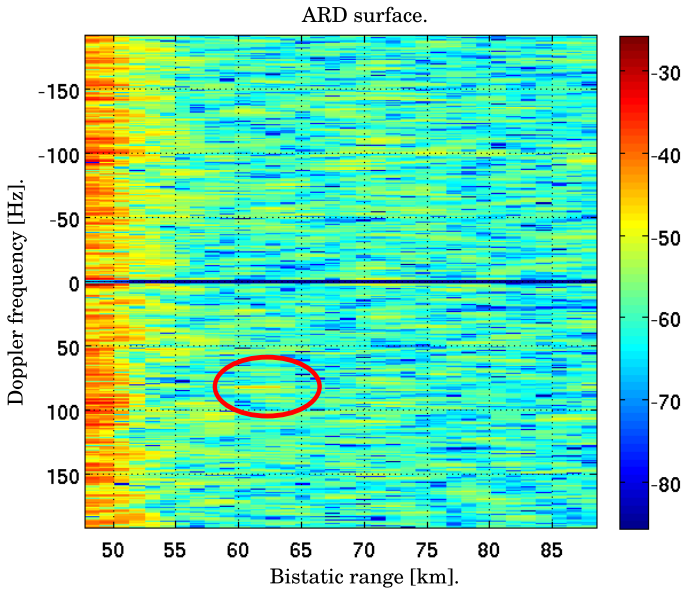

Figure 7.12: The result of processing the reference and surveillance channel signals for the Constantiaberg transmitter. The target is visible at a bistatic range of approximately 61 km.

Figure 7.12 shows that the same target is visible at a bistatic range of approximately 61 km and a Doppler frequency that is close to 80 Hz. Unfortunately, because the geometries of the two transmitter-receiver pairs are almost identical, the target appears at very similar positions on the two ARD surfaces. Placing the receiver at a location where the transmitters provide more spatial diversity, will result in a target appearing at a different position on each ARD surface. The target appears weaker on the second ARD surface because of the longer distance that the reflected signal needs to propagate. Figures 7.13 and 7.14 show the target reflections of the two ARD surfaces in more detail. The x-axis of both figures is normalised relative to the distance between the particular transmitter and the receiver.

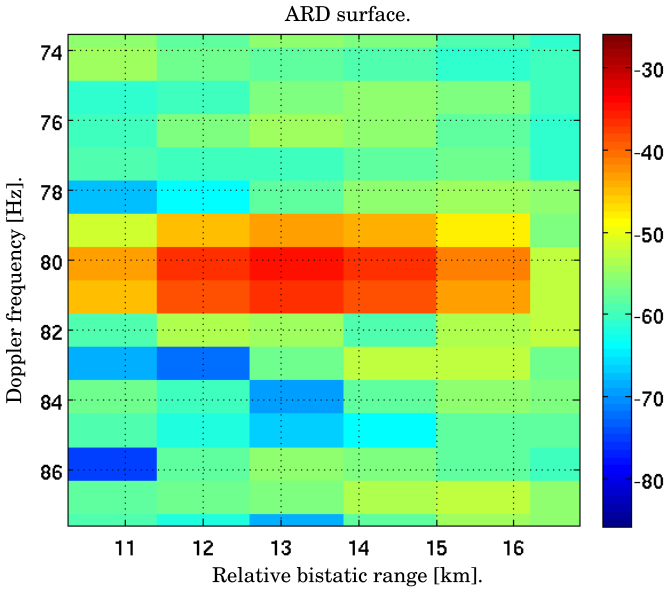

Figure 7.13: The ARD surface for the Tygerberg transmitter, showing the area around the target reflection in more detail.

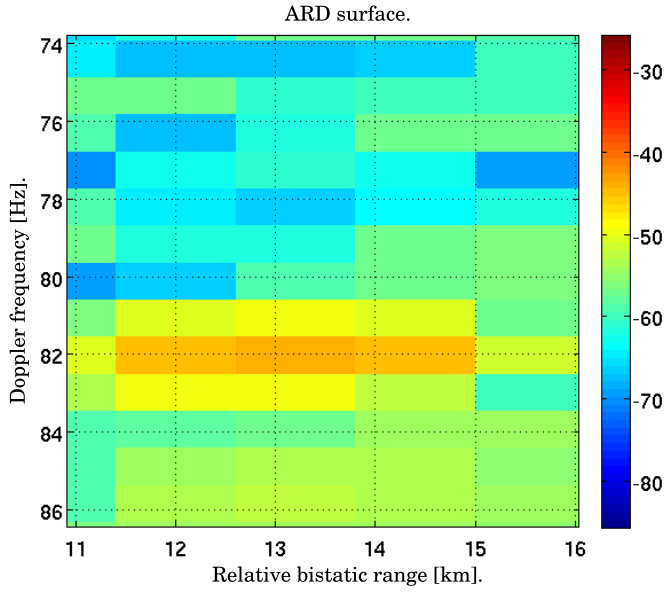

Figure 7.14: The ARD surface for the Constantiaberg transmitter, showing the area around the target reflection in more detail.

Figure 7.13 shows that for the Tygerberg transmitter, the target reflection appears at a relative bistatic range of approximately 13 km and a Doppler frequency of 80 Hz. For the Constantiaberg transmitter, the relative bistatic range is also close to 13 km, with a Doppler frequency of 82 Hz. The higher Doppler frequency can be attributed to the higher carrier frequency of the 5FM radio station transmitted by the Constantiaberg transmitter.

To illustrate the movement of a target on the ARD surface over time, a second 5-second burst of data was captured and processed. Figure 7.15 shows the result of processing a 1-second block of reference and surveillance channel signals for the Tygerberg transmitter, while Figure 7.16 shows the result of the same processing for the signals of the Constantiaberg transmitter.

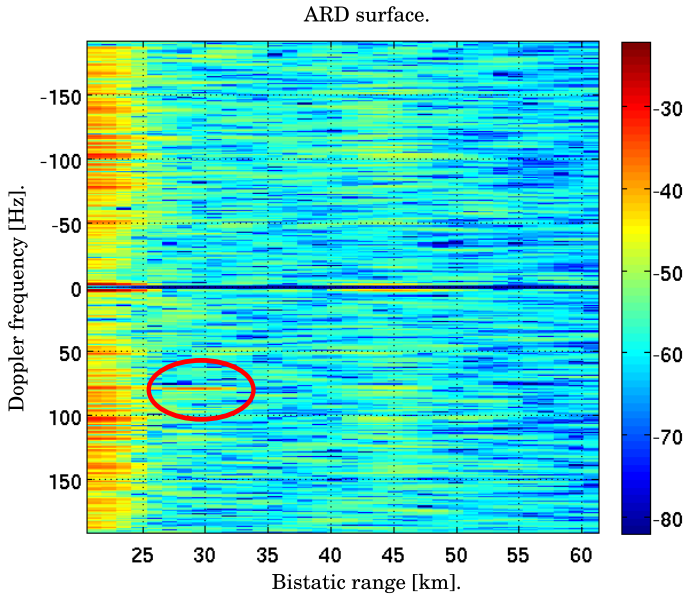

Figure 7.15: The second ARD surface for the Tygerberg transmitter. The bistatic range of the target has decreased.

It can clearly be seen that the bistatic range of the target on both ARD surfaces has decreased. This is expected, since aircraft were flying directly at the receiver and the two transmitters.

7.4 Chapter Summary

This chapter described the integration of various different components into a complete PCL radar system. It was also shown that this system has the ability to detect commercial passenger aircraft. In particular, it was found that

- The matched filter processing causes moving targets to be detectable on the ARD surface.
- The signal projection algorithm suppresses the DPI, as well as strong reflections resulting from clutter sources. It was shown that the signal projection algorithm provides between 20 and 30 dB of DPI and clutter suppression.

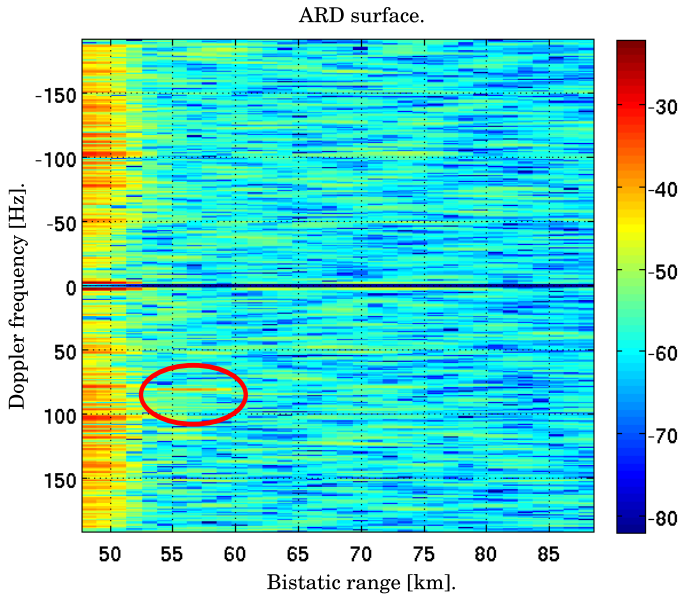

Figure 7.16: The second ARD surface for the Constantiaberg transmitter.

- Using a 4-element Yagi antenna as the surveillance channel antenna provides approximately 11 dB of DPI suppression. An additional 9 dB can be obtained by mounting the antenna for an opposite polarisation to that of the transmitted signal.
- The same target can be detected by utilising radio stations from different transmitters. It was shown in Chapter 6 that multiple transmitters allow targets to be located with a higher accuracy.

It was found that the maximum relative bistatic detection range of the PCL radar system is approximately 13 km, which is dissapointing. The following factors contribute to this short detection range

- The poor quality of the receivers, as discussed in Chapter 3.
- The distance between the Tygerberg transmitter and the receiver. The receiver should ideally be between 40 and 50 km from the transmitter [55].
- The lack of additional analogue DPI suppression prior to the A/D converter of the surveillance channel.

Chapter 8

Conclusions and Recommendations

8.1 Summary

In this dissertation, the following work was completed

- A literature review on PCL radar was presented. The review included the most important properties of PCL radar and also described the components of a typical PCL radar system. Some of the illuminators of opportunity that are available to the PCL radar designer were briefly discussed and it was shown why FM radio transmitters possess some of the most desirable properties for PCL radar.
- A possible receiver for a PCL radar system using the USRP platform was briefly evaluated. It was also shown that a bandpass filter can be designed to suppress a strong transmitter in the area of the receiver.
- The signal processing components used in the DDCs of the USRP were evaluated to identify those components that offered room for improvement. Some minor improvements were made to the filtering stages of each DDC.
- The matched filter and DPI and clutter suppression processing stages of a PCL radar system were investigated. A matched filter was implemented in C++ and its operation was verified through FERS simulations. A second, accelerated version of the matched filter was also implemented and verified. Three different DPI and clutter suppression algorithms were evaluated in terms of the convergence speed and amount of suppression that can be achieved. The suppression algorithms were also tested through FERS simulations.
- A PFB channeliser was investigated. A PFB was implemented using GNURadio signal processing blocks and it was shown that the PFB can be used to separate

a portion of the FM radio band into different channels. In a practical PCL radar system, this technique can be used to utilise more than one FM radio transmitter for target detection. A channeliser also allows only those waveforms that are favourable for PCL radar at any given time to be utilised for target detection.

- Target location using multilateration and TDOA measurements from multiple transmitters was investigated. An algorithm that calculates the coordinates of a target by solving the intersection of three contours of constant bistatic range was implemented. A FERS simulation was performed to show that this algorithm can calculate the coordinates of a target when accurate TDOA measurements are available.

- The different components were integrated into a complete PCL radar system. It was shown that the system has the ability to produce ARD surfaces that contain moving targets. It was also shown that more than one FM transmitter can be utilised to provide additional target information.

8.2 Discussions and Conclusions

During the development of this dissertation, it was found that hardware limitations played the most important role regarding the results that could be achieved. Most importantly, it was found that the TVRX daughterboard is not an ideal receiver for a PCL radar system. Figure 5.4 of Chapter 5 illustrates that at modest distances from the receiver, the power of target reflections are more than 85 dB below the power of the direct signal received from the transmitter. It is therefore very important that the PCL radar receiver utilises the full dynamic range of the A/D converter. The receiver should also have a very high linear dynamic range and a high IP_3 point to keep spurious signals generated in the receiver at a minimum. The oscillator drift between two TVRX daughterboards requires an additional processing stage to correct and therefore, adds to the processing load.

It was found that the DDCs on the USRP have the ability to take full advantage of the 72 dB of dynamic range provided by the A/D converters. The filtering stages in each DDC also suppress out-of-band signals adequately. Two elements of the USRP limit the performance of the PCL radar system. Firstly, the amount of signal bandwidth that is available for processing is limited by the slow transfer rate of the USB 2 interface between the USRP and the host PC. Each A/D converter is able to provide 64 MHz of complex bandwidth. When the USRP is used to capture two channels, a mere 4 MHz of complex bandwidth is available per channel. It would have been more ideal if the

entire 20 MHz-wide FM band was available for processing. This would allow more transmitters and a larger amount of radio stations to be utilised for target detection. The second performance limiting factor of the USRP is the amount of LEs available on the FPGA. Designing filters with very narrow transition bands requires a large amount of coefficients, which in turn requires a large amount of multiplications to be performed. For FPGAs that do not possess hardware multipliers, multipliers are synthesised using LEs. It was found that the USRP FPGA has a very limited number of LEs available for customisation. As a result, filters with a wider transition band had to be implemented. It was found that for two channels on the USRP, a maximum complex bandwidth of 2.6 MHz per channel could be achieved. The limited number of LEs also prevented a channeliser from being implemented on the FPGA.

The signal processing components that were implemented were found to be functioning as expected. Both the simulated results and the actual PCL measurements showed that the matched filter produces ARD surfaces on which moving targets are visible. Of the three DPI and clutter suppression algorithms that were evaluated, it was found that the RLS and signal projection algorithms have the fastest convergence times and provide the largest amount of suppression. Simulated results showed that both algorithms provide DPI suppression in the order of 60 dB. The signal projection algorithm has an added advantage in that it requires no parameter to control the adaptation rate. For this reason, the signal projection algorithm was chosen for the experimental PCL radar system. The actual PCL radar measurements showed that the signal projection algorithm provides approximately 27 dB of DPI and clutter suppression. This relatively low value when compared to the simulated results can be attributed to co-channel interference in the FM band, as well as decorrelating effects and spurious signals introduced by the receiver [48].

It was shown that a PFB has the ability to channelise a portion of the FM band into different channels. The PFB that was implemented using GNURadio signal processing blocks was found to be functioning correctly. It would however have been more ideal to implement a PFB on the USRP FPGA, as this would allow the CPU of the PC to spend more time performing the intensive PCL radar signal processing. Another limiting factor regarding the use of a PFB with the USRP is the low bandwidth that can be sustained across the USB 2 link. A final usable bandwidth of 2.6 MHz can contain a maximum of 13 FM radio channels that are spaced 200 kHz apart. This does not justify the added effort of implementing a PFB on an FPGA.

It was found that TDOA measurements from multiple transmitters can be used to calculate the coordinates of a target by solving the intersection of multiple contours of

constant bistatic range. Three TDOA measurements allows the x-and y-coordinates of a target to be calculated unambiguously, while a single z-coordinate ambiguity exists. The ambiguous z-coordinate is usually negative and can therefore be discarded. FM radio signals have a maximum range resolution of approximately 6 km [5]. This prevents the exact bistatic range of a target to be determined from the ARD surface, resulting in errors. These bistatic range errors lead to errors in the calculated target coordinates. For the FERS simulation that was performed, it was found that a maximum bistatic range error of 218.8 m existed. This resulted in an x-coordinate calculation error of 117.077 m, a y-coordinate calculation error of 197.386 m and a z-coordinate calculation error of 2509.655 m. The x-and y-coordinate errors seem reasonable, but it is evident that the z-coordinate error is totally unacceptable. It was also found that highly accurate target bistatic range values allow all three coordinates of the target to be calculated with a high accuracy. High-bandwidth signals, such as DVB-T transmissions, are therefore the most suitable candidates for target location using multilateration. A further problem with multilateration exists when multiple targets are present in the environment. When N transmitters are utilised and M targets are present, $N.(N-1)M^2$ false targets are formed. Clearly, target location methods that employ additional information, such as AOA and Doppler measurements should be used in a practical PCL radar system to distinguish real targets from false ones.

The primary objective of this dissertation, which was to demonstrate a working PCL radar system, was achieved. It was shown that two 4-element Yagi antennas, along with two TVRX daughterboards, a USRP, a DPI and clutter suppression algorithm and a matched filter can be used to detect commercial passenger aircraft by utilising FM radio signals. While the detection range of the system is very low, it is predicted that better receivers and additional analogue suppression will solve this problem.

8.3 Recommendations

During the course of this dissertation, numerous possible improvements to the PCL radar system were identified. The first, and most important improvement, should be to increase the detection range of the system. To achieve this, new receivers are recommended for the reference and surveillance channels. An example of a good PCL radar receiver is given by O'Hagan [48]. In his work, O'Hagan compares the performance of a superheterodyne downconversion PCL radar receiver and a direct RF sampling PCL radar receiver. It is shown that the performance of the direct RF sampling receiver is by far superior to that of the superheterodyne downconversion receiver for the following reasons

- The direct RF sampling receiver contains no mixer. Mixers introduce additional system losses, which requires further amplification. O'Hagan also shows that when the same signal is received by two identical superheterodyne downconversion receivers, the mixers in the receivers lead to decorrelation of the two channels. This decorrelation influences the performance of the DPI and clutter suppression algorithm.
- The direct RF sampling receiver contains only an amplifier and a bandpass filter. By keeping the receiver as simple as possible, the amount of unwanted effects introduced by analogue components are kept at a minimum.

In Chapter 7 it was shown that the signal projection algorithm provides approximately 27 dB of DPI and clutter suppression. O'Hagan shows that the same algorithm provides up to 37 dB of DPI suppression when direct RF sampling receivers are used to capture the reference and surveillance channel signals. For these reasons, it is recommended that a direct RF sampling receiver that is able to utilise the full 72 dB of A/D converter dynamic range of the USRP should be used. The receiver should also have a high linear dynamic range and a high IP_3. As a second step towards increasing the detection range, additional analogue suppression techniques should be investigated. These include antennas with high front-to-back ratios and the Howells-Applebaum analogue cancellation loop [28].

An analysis of the USRP FPGA showed that it would not be possible to implement a PFB channeliser, due to the limited amount of available FPGA LEs. For a PCL radar system that uses a channeliser to separate the FM band into different channels, the USRP 2 should be considered. The larger amount of LEs, as well as a number of hardware multipliers increases the amount of customisation and functionality that can be added to the FPGA. The USRP 2 also uses a Gigabit Ethernet interface for data transfer to the host PC. This provides a theoretical transfer rate of 125 MB/s. This increased transfer rate when compared to the USRP allows more signal bandwidth to be available for processing. This will also allow more FM radio channels to be utilised for target detection in the PCL radar system.

The results that were presented in Chapter 7 of this dissertation were obtained by processing captured signals in non-realtime. For a practical PCL radar system, data should be processed and displayed in realtime. To achieve this, efficient methods of implementing the signal processing stages should be investigated. Chapter 5 showed that the matched filter processing stage can be accelerated by decimating the data before calculation of the FFT for each range of interest. Future work should be aimed at taking advantage of the multiprocessing capabilities of modern CPUs. This involves

using threads to perform multiple tasks in parallel. Other options include the implementation of the signal processing stages on more advanced computing platforms, such as the Sony PlayStation 3[1] and NVIDIA[2] graphics cards with CUDA[3] technology [56].

[1]Accessed 10 March 2010, <http://http://us.playstation.com/ps3/>.
[2]Accessed 10 March 2010, <http://www.nvidia.com/page/home.html>.
[3]Accessed 10 March 2010, <http://www.nvidia.com/object/cuda_home_new.html>.

Appendix A

Additional PCL processing results

A number of measurements were captured during the final PCL radar experiment. The following figures show some of the ARD surfaces on which targets are visible.

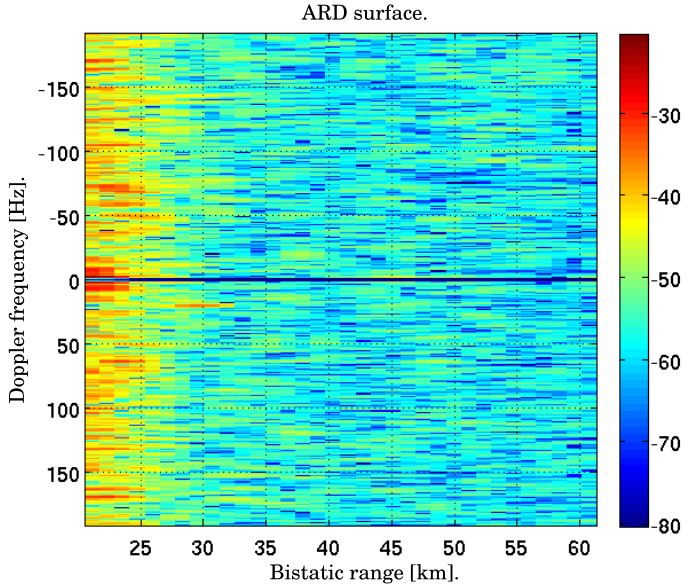

Figure A.1: The ARD surface obtained after processing a 1-second block of the 7th PCL measurement for the Tygerberg transmitter.

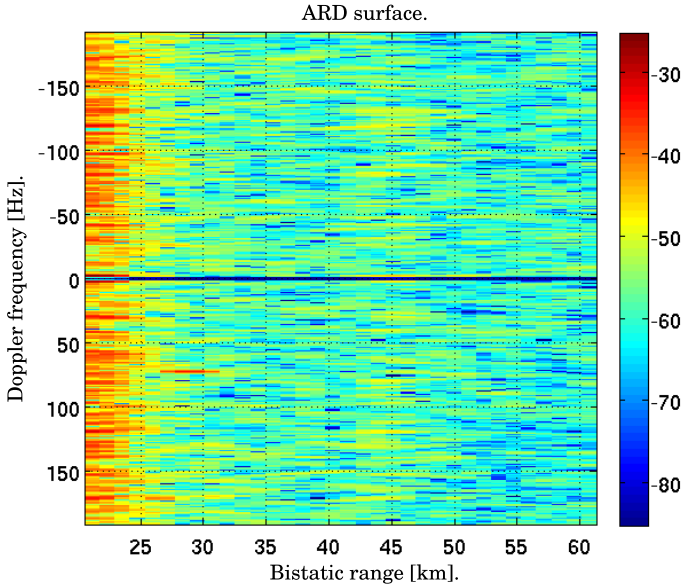

Figure A.2: The ARD surface obtained after processing a 1-second block of the 9th PCL measurement for the Tygerberg transmitter.

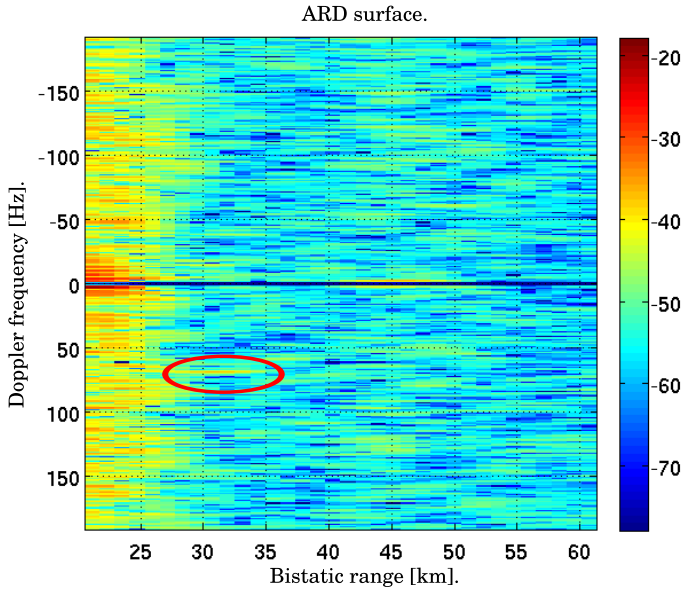

Figure A.3: The ARD surface obtained after processing a 1-second block of the 10th PCL measurement for the Tygerberg transmitter.

Appendix B

Project DVD Directory Layout

The directory layout of the DVD that accompanies this dissertation is depicted in Figure B.1.

Name	Size	Type	Date Modified
c++_code	9 items	folder	Mon 08 Feb 2010 11:28:57 SAST
example_fers_simulations	3 items	folder	Tue 09 Feb 2010 12:17:12 SAST
fpga_image	1 item	folder	Sat 20 Mar 2010 16:30:55 SAST
fri_22jan_2010_measurements	23 items	folder	Mon 08 Feb 2010 00:03:10 SAST
fri_22jan_2010_pictures	8 items	folder	Wed 03 Feb 2010 15:45:04 SAST
gnuradio_scripts	6 items	folder	Tue 09 Feb 2010 12:19:35 SAST
iverilog_simulations	7 items	folder	Sat 20 Mar 2010 16:34:50 SAST
multilateration	2 items	folder	Mon 08 Feb 2010 11:48:55 SAST
pfb	23 items	folder	Sat 20 Mar 2010 19:58:48 SAST
processing_files	13 items	folder	Fri 29 Jan 2010 15:30:27 SAST
unused_cancellers	3 items	folder	Fri 29 Jan 2010 15:37:09 SAST
usrp_new_2times	15 items	folder	Mon 08 Feb 2010 12:38:33 SAST

Figure B.1: Directory layout of the project DVD.

The contents of the folders are as follows

c++_code Contains the C++ matched filter and accelerated matched filter implementations.

example_fers_simulations Contains three different FERS simulation setups showing how to perform a bistatic simulation, a simulation with multiple transmitters, as well as a 10-second simulation. It is also shown how to import a custom antenna pattern into a FERS simulation.

fpga_image Contains the FPGA image for the modified USRP FPGA build described in Chapter 4.

fri_22jan_2010_measurements Contains all the measurement data that was captured on the day that the final PCL experiment was performed.

fri_22jan_2010_pictures Contains the ARD surfaces of the measurements on which targets are visible.

gnuradio_scripts Contains all the GNURadio scripts that were written during the course of this dissertation. This includes the scripts that were used in Chapter 3 to evaluate the performance of the TVRX daughterboards, as well as the script that was used to capture the PCL data.

iverilog_simulations Contains the Icarus Verilog files that were used to perform the simulations described in Chapter 4.

multilateration Contains the Python script that calculates the coordinates of a target from three bistatic range measurements.

pfb Contains the GNURadio script that implements a software PFB, as well as the PFB implemented in Matlab

processing_files Contains all the Matlab files that were used to obtain the final results presented in Chapter 7. This includes the frequency correction algorithm, the signal projection algorithm and the matched filter.

unused_cancellers Contains the Matlab implementations of the NLMS and the RLS algorithms.

usrp_new_2times Contains the Quartus project of the improved USRP FPGA build.

Bibliography

[1] A. Moccia, M. D'Errico, A. Moreiga, G. Krieger, P. Dubois-Fernandez, H. Cantalloube, B. Vaizan, M. Cherniakov, T. Zeng, P. Howland, H. Griffiths, C. Baker, and J. Sahr, *Bistatic Radar: Emerging Technology*. John Wiley & Sons, Ltd, 2008.

[2] M. Jackson, "The geometry of bistatic radar systems," *Communications, Radar and Signal Processing, IEE Proceedings F*, vol. 133, pp. 604–612, December 1986.

[3] H. Griffiths, "Bistatic and Multistatic Radar," tech. rep., University College London.

[4] T. Tsao, M. Slamani, P. Varshney, D. Weiner, H. Schwarzlander, and S. Borek, "Ambiguity function for a bistatic radar," *Aerospace and Electronic Systems, IEEE Transactions on*, vol. 33, pp. 1041–1051, July 1997.

[5] C. Baker, H. Griffiths, and I. Papoutsis, "Passive coherent location radar systems. part 2: waveform properties," *Radar, Sonar and Navigation, IEE Proceedings -*, vol. 152, pp. 160–168, June 2005.

[6] R. E. Watson, "Receiver Dynamic Range: Part 1," tech. rep., Watkins-Johnson Company, 1987.

[7] M. Donadio, "CIC Filter Introduction," tech. rep., Iowegian, July 2000.

[8] P. Vaidyanathan, "Multirate digital filters, filter banks, polyphase networks, and applications: a tutorial," *Proceedings of the IEEE*, vol. 78, pp. 56–93, Jan 1990.

[9] A. Poularikas and Z. Ramadan, *Adaptive Filtering Primer with Matlab*. CRC Press, 2006.

[10] F. Harris, C. Dick, and M. Rice, "Digital receivers and transmitters using polyphase filter banks for wireless communications," *Microwave Theory and Techniques, IEEE Transactions on*, vol. 51, pp. 1395–1412, Apr 2003.

[11] P. Howland, D. Maksimiuk, and G. Reitsma, "FM radio based bistatic radar," *Radar, Sonar and Navigation, IEE Proceedings* -, vol. 152, pp. 107–115, June 2005.

[12] N. Willis, *Bistatic Radar*. Scitech Publishing, Inc., second ed., 2005.

[13] P. Howland, "Editorial: Passive radar systems," *Radar, Sonar and Navigation, IEE Proceedings* -, vol. 152, pp. 105–106, June 2005.

[14] J. Baniak, G. Baker, A. Cunningham, and L. Martin, "Silent Sentry Passive Surveillance." Accessed 24 September 2009, <http://servv89pn0aj.sn.sourcedns.com/gbpprorg/mil/radar/sentry.pdf>, 1999.

[15] H. Griffiths and N. Long, "Television-based bistatic radar," *Communications, Radar and Signal Processing, IEE Proceedings F*, vol. 133, pp. 649–657, December 1986.

[16] P. Hudson, "Passive Multistatic Radars in Anti-Stealth Air Defence," Master's thesis, Canadian Forces College, 2003.

[17] J. Mitola, "The software radio architecture," *Communications Magazine, IEEE*, vol. 33, pp. 26–38, May 1995.

[18] F. Abbas, "The USRP under 1.5x Magnifying Lens!." Accessed 24 September 2009, <http://www.scribd.com/doc/9688095/USRP-Documentation>, 2008.

[19] F. Abbas, "Simple User Manual for Gnuradio 3.1.1." Accessed 24 September 2009, <http://rapidshare.com/files/71300271/Simple-Gnuradio-User-Manual.pdf>, 2007.

[20] M. Inggs and M. Brooker, "Extensible simulator for waveform diversity testing," in *Waveform Diversity and Design Conference, 2009 International*, pp. 273–277, Feb. 2009.

[21] H. Griffiths and C. Baker, "Passive coherent location radar systems. part 1: performance prediction," *Radar, Sonar and Navigation, IEE Proceedings* -, vol. 152, pp. 153–159, June 2005.

[22] P. Howland, "Passive Tracking Of Airborne Targets Using Only Doppler And Doa Information," in *Algorithms for Target Tracking, IEE Colloquium on*, pp. 37–39, May 1995.

[23] D. Tan, H. Sun, Y. Lu, M. Lesturgie, and H. Chan, "Passive radar using Global System for Mobile communication signal: theory, implementation and measurements," *Radar, Sonar and Navigation, IEE Proceedings* -, vol. 152, pp. 116–123, June 2005.

[24] H. Kuschel, J. Heckenbach, S. Muller, and R. Appel, "On the potentials of passive, multistatic, low frequency radars to counter stealth and detect low flying targets," in *Radar Conference, 2008. RADAR '08. IEEE*, pp. 1–6, May 2008.

[25] V. Koch and R. Westphal, "New approach to a multistatic passive radar sensor for air/space defense," *Aerospace and Electronic Systems Magazine, IEEE*, vol. 10, pp. 24–32, Nov 1995.

[26] H. Guo, K. Woodbridge, and C. Baker, "Evaluation of WiFi beacon transmissions for wireless based passive radar," in *Radar Conference, 2008. RADAR '08. IEEE*, pp. 1–6, May 2008.

[27] J. Sahr and F. Lind, "The Manastash Ridge radar: A passive bistatic radar for upper atmospheric radio science," *Radio Science*, vol. 32, pp. 2345–2358, November 1997.

[28] D. O'Hagan, C. Baker, and H. Griffiths, "Signal and Interference Analysis: Proposed Analogue Signal Suppression Techniques for PCL Radar," in *Radar Conference, 2006. EuRAD 2006. 3rd European*, pp. 296–298, Sept. 2006.

[29] R. Nitzberg, *Radar signal processing and adaptive systems*. Artech House, 1999.

[30] R. Kell, "On the derivation of bistatic RCS from monostatic measurements," *Proceedings of the IEEE*, vol. 53, pp. 983–988, Aug. 1965.

[31] A. Lauri, F. Colone, R. Cardinali, C. Bongioanni, and P. Lombardo, "Analysis and Emulation of FM Radio Signals for Passive Radar," in *Aerospace Conference, 2007 IEEE*, pp. 1–10, March 2007.

[32] R. Saini and M. Cherniakov, "DTV signal ambiguity function analysis for radar application," *Radar, Sonar and Navigation, IEE Proceedings* -, vol. 152, pp. 133–142, June 2005.

[33] A. Volkwin, "Suitability of a Commercial Software Defined Radio System for Passive Coherent Location," Master's thesis, Department of Electrical Engineering, University of Cape Town, 2008.

[34] J. R. Fisk, "Receiver noise figure sensitivity and dynamic range - what the numbers mean," *Ham Radio Magazine*, 1975.

[35] R. E. Watson, "Receiver Dynamic Range: Part 2," tech. rep., Watkins-Johnson Company, 1987.

[36] L. Devlin, "RF Filter Design Using Coupled Co-axial Resonators," tech. rep., Plextek Ltd.

[37] R. Andraka, "High Performance Digital Down-Converters for FPGAs," *Xilinx Xcell Journal*, no. 38, 2000.

[38] R. Andraka, "A survey of CORDIC algorithms for FPGA based computers," in *FPGA '98: Proceedings of the 1998 ACM/SIGDA sixth international symposium on Field programmable gate arrays*, (New York, NY, USA), pp. 191–200, ACM, 1998.

[39] E. Hogenauer, "An economical class of digital filters for decimation and interpolation," *Acoustics, Speech and Signal Processing, IEEE Transactions on*, vol. 29, pp. 155–162, Apr 1981.

[40] L. Milic, *Multirate Filtering for Digital Signal Processing: MATLAB Applications*. IGI Global, 2009.

[41] F. Harris, "On the use of windows for harmonic analysis with the discrete Fourier transform," *Proceedings of the IEEE*, vol. 66, pp. 51–83, Jan. 1978.

[42] P. Bezousek and V. Schejbal, "Coherent multilateration systems," in *Microwaves, Radar and Remote Sensing Symposium, 2008. MRRS 2008*, pp. 60–65, Sept. 2008.

[43] K. Kulpa and J. Misiurewicz, "Stretch Processing for Long Integration Time Passive Covert Radar," in *Radar, 2006. CIE '06. International Conference on*, pp. 1–4, Oct. 2006.

[44] M. Malanowski, "Comparison of Adaptive Methods for Clutter Removal in PCL Radar," in *Radar Symposium, 2006. IRS 2006. International*, pp. 1–4, May 2006.

[45] S. Haykin, *Adaptive Filter Theory*. Prentice-Hall, 3rd ed., 1996.

[46] A. Guner, M. Temple, and J. Claypoole, R.L., "Direct-path filtering of DAB waveform from PCL receiver target channel," *Electronics Letters*, vol. 39, pp. 118–119, Jan. 2003.

[47] F. Colone, D. W. O'Hagan, P. Lombardo, and C. J. Baker, "A multistage processing algorithm for disturbance removal and target detection in Passive Bistatic Radar," *Trans AES*, vol. TBD, 2009. Accepted for publication.

[48] D. W. O'Hagan, *Passive Bistatic Radar Performance Characterisation Using FM Radio Illuminators of Opportunity*. PhD thesis, Department of Electronic & Electrical Engineering, University College London, 2009.

[49] Y. Trofimova, "Multilateration Error Investigation and Classification. Error Estimation," *Transport and Telecommunication*, vol. 8, no. 2, pp. 28–37, 2007.

[50] L. Paradowski, "Microwave emitter position location: present and future," in *Microwaves and Radar, 1998. MIKON '98., 12th International Conference on*, vol. 4, pp. 97–116 vol.4, May 1998.

[51] G. Savir, "Scalable and Reconfigurable Digital Front-End for SDR Wideband Channelizer," Master's thesis, Faculty of Electrical Engineering, TUDelft, 2006.

[52] R. Bucher and D. Misra, "A Synthesizable VHDL Model of the Exact Solution for Three-dimensional Hyperbolic Positioning System," *VLSI Design*, vol. 15, no. 2, pp. 507–520, 2002.

[53] Y. Norouzi and M. Derakhshani, "Joint time difference of arrival/angle of arrival position finding in passive radar," *Radar, Sonar & Navigation, IET*, vol. 3, pp. 167–176, April 2009.

[54] H. Griffiths and C. Baker, "Measurement and analysis of ambiguity functions of passive radar transmissions," in *Radar Conference, 2005 IEEE International*, pp. 321–325, May 2005.

[55] P. Howland, "Personal communications," *Chief Scientist C2ISR at NATO C3 Agency*.

[56] K. Szumski, M. Malanowski, J. Kulpa, W. Porczyk, and K. Kulpa, "Real-time software implementation of Passive Radar," in *Radar Conference, 2009. EuRAD 2009. European*, pp. 33–36, 30 2009-Oct. 2 2009.